Quantum Optomechanics in a Liquid

A. B. Shkarin,[1] A. D. Kashkanova,[1] C. D. Brown,[1] S. Garcia,[2] K. Ott,[2] J. Reichel,[2] and J. G. E. Harris[1,3,4,5,*]

[1]*Department of Physics, Yale University, New Haven, Connecticut 06520, USA*
[2]*Laboratoire Kastler Brossel, ENS-Université PSL, CNRS, Sorbonne Université,*
Collège de France 24 rue Lhomond, 75005 Paris, France
[3]*Department of Applied Physics, Yale University, New Haven, Connecticut 06520, USA*
[4]*Yale Quantum Institute, Yale University, New Haven, Connecticut 06520, USA*
[5]*Wright Laboratory, Department of Physics, Yale University, New Haven, Connecticut 06520, USA*

We measure the quantum fluctuations of a single acoustic mode in a volume of superfluid He that is coupled to an optical cavity. Specifically, we monitor the Stokes and anti-Stokes light scattered by a standing acoustic wave that is confined by the cavity mirrors. The intensity of these signals (and their cross-correlation) exhibits the characteristic features of the acoustic wave's zero-point motion and the quantum backaction of the intracavity light. While these features are also observed in the vibrations of solid objects and ultracold atomic gases, their observation in superfluid He opens the possibility of exploiting the remarkable properties of this material to access new regimes of quantum optomechanics.

When light interacts with a macroscopic object, it typically produces complex excitations within the object that cannot be reversed by practical means. This effectively destroys the light's quantum state and precludes access to the macroscopic object's quantum dynamics. This limitation can be overcome by identifying an object with a collective degree of freedom that interacts strongly with the electromagnetic (EM) field but remains well isolated from other degrees of freedom. Examples include superconducting circuits [1], atomic gases [2], ferromagnets [3], and objects whose vibrations couple to an EM cavity [4]. In the lattermost case (known as an optomechanical system), the object's vibrational mode is isolated by its high quality factor, while its interaction with the EM field results from radiation pressure, electrostriction, or other reversible processes [4]. Optomechanical experiments have demonstrated quantum effects in mechanical oscillators as massive as ~ 100 ng [5], as hot as ~ 300 K [6], and employing EM fields in the microwave [7,8] or near-infrared [5,6,9–13] domains. They have been used to realize hybrid quantum systems with superconducting qubits [7], atomic spins [13], and solid-state impurities [12] and show considerable promise in applications such as coherent microwave-to-optical conversion [14,15]. To date, the mechanical oscillators demonstrating quantum behavior have been formed from solids [5–9,11–13] or ultracold gases [10]. Here we describe measurements of quantum behavior in the vibration of a liquid body that is coupled to an optical cavity. Specifically, we monitor the dynamics of an individual acoustic standing wave in a volume of superfluid liquid helium and observe the characteristic signatures of zero-point motion and quantum backaction [16–18]. This opens

the possibility of exploiting the properties of liquids (and superfluid helium in particular) to access qualitatively new regimes of quantum optomechanics.

The signatures of quantum motion described here have also been measured in solid-based and gas-based optomechanical systems [5,6,9–11]. However, their observation in a liquid is significant because of several fundamental and technical features offered by liquid-based optomechanical systems. First, liquids possess mechanical degrees of freedom (such as rotational flow) with unbounded displacement; as such, they differ qualitatively from the normal modes of a solid, which represent bounded harmonic oscillations about an equilibrium [19,20]. Second, the presence of a free surface allows a liquid body's geometry and topology to be reconfigured *in situ* and to serve as a dynamical degree of freedom. Third, superfluid He can host a number of atomlike impurities (such as electrons, ions, and He_2^* excimers) potentially suitable for hybrid quantum systems [21,22]. Fourth, the remarkable physical properties of superfluid He help to address some of the outstanding technical challenges in optomechanics: Its exceptional thermal conductivity allows for effective cooling by conventional refrigerators, its acoustic damping can be predicted *a priori* [23,24], and its ability to conformally fill or coat a cryogenic EM resonator [23–26] means that such devices require no *in situ* alignment. Lastly, this type of device offers the possibility of applying precision optical measurements to address outstanding questions regarding the fundamental properties of superfluid He [27,28]. Some of the features listed above can be explored by optomechanical systems in the classical regime (using normal fluids [29,30] or superfluid He [23–26]). However, the quantum regime of liquid-based
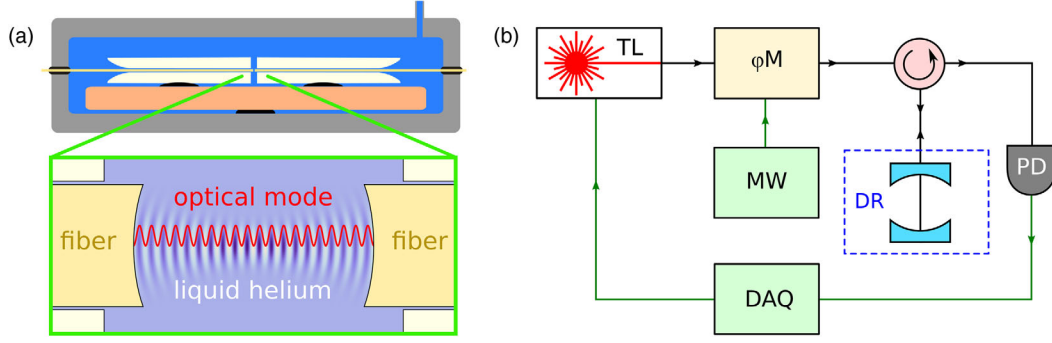
FIG. 1.   Schematic of the experiment. (a) Top: Illustration of the optomechanical device. The optical fibers (yellow) and ferrules (white) are fixed inside a Cu cell (gray) which is attached to the mixing chamber of a dilution refrigerator (DR, not shown). Liquid He (blue) fills the cell. The fibers enter the cell via epoxy feedthroughs (black). Bottom: Enlarged view of the cavity. Red curve: The intensity profile of an optical mode. Blue shading: The density profile of the acoustic mode that couples to the optical mode. The actual optical and acoustic modes used in this work have, respectively, 91 and 182 half wavelengths along the cavity length. (b) Simplified layout of the measurement setup. Light from a tunable laser (TL) passes through a phase modulation system (φM) driven by a microwave source (MW). Light is delivered to (and collected from) the DR via a circulator (pink). The reflected light is collected on a photodiode (PD), and the resulting photocurrent is analyzed by a data acquisition system (DAQ). Details are given in the Supplemental Material [31].

optomechanics remains largely unexplored by theory and experiment.

The device used in this study is shown in Fig. 1(a). It consists of a cavity formed between the end faces of two optical fibers. These end faces serve as high-reflectivity mirrors and are mounted on the mixing chamber (MC) of a dilution refrigerator (see Supplemental Material [31]). When the cavity is excited by a laser, these mirrors confine an optical standing wave. The mode used in these experiments has frequency $\omega_{\mathrm{opt}} = 2\pi \times 196.0$ THz, linewidth $\kappa = 2\pi \times 21$ MHz, external coupling rate $\kappa_{\mathrm{ext}} = 2\pi \times 10$ MHz (including the transverse mode matching), and finesse $F = 9.5 \times 10^4$. The device is similar to the one described in Ref. [24] but offers improved thermal conductance between the cavity and the MC.

When the cavity is filled with liquid He, the fiber ends also confine acoustic modes. The acoustic modes' density variations alter the index of refraction experienced by the optical modes. Equivalently, the optical modes' intensity variations exert a force that can excite the acoustic modes. This leads [24,53] to optomechanical coupling of the conventional [4] form $H_{\mathrm{OM}} = \hbar g^{(0)} a^\dagger a(c^\dagger + c)$ where a and c are the annihilation operators for cavity photons and phonons, respectively. Straightforward geometric considerations show that the single-quantum optomechanical coupling rate $g^{(0)}$ is maximized for an acoustic mode with half the wavelength of the optical mode [24,53]. As a result, the optical mode used in this experiment couples to an acoustic mode with resonant frequency $\omega_{\mathrm{ac}} \approx 2\pi \times 319.2$ MHz.

The device was characterized using optomechanically induced transparency or amplification, a standard technique in which laser tones applied to the cavity drive the acoustic mode and record its driven motion [54]. Analysis of these measurements (see Supplemental Material [31] and Ref. [24])

provides a best-fit value of $g^{(0)} = 2\pi \times (3.6 \pm 0.1)$ kHz (unless noted, errors correspond to the statistical uncertainty in least-squares fits). This value is consistent with the *a priori* calculation (Supplemental Material [31]) $g^{(0)} = 2\pi \times (3.9 \pm 0.2)$ kHz (here the error is due to uncertainty in the mirror materials properties) [55].

In the absence of any external drive, the acoustic mode's thermal and quantum fluctuations can be inferred from the motional sidebands imprinted on a laser beam that interacts with the cavity. Standard optomechanics theory predicts that the acoustic mode's thermal fluctuations contribute equally to the red and blue motional sidebands but that quantum fluctuations contribute unequally [4]. Specifically, when the blue sideband is converted to a photocurrent via heterodyne detection, its power spectral density $S_{ii}^{(bb)}$ is predicted to consist of a noise floor plus a peak that reproduces the acoustic mode's Lorentzian line shape. When the photocurrent is appropriately calibrated (see below and the Supplemental Material [31]), the height of this peak h_{bb} equals the mode's mean phonon number n_{ac}. The same holds for $S_{ii}^{(rr)}$ (the photocurrent spectrum resulting from the red sideband), except that its peak height $h_{rr} = n_{\mathrm{ac}} + 1$. Furthermore, the spectrum of correlations between the two sidebands ($S_{ii}^{(rb)}$) is predicted to have a real part consisting of the same line shape (with height $h_{rb,\mathrm{Re}} = n_{\mathrm{ac}} + \frac{1}{2}$) and an imaginary part with an antisymmetric line shape of magnitude $h_{rb,\mathrm{Im}} = \frac{1}{2}$. (Equivalent information can also be extracted by measuring both quadratures of the reflected light [6,56].)

While various interpretations can be applied to these features (see Refs. [16–18] and Supplemental Material [31]), they are intrinsically quantum in nature as the perceived energy differences between $S_{ii}^{(bb)}$, $S_{ii}^{(rr)}$, and
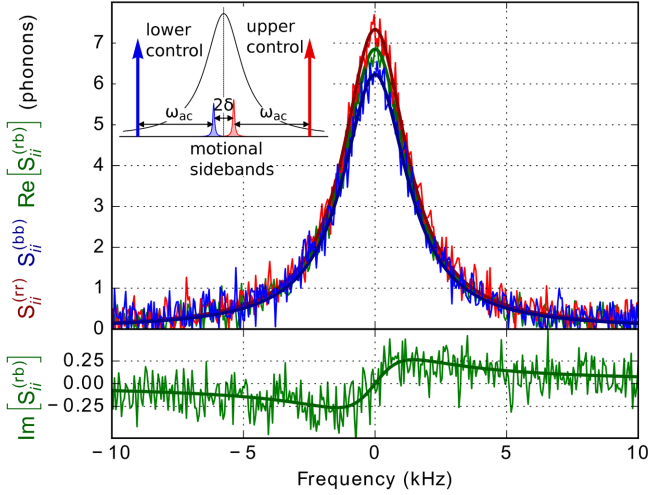
FIG. 2. Sidebands produced by the acoustic mode's fluctuations. Inset: Illustration of the measurement scheme. Black curve: Cavity line shape. Colored arrows: Laser tones. Colored curves: Acoustic sidebands. Upper panel: The spectrum of the red and blue motional sidebands ($S_{ii}^{(rr)}$ and $S_{ii}^{(bb)}$) and the real part of their cross-correlation (Re[$S_{ii}^{(rb)}$]). A frequency-independent background has been subtracted from $S_{ii}^{(rr)}$ and $S_{ii}^{(bb)}$. Lower panel: The imaginary part of the cross-correlation (Im[$S_{ii}^{(rb)}$]). The data were normalized and fit as described in the text and the Supplemental Material [31]. For this measurement, $T_{MC} = 20$ mK and $n_{circ} = 400$.

$S_{ii}^{(rb)}$ are set by the energy of a single phonon $\hbar\omega_{ac}$. It is convenient to characterize these quantum features by three parameters: $H_{AS} = h_{rr} - h_{bb}$, $H_{Re} = 2(h_{rb,Re} - h_{bb})$, and $H_{Im} = 2h_{rb,Im}$. Each is predicted to be unity, independent of experimental conditions such as temperature and laser power.

The system described here operates well in the resolved sideband regime ($\omega_{ac} \approx 15\,\kappa$), so it is impractical to measure the two sidebands produced from a single beam (at least one will be strongly suppressed by the cavity's response). Instead, we apply two measurement beams to the cavity: an "upper" beam with detuning (relative to the cavity resonance) $\Delta_u = \omega_{ac} + \delta$ and a "lower" beam with detuning $\Delta_l = -\omega_{ac} - \delta$ where δ is set to $2\pi \times 100$ kHz. As illustrated in the inset of Fig. 2, this ensures that two motional sidebands are approximately resonant with the cavity: the lower beam's blue sideband and the upper beam's red sideband. The offset δ is chosen so that these sidebands do not overlap but do lie within the measurement bandwidth. The sidebands are recorded simultaneously via a heterodyne measurement, and $S_{ii}^{(bb)}$, $S_{ii}^{(rr)}$, and $S_{ii}^{(rb)}$ are computed from this record (Supplemental Material [31]). Each of these records is calibrated (Supplemental Material [31]) so that the features in $S_{ii}^{(bb)}$, $S_{ii}^{(rr)}$, and $S_{ii}^{(rb)}$ should be related to n_{ac} as described above.

Figure 2 shows a typical measurement of $S_{ii}^{(rr)}$ and $S_{ii}^{(bb)}$ (with their frequency-independent background subtracted)

as well as $S_{ii}^{(rb)}$. The features in these data appear qualitatively consistent with the quantum effects described above. To quantify this comparison, we fit $S_{ii}^{(rr)}$, $S_{ii}^{(bb)}$, and Re$(S_{ii}^{(rb)})$ to the function $h_x / [1 + 4(\omega - \omega_{ac})^2 / \gamma_{ac}^2]$ with $x = \{rr; bb; rb, \text{Re}\}$, while Im$(S_{ii}^{(rb)})$ is fit to $h_{rb,\text{Im}}(\omega - \omega_{ac})(\gamma_{ac}/2)^{-1}[1 + 4(\omega - \omega_{ac})^2/\gamma_{ac}^2]^{-1}$ (Supplemental Material [31]). Here, ω is the measurement frequency, and ω_{ac} and γ_{ac} are the acoustic mode's frequency and linewidth. The fits in Fig. 2 give $H_{AS} = 1.10 \pm 0.086$, $H_{Re} = 0.97 \pm 0.14$, and $H_{Im} = 1.06 \pm 0.055$.

The parameters H_{AS}, H_{Re}, and H_{Im} are defined to reflect only the quantum aspects of the system's dynamics; however, they are determined from fit parameters (h_{bb}, h_{rr}, $h_{rb,\text{Re}}$, and $h_{rb,\text{Im}}$) that reflect both thermal and quantum fluctuations. To compare the quantum and thermal signatures in the data, we measured heterodyne spectra similar to those in Fig. 2 over a range of T_{MC} (the MC temperature) and n_{circ} (the intracavity photon number). Figures 3(a) and 3(b) show the inferred phonon number of the acoustic mode's bath defined as $n_{th} = n_{ac}(\gamma_{ac}/\gamma_{ac,0}) - n_O\gamma_O/\gamma_{ac,0}$. This expression was evaluated by fitting heterodyne spectra (as in Fig. 2) for γ_{ac} and n_{ac} [for these measurements we use $n_{ac} = \frac{1}{2}(h_{bb} + h_{rr} - 1)$]. Standard optomechanics theory [4] was used to calculate the phonon number associated with the quantum backaction n_O and the optical damping rate $\gamma_O = \gamma_{ac} - \gamma_{ac,0}$ (where $\gamma_{ac,0}$ is the acoustic damping rate when $n_{circ} = 0$). For all the measurements described here, n_{th} nearly equals n_{ac}, as the "quantum backaction" term $n_O\gamma_O/\gamma_{ac} < 1.1$, and the "laser cooling" factor $\gamma_{ac}/\gamma_{ac,0}$ differs from unity by no more than 5% [57]. We plot n_{th} (rather than n_{ac}) in Fig. 3(b) to facilitate comparison with the thermal model described in the Supplemental Material [31].

Figure 3(a) shows n_{th} vs T_{MC}. For $T_{MC} \gtrsim 150$ mK, n_{th} tracks T_{MC}, while for $T_{MC} \lesssim 150$ mK, n_{th} does not track T_{MC} and clearly depends on n_{circ}. Qualitatively similar behavior was found in Ref. [24] and was accounted for by a thermal model in which the He temperature was set by the heat from optical absorption in the mirrors and the cooling provided by the slender superfluid region which linked that device to the MC. The present device's more open geometry gives improved cooling, but the absence of a thermal bottleneck means that the temperature is not uniform throughout the cavity. We calculate the cavity's temperature distribution using standard models of thermal transport and convert this distribution into an effective temperature for the mode T_{eff} that depends upon T_{MC} and n_{circ} (Supplemental Material [31]). Figure 3(b) shows the same values of n_{th} as Fig. 3(a) but plotted vs T_{eff}. In this case, the data show close agreement with the prediction $n_{th} = 1/(e^{\hbar\omega_{ac}/k_B T} - 1)$ over the full range of T_{MC} and n_{circ}, indicating that this approach captures the main features of the device's thermal behavior. The deviations from the prediction are roughly independent of T_{MC} and n_{circ} and so
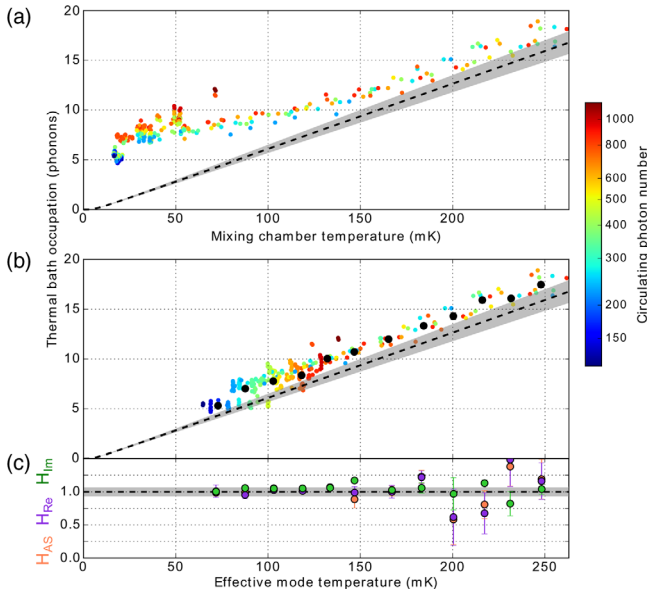
FIG. 3. Thermal and quantum fluctuations of the acoustic mode. (a) The mean phonon number n_{th} associated with the acoustic mode's bath temperature plotted vs T_{MC}. (b) The same measurements of n_{th} as in (a) but plotted as a function of T_{eff}, the effective device temperature calculated in the Supplemental Material [31]. The color of each marker encodes n_{circ}, the intracavity photon number. The black points are obtained by averaging data in 15 mK bins. In both (a) and (b), the dashed lines show the expected behavior $n_{\text{th}} = 1/(e^{\hbar\omega_{\text{ac}}/k_B T} - 1)$, while the gray area represents the systematic uncertainty resulting from the calibration of the heterodyne signal (Supplemental Material [31]). (c) Three measures of the quantum features plotted as a function of T_{eff}. The dashed line is the prediction of quantum optomechanics theory; the gray area shows the systematic uncertainty resulting from the calibration of the heterodyne signal. Each data point is produced from data and fits similar to Fig. 2 (averaged over 15 mK bins). Error bars indicate the statistical uncertainty in these fits.

are unlikely to arise from thermal effects (which would typically depend on T_{MC} and n_{circ}). Instead, this behavior is consistent with an imperfect calibration of the heterodyne signal (Supplemental Material [31]).

Figure 3(c) shows H_{AS}, H_{Re}, and H_{Im} as a function of T_{eff}. The points in Fig. 3(c) are derived from data and fits similar to those in Fig. 2 [and from the same set of measurements used to produce Figs. 3(a) and 3(b)]. The uncertainty grows at higher T_{eff} because of the rapid increase of γ_{ac} with T_{eff}, which makes the motional sidebands harder to distinguish from the noise floor. The uncertainty also grows at the lowest values of T_{eff} owing to the need to use low n_{circ}. The data in Fig. 3(c) are consistent with the theoretical prediction (dashed line), indicating their origin in the coherent quantum dynamics of the cavity's acoustic and optical modes.

In conclusion, we have isolated a single normal mode of a liquid body and measured its quantum fluctuations. This result is distinct from the large body of work on the

quantum aspects of superfluid He's bulk properties, which reflect the aggregate behavior of very many normal modes. It is also distinct from work on quantum effects directly related to the superfluid's wave function (such as persistent flow, quantized vortices, and Josephson effects); although superfluidity greatly facilitates the experiments described here by suppressing the viscous damping of the acoustic mode, the acoustic mode itself and its quantum dynamics are generic to any liquid.

A. B. S. and A. D. K. contributed equally to this work.

---

*Corresponding author.
jack.harris@yale.edu

[1] M. H. Devoret and R. J. Schoelkopf, Science **339**, 1169 (2013).

[2] D. M. Stamper-Kurn, *Cavity Optomechanics*, edited by M. Aspelmeyer, T. J. Kippenberg, and F. Marquardt (Springer, New York, 2014), pp. 283–325.

[3] T. Tabuchi, S. Ishino, A. Noguchi, T. Ishikawa, R. Yamazaki, K. Usami, and Y. Nakamura, Science **349**, 405 (2015).

[4] M. Aspelmeyer, T. J. Kippenberg, and F. Marquardt, Rev. Mod. Phys. **86**, 1391 (2014).

[5] M. Underwood, D. Mason, D. Lee, H. Xu, L. Jiang, A. B. Shkarin, K. Børkje, S. M. Girvin, and J. G. E. Harris, Phys. Rev. A **92**, 061801(R) (2015).

[6] T. P. Purdy, K. E. Grutter, K. Srinivasan, and J. M. Taylor, Science **356**, 1265 (2017).

[7] A. D. O'Connell, M. Hofheinz, M. Ansmann, R. C. Bialczak, M. Lenander, E. Lucero, M. Neeley, D. Sank, H. Wang, M. Weides, J. Wenner, J. Martinis, and A. N. Cleland, Nature (London) **464**, 697 (2010).

[8] T. A. Palomaki, J. D. Teufel, R. W. Simmonds, and K. W. Lehnert, Science **342**, 710 (2013).

[9] A. H. Safavi-Naeini, J. Chan, J. T. Hill, T. P. Mayer Alegre, A. Krause, and O. Painter, Phys. Rev. Lett. **108,** 033602 (2012).

[10] N. Brahms, T. Botter, S. Schreppler, D. W. C. Brooks, and D. M. Stamper-Kurn, Phys. Rev. Lett. **108,** 133601 (2012).

[11] T. P. Purdy, P. L. Yu, N. S. Kampel, R. W. Peterson, K. Cicak, R. W. Simmonds, and C. A. Regal, Phys. Rev. A **92,** 031802(R) (2015).

[12] D. A. Golter, T. Oo, M. Amezcua, K. A. Stewart, and H. Wang, Phys. Rev. Lett. **116,** 143602 (2016).

[13] C. B. Møller, R. A. Thomas, G. Vasilakis, E. Zeuthen, Y. Tsaturyan, K. Jensen, A. Schliesser, K. Hammerer, and E. S. Polzik, Nature (London) **547,** 191 (2017).

[14] J. Bochmann, A. Vainsencher, D. D. Awschalom, and A. N. Cleland, Nat. Phys. **9,** 712 (2013).

[15] R. W. Andrews, R. W. Peterson, T. P. Purdy, K. Cicak, R. W. Simmonds, C. A. Regal, and K. W. Lehnert, Nat. Phys. **10,** 321 (2014).

[16] F. Ya. Khalili, H. Miao, H. Yang, A. H. Safavi-Naeini, O. Painter, and Y. Chen, Phys. Rev. A **86,** 033840 (2012).

[17] A. J. Weinstein, C. U. Lei, E. E. Wollman, J. Suh, A. Metelmann, A. A. Clerk, and K. C. Schwab, Phys. Rev. X **4,** 041003 (2014).

[18] K. Børkje, Phys. Rev. A **94,** 043816 (2016).

[19] M. Bhattacharya, J. Opt. Soc. Am. B **32,** B55 (2015).

[20] L. Childress, M. P. Schmidt, A. D. Kashkanova, C. D. Brown, G. I. Harris, A. Aiello, F. Marquardt, and J. G. E. Harris, Phys. Rev. A **96,** 063842 (2017).

[21] S. A. Lyon, Phys. Rev. A **74,** 052338 (2006).

[22] P. M. Platzman and M. I. Dykman, Science **284,** 1967 (1999).

[23] L. A. De Lorenzo and K. C. Schwab, New J. Phys. **16,** 113020 (2014).

[24] A. D. Kashkanova, A. B. Shkarin, C. D. Brown, N. E. Flowers-Jacobs, L. Childress, S. W. Hoch, L. Hohmann, K. Ott, J. Reichel, and J. G. E. Harris, Nat. Phys. **13,** 74 (2017).

[25] G. I. Harris, D. L. McAuslan, E. Sheridan, Y. Sachkou, C. Baker, and W. P. Bowen, Nat. Phys. **12,** 788 (2016).

[26] F. Souris, X. Rojas, P. H. Kim, and J. P. Davis, Phys. Rev. Applied **7,** 044008 (2017).

[27] W. F. Vinen, M. Tsubota, and A. Mitani, Phys. Rev. Lett. **91,** 135301 (2003).

[28] E. Kozik and B. Svistunov, Phys. Rev. Lett. **92,** 035301 (2004).

[29] G. Bahl, K. H. Kim, W. Lee, J. Liu, X. Fan, and T. Carmon, Nat. Commun. **4,** 1994 (2013).

[30] S. Kaminski, L. L. Martin, S. Maayani, and T. Carmon, Nat. Photonics **10,** 758 (2016).

[31] See Supplemental Material at http://link.aps.org/supplemental/10.1103/PhysRevLett.122.153601 for details of the experimental apparatus, characterization measurements, calibration procedures, and theoretical modeling of the optical signals and thermal behavior, which includes Refs. [32–52].

[32] A. M. Jayich, J. C. Sankey, K. Børkje, D. Lee, C. Yang, M. Underwood, L. Childress, A. Petrenko, S. M. Girvin, and J. G. E. Harris, New J. Phys. **14,** 115018 (2012).

[33] K. Børkje, Phys. Rev. A **94,** 043816 (2016).

[34] A. D. Kashkanova, A. B. Shkarin, C. D. Brown, N. E. Flowers-Jacobs, L. Childress, S. W. Hoch, L. Hohmann, K. Ott, J. Reichel, and J. G. E. Harris, J. Opt. **19,** 034001 (2017).

[35] D. Hunger, C. Deutsch, R. J. Barbour, R. J. Warburton, and J. Reichel, AIP Adv. **2,** 012119 (2012).

[36] N. E. Flowers-Jacobs, S. W. Hoch, J. C. Sankey, A. D. Kashkanova, A. M. Jayich, C. Deutsch, J. Reichel, and J. G. E. Harris, Appl. Phys. Lett. **101,** 221109 (2012).

[37] A. D. Kashkanova, Yale University Ph.D. Thesis, 2017.

[38] H. J. Carmichael, J. Opt. Soc. Am. B **4,** 1588 (1987).

[39] A. A. Clerk, S. M. Girvin, F. Marquardt, R. J. Schoelkopf, and M. H. Devoret, Rev. Mod. Phys. **82,** 1155 (2010).

[40] J. Restrepo, J. Gabelli, C. Ciuti, and I. Favero, C. R. Phys. **12,** 860 (2011).

[41] LaserOptik GmbH (private communication).

[42] M. Sciacca, A. Sellitto, and D. Jou, Phys. Lett. A **378,** 2471 (2014).

[43] B. Bertman and T. A. Kitchens, Cryogenics **8,** 36 (1968).

[44] R. W. Whitworth, Proc. R. Soc. A **246,** 390 (1958).

[45] S. W. Van Sciver, *Helium Cryogenics* (Springer New York, New York, NY, 2012)

[46] H. E. Bennett and J. O. Porteus, J. Opt. Soc. Am. **51,** 123 (1961).

[47] F. Pobell, *Matter and methods at low temperatures* (Springer-Verlag, Berlin Heidelberg, 1961).

[48] V. Arp, Cryogenics **10,** 96 (1970).

[49] A. D. Pierce, *Acoustics* (McGraw-Hill Book Company, New York, NY, 1982).

[50] B. M. Abraham, Y. Eckstein, J. B. Ketterson, M. Kuchnir, and J. Vignos, Phys. Rev. **181,** 347 (1969).

[51] R. J. Donnelly and C. F. Barenghi, Phys. Rev. **27,** 1217 (1998).

[52] R. L. St. Peters, T. J. Greytak, and G. B. Benedek, Opt. Commun. **1,** 412 (1970).

[53] G. S. Agarwal and S. S. Jha, Phys. Rev. A **90,** 023812 (2014).

[54] S. Weis, R. Rivière, S. Deléglise, E. Gavartin, O. Arcizet, A. Schliesser, and T. J. Kippenberg, Science **330,** 1520 (2010).

[55] These measurements also provide a measure of the non-unitary photothermal effects in the system. As described in Sec. 3.4 of Ref. [31], they do not contribute appreciably to the measurements presented here.

[56] K. Børkje, A. Nunnenkamp, B. M. Zwickl, C. Yang, J. G. E. Harris, and S. M. Girvin, Phys. Rev. A **82,** 013818 (2010).

[57] The near absence of laser cooling in these measurements results because the two measurement tones are detuned symmetrically (relative to the cavity resonance) to within $\sim 0.01\,\kappa$, leading to cancellation of their dynamical back action. See Sec. 2.3 of Ref. [31] for details.

Quantum optomechanics in a liquid

A.B. Shkarin,[1] A.D. Kashkanova,[1] C. D. Brown,[1]
K. Ott,[2] S. Garcia,[2] J. Reichel,[3] and J. G. E. Harris[1,3]

[1]Department of Physics, Yale University, New Haven, CT, 06511, USA
[2]Laboratoire Kastler Brossel, ENS-Université PSL, CNRS, Sorbonne Université, Collège de France
24 rue Lhomond, 75005 Paris, France
[3]Department of Applied Physics, Yale University, New Haven, CT, 06511, USA

Contents

1 Supplementary Note 1: Measurement setup

The purpose of this section is to describe the experimental setup used in the experiment. A schematic of the setup is shown in Supplementary Figure 1.

1.1 Optical setup

Light is produced by a tunable laser (TL)[1] and passes through a circulator and a filter cavity (FC)[2]. The reflection from the FC is used to lock it to the frequency of the TL. Light transmitted through the FC passes through an IQ-modulator (IQM)[3] operating in the single sideband suppressed carrier mode. The IQM serves as a frequency shifter to lock the laser to the experimental cavity. The tone generated by the IQM is used as a local oscillator (LO) for the heterodyne detection.

After the IQM, the frequency-shifted light passes through a phase modulator (PM)[4]. The PM is driven by up to four different tones, originating from four microwave sources described in section 1.2.1. Each of these tones produces sidebands on the LO. The beams incident on the cavity during Brownian motion measurements are shown in Supplementary Figure 2. The relative power in all the sidebands as a function of the microwave signals driving the phase modulator was calibrated as described in section 1.3.3.

The light then goes through a variable attenuator. A 90:10 splitter sends 90% of light to the experimental cavity via a circulator; the remaining 10% is monitored to control the incident power. The power incident on the cavity and reflected from the cavity is calibrated using a 99:1 splitter immediately before the dilution refrigerator (DR)[5]. The light reflected from the cavity passes through the circulator and another 90:10 splitter, which sends 10% of the power onto a photodiode and 90% towards an Erbium Doped Fiber Amplifier (EDFA)[6], which amplifies the optical signal by a factor of 20-50 and adds ≈ 4 dB noise. The noise figure of the EDFA was calibrated as described in section 1.3.4.

The light leaving the EDFA goes through a broadband tunable filter (TF)[7], which is used to suppress the amplified spontaneous emission (ASE) noise from the EDFA. The filtered light then lands on a photodiode (PD)[8].

1.2 Microwave setup

It is convenient to separate the microwave setup into the generation part and the detection part.

1.2.1 Generation

Up to 4 microwave tones are used to drive the phase modulators:

- The Lock beam is used to lock the laser to the experimental cavity. The beam is generated using a lock-in amplifier (LIA)[9]. A tone at 200 MHz from the LIA is sent to a mix-up circuit. There it is mixed with a tone from a microwave generator (MWG1)[10] at 1,900 MHz. The mixed-up tone at $\omega_{\text{Lock}} = 2,100$ GHz is sent to the four-way splitter (4WS) where it is combined with other tones and then sent to the phase modulator.

---

[1] Pure Photonics PPCL200
[2] MicronOptics FFP-TF, $\kappa/2\pi = 30$ MHz, $\omega_{\text{FSR}}/2\pi = 15$ GHz
[3] EOspace QPSK modulator IQ-0DKS-25-PFA-PFA-LV-UL
[4] EOSpace phase modulator PM-0KS-10-PFA-PFAP-UL
[5] Janis DR500
[6] Nuphoton EDFA-CW-LNF-RS-10-40-FCA
[7] OzOptics TF100, 0.5 nm bandwidth
[8] Thorlabs DET08CFC
[9] Zurich Instruments UHF
[10] Vaunix Lab Brick LMS-232D
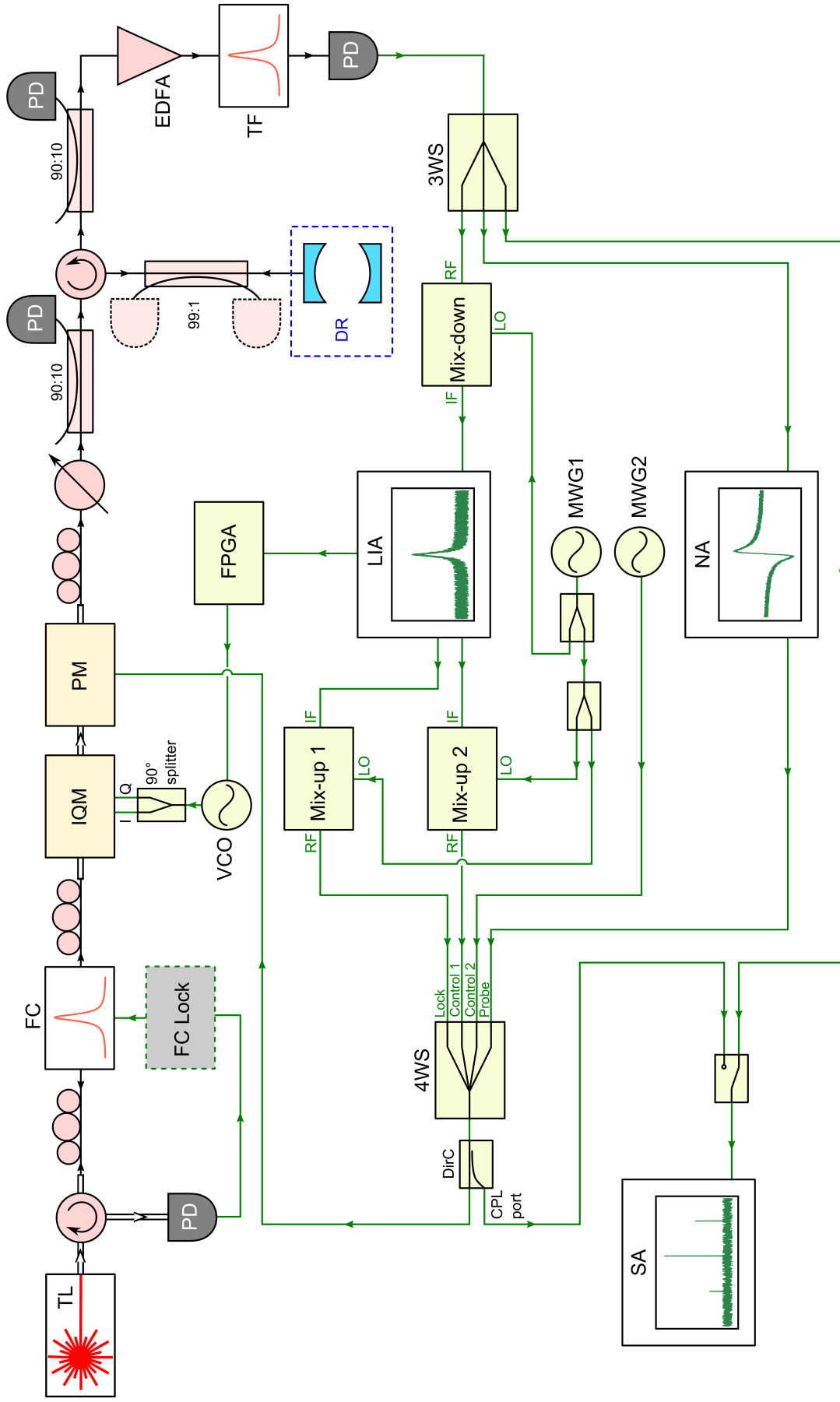
Supplementary Figure 1: Measurement setup. The optical and electronic components of the measurement scheme. Single mode fiber: black line. Polarization-maintaining fiber: double black lines. Electrical path: green lines. TL: tunable laser. FC: filter cavity. FC Lock: locking circuit for the filter cavity. IQM: IQ-modulator. PM: phase modulator. PD: photodiode. EDFA: erbium doped fiber amplifier. TF: tunable filter. DR: dilution refrigerator. 3WS: three-way splitter. NA: network analyzer. LIA: lock-in amplifier. SA: spectrum analyzer. MWG: microwave generator. FPGA: field programmable gate array. VCO: voltage controlled oscillator. 4WS: four-way splitter. DirC: directional coupler.
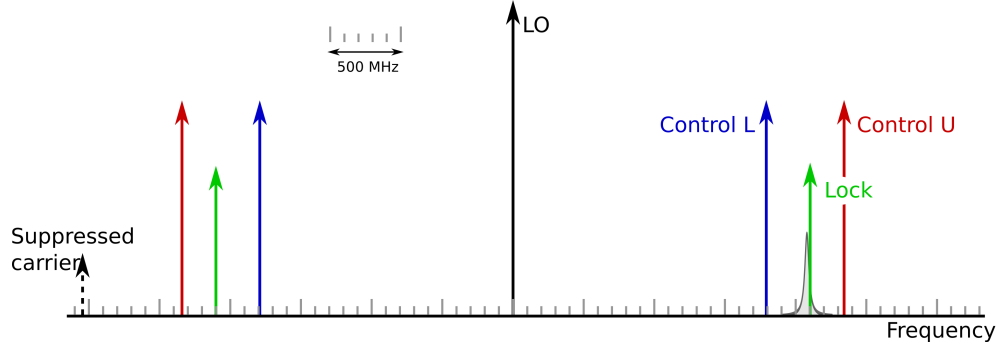
Supplementary Figure 2: Beams incident on the cavity during the Brownian motion measurement. The phase modulator (PM in Supplementary Figure 1) adds two control beams and one lock beam on either side of the local oscillator (LO) beam. The laser is locked to the cavity using one of the lock beams. The cavity lineshape is shown in gray.

- The Control 1 signal is used to generate one of the control beams. It is generated by the LIA at 529.343 MHz. This tone is mixed with the signal from MWG1 at $1,900$ MHz. The mixed up signal at $\omega_{\mathrm{Control1}} = 2,429.343$ MHz is sent to the 4WS.

- The Control 2 signal is used to generate the other control beam. It is generated directly by a different microwave generator (MWG2)[11] at $\omega_{\mathrm{Control2}} = 1,790.657$ MHz.

- The Probe signal is only on for the OMIT/A measurements. It is generated by the network analyzer (NA)[12] at a frequency $\omega_{\mathrm{Control(1,2)}} \pm \omega_{\mathrm{ac}} \pm \delta$, where $\omega_{\mathrm{ac}} = 319.243$ MHz is the frequency of the acoustic mode, and $\delta \approx 100$ kHz.

The signal out of the 4WS is split and a small portion is sent to a spectrum analyzer (SA)[13], where the spectrum is recorded. This is done to measure the power in all the microwave tones incident on the PM.

For the Brownian motion measurements, the control signals are filtered with high pass filter for Control 1 and low pass filter for Control 2. The filters are placed before the PM to block microwave noise that would produce laser noise near the cavity resonance frequency.

For the OMIT/A measurements only one control beam and a probe beam are on. The frequency of the control beam is swept, as described in the main text. The probe beam's detuning is varied as described above.

The typical optical powers in the measurements are:

- $P_{\mathrm{Control1}} \approx P_{\mathrm{Control2}} \approx 0.1 P_{\mathrm{total}}$

- $P_{\mathrm{Lock}} \approx 10^{-6} P_{\mathrm{total}}$

- $P_{\mathrm{Probe}} \approx 10^{-5} P_{\mathrm{total}}$

- $P_{\mathrm{LO}} \approx 0.8 P_{\mathrm{total}}$

The total incident power P_{total} is up to 100 μW.

1.2.2 Detection

A heterodyne detection scheme is used. The signal from the PD consists primarily of beating between the LO and the sidebands. These beat notes occur at $2,100$ MHz (Lock), $2,429.343$ MHz (Control 1), $1,790.657$ MHz (Control 2), and $2,110 \pm 0.1$ MHz (motional sidebands of the control beams). The signal is sent to a three-way splitter (3WS).

---

[11]Vaunix Lab Brick LMS-232D
[12]Keysight HP 8722D
[13]Rigol DSA1030A

The first part is mixed down with the signal from MWG1 (at $1,900$ MHz). During the Brownian motion measurements, the mixed-down signal is dominated by 5 frequencies: 200 MHz (Lock), 529.343 MHz (Control 1), 109.343 MHz (Control 2), and 210 ± 0.1 MHz (motional sidebands of the control beams). It is sent to the LIA, where the spectra at $210 + 0.1$ MHz and $210 - 0.1$ MHz are recorded. The quadratures of the signal at 200 MHz are sent to a field programmable gate array (FPGA)[14], which uses them to generate an error signal, which is then sent to the voltage controlled oscillator (VCO) to vary its output frequency between 3 GHz and 3.5 GHz in order to lock the laser to the experimental cavity. The Lock beam is typically detuned by ≈ 10 MHz from the cavity resonance, as indicated in Supplementary Figure 2.

The second part is sent to the NA. It gives the response at the probe beam frequency when the probe beam is on (i.e. for OMIT/A measurements).

The third part is sent to the SA to record the spectrum of the light coming from the experimental cavity.

1.3 Calibrations

1.3.1 Power calibrations

The power incident on the cavity is found as the geometric mean of the incident and reflected powers measured at the 99:1 splitter.

1.3.2 Classical noise calibrations

For the measurements of the acoustic mode's fluctuations (Figures 2 and 3 in the main text) there are three potentially relevant sources of classical noise.

Two of these sources (the EDFA output noise and the detector electronic noise) result in a frequency-independent background for $S_{ii}^{(\mathrm{rr})}$, $S_{ii}^{(\mathrm{bb})}$, and $S_{ii}^{(\mathrm{rb})}$. For $S_{ii}^{(\mathrm{rr})}$ and $S_{ii}^{(\mathrm{bb})}$ this background averages to a non-zero value (which is subtracted from the data shown in Fig. 2), while for $S_{ii}^{(\mathrm{rb})}$ this background averages to zero. The contribution of the EDFA output noise is discussed in Section 1.3.4. The detector electronic noise is never more than 2% of the total noise background.

The third potentially relevant source is the laser's classical noise. This noise can drive the acoustic motion while also contributing to the measurement background. The resulting correlation can produce sideband asymmetry which is unrelated to the quantum effects that are the main focus of this paper (for an in-depth discussion, see [37, 38]). To estimate the possible impact of this effect, the laser's classical noise was characterized in two ways.

First, the laser was measured directly after the filter cavity. It was found that the classical noise at frequencies near 300 MHz was predominantly phase noise, and was smaller than the quantum noise ($C_{\mathrm{yy}} < 1/4$ in the terminology of [37]) for powers less than ≈ 200 μW. However in the measurements of the acoustic mode's fluctuations described in the main paper, the laser beam passes through a number of additional elements after the filter cavity (Supplementary Figure 1), and these elements may add classical noise to the laser. Analysis of the noise floor in the heterodyne data suggests that the classical noise after these elements is smaller than the quantum noise for laser powers less than ≈ 40 μW.

For all of the data shown in Figures 2 and 3 the total power in the control beams was < 8 μW. As a result, the impact of classical laser noise is expected to be small. Specifically, for a system in the sideband-resolved limit (as is the case for the present device) classical phase noise is expected to produce a sideband asymmetry roughly equal to $\kappa_{\mathrm{ext}}/\kappa$ fraction (which is approximately one half in our system) of the ratio of the classical noise to the quantum noise. For the data in Fig. 3, this amounts to $< 10\%$.

---

[14]National Instruments FPGA NI PXI-7854R
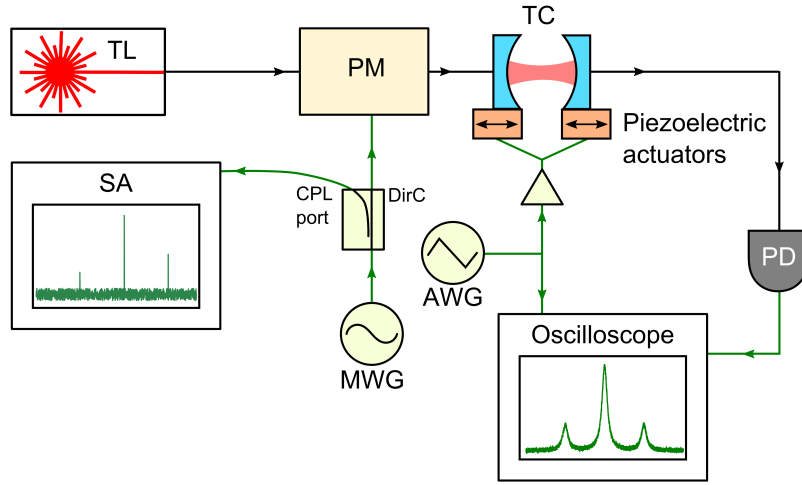
Supplementary Figure 3: Calibration of the phase modulator. Black lines: single mode fiber. Green lines: electrical path. TL: tunable laser. PM: phase modulator. TC: tunable cavity. PD: photodiode. AWG: arbitrary wave generator. MWG: microwave generator. SA: spectrum analyzer. DirC: directional coupler.

1.3.3   Calibration of the phase modulator

The relative optical power in the beams after the phase modulator is calibrated using the setup shown in Supplementary Figure 3.

Light from the TL passes through the PM and a tunable cavity (TC)[15], which acts as an optical spectrum analyzer; the light transmitted through the TC lands on the PD. The PM is driven by a microwave generator (MWG)[16] with varying frequency and power. The SA records the power in the CPL port of the directional coupler (DirC), which is used in the actual experiment. The TC length is swept by applying a triangle wave from the arbitrary wave generator (AWG) to piezoelectric elements within the TC. The TC transmission is fit to a Lorentzian with two sidebands:

$$f(x) = \frac{E_0}{x^2 + (\kappa/2)^2} + \frac{E_1}{(x - d_{\mathrm{sb}})^2 + (\kappa/2)^2} + \frac{E_1}{(x + d_{\mathrm{sb}})^2 + (\kappa/2)^2} \tag{1}$$

The ratio of the sidebands to the carrier is recorded (as a function of microwave drive power and frequency). This ratio is expected to be:

$$\frac{E_1}{E_0} = \frac{J_1(\pi V_{\mathrm{rel}})^2}{J_0(\pi V_{\mathrm{rel}})^2} \tag{2}$$

Here J_0 and J_1 are Bessel functions of order 0 and 1. The drive voltage amplitude relative to the half-wave voltage V_π is:

$$V_{\mathrm{rel}} = \frac{V}{V_\pi} = \left(\frac{P}{P_\pi}\right)^{1/2} = 10^{(P_{\mathrm{dBm}} - P_{\pi\mathrm{dBm}})/20} \tag{3}$$

Here V is the voltage sent to the phase modulator; the half-wave voltage V_π is the voltage necessary to induce a phase change of π. The values P and P_π are the corresponding powers in Watts and the value P_{dBm} and $P_{\pi\mathrm{dBm}}$ are the corresponding powers in dBm. The value of $P_{\pi\mathrm{dBm}}$ is given relative to the CPL port of the DirC, as that is what is measured during the experiment. This value is independent of microwave power, but varies with microwave frequency. We record its values for frequencies between 1,400 and 3,000 MHz, as that is the range of the microwave tones.

During the experiment the optical power in the first order sideband, relative to the total power, is given by $J_1(\pi V_{\mathrm{rel}})^2$, where $P_{\pi\mathrm{dBm}}$ is known from the calibration and P_{dBm} is measured for each microwave tone using the SA.

---

[15]Homebuilt, $\kappa/2\pi = 200$ MHz, $\omega_{\mathrm{FSR}}/2\pi = 1.5$ THz
[16]Agilent N9310A
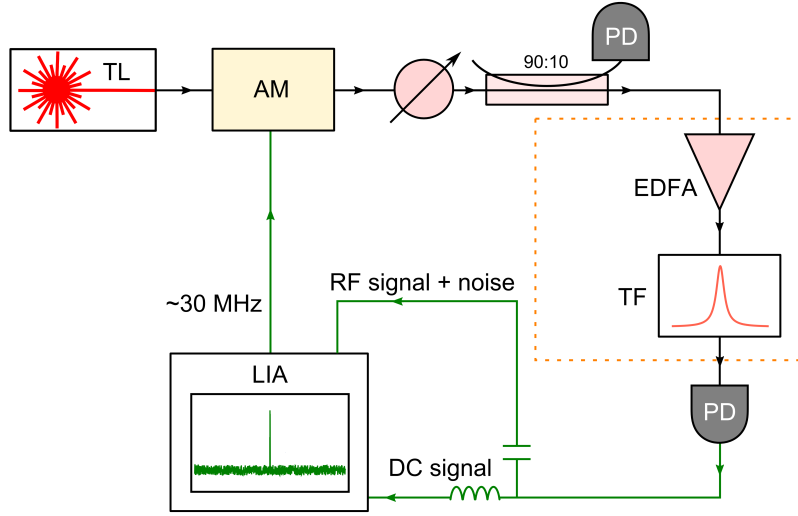
Supplementary Figure 4: Calibration of the EDFA noise. Black lines: single mode fiber. Green lines: electrical path. TL: tunable laser. AM: amplitude modulator. PD: photodiode. EDFA: erbium doped fiber amplifier. TF: tunable filter. LIA: lock-in amplifier.

1.3.4 EDFA noise figure calibration

The EDFA noise figure is calibrated as shown in Supplementary Figure 4.

Light leaving the TL passes through an amplitude modulator (AM)[17], which puts small sidebands ("signal") onto the beam. The amplitude modulator is driven at ≈ 30 MHz. At this frequency the laser amplitude noise is lower than shot noise, and the photodiode gain is within 5 % of the DC photodiode gain. Light then passes through a variable attenuator and a 90:10 splitter, which is used to monitor the incident power. Then it either goes directly onto the PD, or passes through the EDFA and TF first. During the measurement, the power of the AM sidebands and the background power spectral density are recorded as the incident laser power is changed using the attenuator. The ratio of the sideband power to the background gives the signal-to-noise ratio. The DC signal gives the record of laser power.

The gain of the photodiode and the laser noise are calibrated without the EDFA first (i.e., without the components inside the dashed orange square in Supplementary Figure 4). The background grows linearly with increasing laser power, as expected for shot noise. The power of the AM sidebands grows quadratically. This measurement gives SNR_0, the signal-to-noise ratio without the EDFA.

Then the EDFA and TF are put in, and the signal-to-noise ratio is measured again (SNR_{EDFA}). The noise figure of the EFDA is calculated as:

$$\text{NF} = 10 \log_{10} \left(\frac{\text{SNR}_0}{\text{SNR}_{\text{EDFA}}} \right) \tag{4}$$

NF was found to vary slightly with laser wavelength, so we measured it for a number of different wavelengths. For 1,529.7 nm (the wavelength used for the Brownian motion measurements), the EDFA noise figure is 4 dB for laser powers below 30 μW. For laser powers below 100 μW (the maximum used in the experiment), the noise figure is smaller than 4.5 dB.

---

[17]Thorlabs LN81S

2 Supplementary Note 2: Methods

2.1 Device construction

The device used in this study is similar to the device described in Refs. 22 and 39. It consists of a cavity formed between the end faces of two optical fibers. The fibers' end faces are laser-machined to have concave surfaces, and each surface is coated with a high reflectivity dielectric distributed Bragg reflector (DBR) [40]. The fibers are aligned in a pair of glass ferrules [41] which are epoxied to a glass plate (shown as orange in Fig. 1a in the main text). The glass plate is epoxied inside a Cu cell, which is bolted to the mixing chamber of a dilution refrigerator. Liquid He is introduced to the cell via a capillary tube. The capillary is heat sunk at each stage of the refrigerator and includes a silver sinter heat exchanger at the mixing chamber.

In contrast with the device described in Refs. 22 and [39] (in which the fibers were aligned in a single ferrule), the present device's use of two separate ferrules greatly improves the thermal link between the He in the cavity and the mixing chamber. Further details are given in Supplementary Note 5.

The cavity length is $L = 69.1$ μm. The two DBR reflectivities are $R_1 = 0.99995$ and $R_2 = 0.99999$. Light is coupled to and collected from the cavity via the lower-reflectivity DBR.
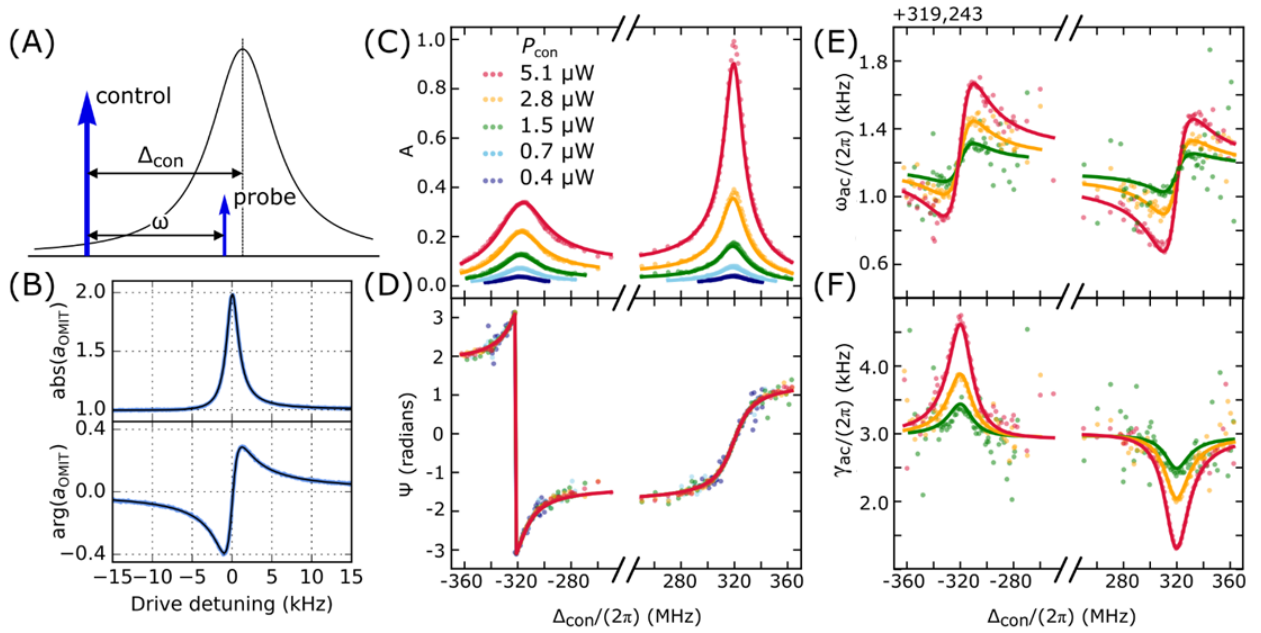
2.2 OMIT/A characterization

For OMIT/A measurements, three laser beams drive the cavity: a weak ("probe") beam, a stronger ("control") beam, and a far-detuned local oscillator ("LO") beam (Supplementary Figure 5 (a)). Beating between the probe and control beams causes the intracavity optical intensity to oscillate, thereby driving the acoustic mode. The resulting oscillation of the acoustic mode then adds sidebands to these beams. One sideband from the control beam interferes with the probe beam; as a result, a heterodyne measurement of the reflected probe (made using the LO) provides information about the acoustic mode's driven motion [22, 30]. The OMIT/A measurement scheme and analysis are described in detail in Ref. 22.

Supplementary Figure 5(b) shows a typical OMIT/A spectrum in which the probe beam's detuning is varied while keeping the control beam's detuning fixed, thereby varying the frequency ω of the drive applied to the acoustic mode. The heterodyne signal is fit to a complex Lorentzian with a constant background: $a_{\mathrm{OMIT}}[\omega] = a_{\mathrm{bg}} + a_{\mathrm{lor}}/(\gamma_{\mathrm{ac}}/2 + i(\omega - \omega_{\mathrm{ac}}))$, where a_{bg} and a_{lor} are both complex. This fit returns values for a_{bg}, a_{lor}, and the acoustic linewidth γ_{ac} and frequency ω_{ac}. Note that when $\bar{n} > 0$ the optomechanical interaction H_{OM} can shift γ_{ac} and ω_{ac} from their bare values [4] $\gamma_{\mathrm{ac},0}$ and $\omega_{\mathrm{ac},0}$.

An OMIT/A spectrum (such as the one shown in Supplementary Figure 5(b)) can be characterized by its magnitude $A \equiv \mathrm{abs}(X)$ and phase $\Psi \equiv \arg(X)$, where $X \equiv 2a_{\mathrm{lor}}/\gamma_{\mathrm{ac}}a_{\mathrm{bg}}$. Supplementary Figure 5(c,d) shows A and Ψ (derived from the best-fit values of a_{bg}, a_{lor}, and γ_{ac}) as a function of the control beam's detuning Δ_{con} and power P_{con}. Both A and Ψ show a feature of width $\sim \kappa$ centered at $\Delta_{\mathrm{con}} \sim \pm\omega_{\mathrm{ac}}$, corresponding to the probe being resonant with the optical cavity. Supplementary Figure 5(e,f) shows $\omega_{\mathrm{ac}}(\Delta_{\mathrm{con}}, P_{\mathrm{con}})$ and $\gamma_{\mathrm{ac}}(\Delta_{\mathrm{con}}, P_{\mathrm{con}})$, which exhibit the standard optical spring and damping[4].

(For the measurements of thermal and quantum fluctuations shown in Figs. 2, 3 the strong control beam is turned off. As a result the optical spring and damping effects are much weaker in those measurements.)

The solid lines in Supplementary Figure 5(c-f) are the result of fitting all the OMIT/A data to the dynamical backaction model described in Ref. 22. The two fitting parameters are $g^{(0)}$, which represents the unitary electrostrictive interaction between the cavity mode and the acoustic mode; and $g_{\mathrm{pt}}^{(0)}$, which represents an additional optomechanical interaction with a 90° phase lag between the optical intensity and the resulting force on the acoustic mode. As described in Ref. 22, this arises from a photothermal effect in which optical absorption in the DBRs drives the acoustic mode, but with a bandwidth much less than ω_{ac}. The best-fit values are $g^{(0)} = 2\pi \times (3.6 \pm 0.1)$ kHz and $g_{\mathrm{pt}}^{(0)} = 2\pi \times (0.8 \pm 0.1)$ kHz. This is

Supplementary Figure 5: Optomechanical characterization. (a) Illustration of the OMIT/A measurement scheme. Black curve: the cavity lineshape. Blue arrows: the "probe" and "control" laser tones (the far-detuned local oscillator tone is not shown). (b) Typical OMIT/A measurement ($\Delta_{\mathrm{con}} = 2\pi \times 320$ MHz, $P_{\mathrm{con}} = 5.1$ μW). Upper panel: abs(a_{OMIT}) normalized so that the background $a_{\mathrm{bg}} = 1$. Lower panel: arg(a_{OMIT}). Both are shown as a function of the beat note frequency ω. The black line is the fit described in the text. The subsequent panels show the four parameters extracted from this type of fit, all as a function of Δ_{con} and P_{con}. (c) Amplitude of the OMIT/A signal A. (d) Phase of the OMIT/A signal Ψ. (e) Acoustic mode resonance frequency ω_{ac}. (f) Acoustic mode damping rate γ_{ac}. The solid lines in (c) – (f) are a single fit to all the data shown, using the model described in Ref. 22. The only free parameters are the unitary optomechanical coupling rate and the photothermal optomechanical coupling rate defined in Ref. 22. For all of these measurements, 25 mK$< T_{\mathrm{MC}} < 60$ mK.

consistent with the *a priori* calculation [42] $g^{(0)} = 2\pi \times (3.9 \pm 0.2)$ kHz (where the error is due to uncertainty in the mirrors' materials properties) and the value $g^{(0)} = 2\pi \times (0.97 \pm 0.05)$ kHz found in a similar device [22].

2.3 Procedure for measuring undriven motion

As described in the main text and in section 1, measurements of the acoustic mode's thermal and quantum fluctuations are carried out by driving the cavity with two measurement beams. Conceptually, this measurement is simplest when these two beams have equal power and are symmetrically detuned about the cavity resonance. Here we describe the procedure used to approximate this ideal situation.

As described in section 1, all of the optical beams are generated by driving the PM with microwave tones. As a result, all the relative detunings between the optical beams are known precisely. To measure their detuning with respect to the cavity resonance, we produce an auxiliary beam and record its reflection from the cavity as we sweep the (microwave) frequency used to produce it. We fit this data to extract the (microwave) frequency ω_{aux} that produces a beam resonant with the cavity. The difference $\omega_{\mathrm{aux}} - \omega_{\mathrm{Lock}}$ then provides the offset between the Lock beam and the cavity resonance (~ 10 MHz).

This procedure is used to determine ω_{aux} before each measurement of the acoustic mode's fluctuations (i.e., before each measurement represented as a small data point in Figure 3 (a,b) of the main text). The measured detuning value $\omega_{\mathrm{aux}} - \omega_{\mathrm{Lock}}$ is subsequently used in the analysis of the Brownian motion measurements. Furthermore, once every

several measurements the cavity lock parameters were adjusted to minimize the difference $|\omega_{\mathrm{aux}} - \omega_{\mathrm{ControlC}}|$, where $\omega_{\mathrm{ControlC}} = (\omega_{\mathrm{Control1}} + \omega_{\mathrm{Control2}})/2$ is the center point between the two control MW tones (which is, consequently, the center point between the two measured Brownian motion peaks).
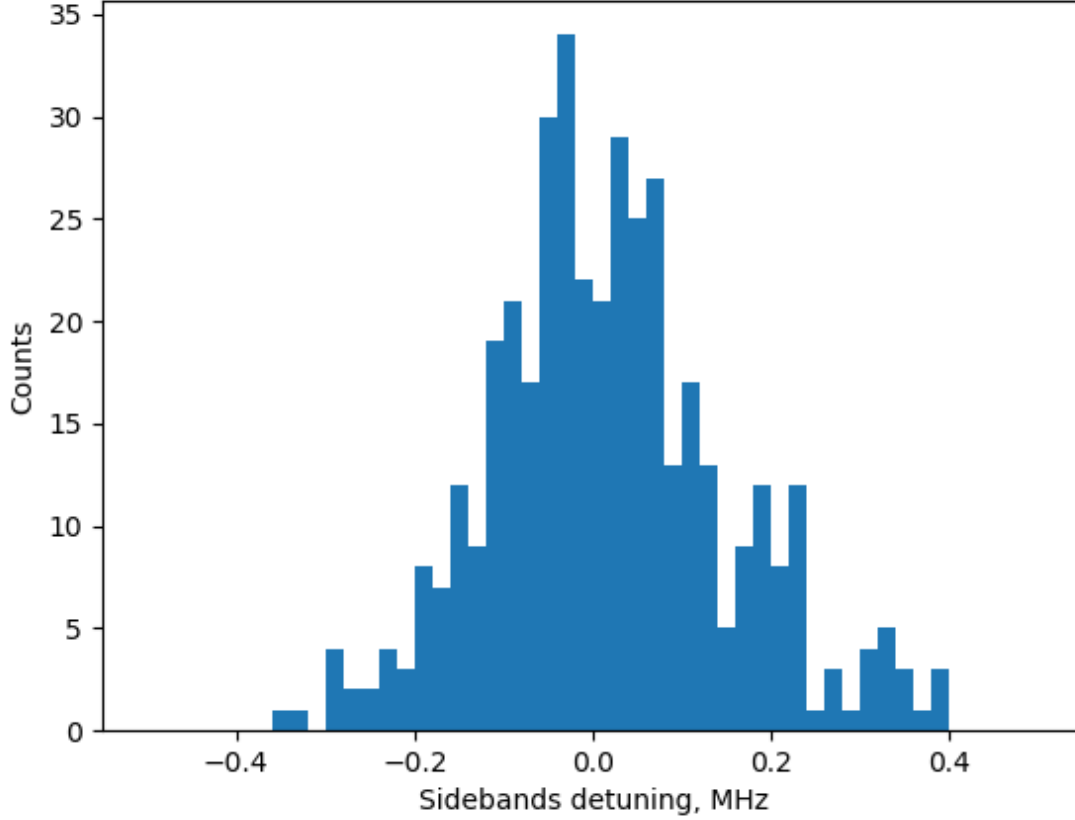
Supplementary Figure 6: Histogram of the difference $\omega_{\mathrm{aux}} - \omega_{\mathrm{ControlC}}$ between the cavity resonance frequency and the midpoint between the two control beams.

Supplementary Figure 6 shows the histogram of the measured variations in ω_{aux} across the data set used to produce Figure 3 of the main text. This figure indicates that the two measurement tones are symmetric with respect to the cavity resonance to ~ 0.2 MHz. For each small data point shown in Fig. 3 (a,b), the corresponding variation in ω_{aux} was included in the analysis; however, this produced no appreciable effect on the sideband asymmetry / correlation factors H_{AS}, H_{Re}, and H_{Im}.

The power in the two control tones was inferred by conducting an OMIT/A measurement. These are similar to the ones shown in Supplementary Figure 5 (b), with the measurement beam of the fluctuation setup serving as the "control" beam for this OMIT/A measurement (and an auxiliary beam serving as the "probe" beam). Fitting the OMIT/A data gives the optomechanical cooperativity for each measurement beam, which is used to infer each beam's power. Such a measurement was carried out for every Brownian motion measurement (i.e., for every small data points in Figure 3 (a,b) of the main text). The measured variations in the beam powers were incorporated in the analysis; however (as with the measured detuning asymmetry) this produced no appreciable effect on the sideband asymmetry and correlation factors.

3 Supplementary Note 3: Theoretical description of the measurement results

3.1 Two tone measurement scheme

Here we consider a standard optomechanical system in which the two motional sidebands are measured using two beams detuned by $\pm\omega_{\mathrm{ac}}$ from the cavity resonance.

The standard optomechanical Hamiltonian is

$$\hat{\mathcal{H}} = \hbar\omega_{\mathrm{opt}}\hat{a}^\dagger\hat{a} + \hbar\omega_{\mathrm{ac}}\hat{c}^\dagger\hat{c} + \hbar g^{(0)}(\hat{c}^\dagger + \hat{c})\hat{a}^\dagger\hat{a} + \hat{\mathcal{H}}_{\mathrm{env}}, \tag{5}$$

where $\hat{a}$ and $\hat{c}$ are annihilation operators for the optical and the acoustic modes respectively, ω_{opt} is the optical mode frequency (at zero acoustic mode amplitude), ω_{ac} is the acoustic mode frequency, and $g^{(0)}$ is the single-photon optomechanical coupling constant, i.e., the optical mode detuning per acoustic displacement equal to the acoustic zero-point fluctuations. Finally, $\hat{\mathcal{H}}_{\mathrm{env}}$ is the part of the Hamiltonian corresponding to the coupling to the environment (including both optical and acoustic mode noise and damping as well as the coherent optical drives). This Hamiltonian leads to the equations of motion

$$\dot{\hat{a}} = -\left(\frac{\kappa}{2} + i\omega_{\mathrm{opt}}\right)\hat{a} - ig^{(0)}(\hat{c}^\dagger + \hat{c})\hat{a} + \sqrt{\kappa_{\mathrm{int}}}\hat{\xi}_{\mathrm{int}} + \sqrt{\kappa_{\mathrm{ext}}}(a_{\mathrm{ext}} + \hat{\xi}_{\mathrm{ext}}) \tag{6}$$

$$\dot{\hat{c}} = -\left(\frac{\gamma_{\mathrm{ac}}}{2} + i\omega_{\mathrm{ac}}\right)\hat{c} - ig^{(0)}\hat{a}^\dagger\hat{a} + \sqrt{\gamma_{\mathrm{ac}}}\hat{\eta} \tag{7}$$

Here κ_{ext} and κ_{int} are the external and internal coupling rates for the optical mode with $\hat{\xi}_{\mathrm{ext}}$ and $\hat{\xi}_{\mathrm{int}}$ being the corresponding optical noise operators, $\kappa = \kappa_{\mathrm{int}} + \kappa_{\mathrm{ext}}$ is the total optical damping rate, a_{ext} denotes the optical drive, and γ_{ac} is the acoustic damping rate with the noise operator $\hat{\eta}$. The noise operators' correlations satisfy

$$\left\langle \hat{\xi}_i(t)\hat{\xi}_j(t') \right\rangle = 0 \tag{8}$$

$$\left\langle \hat{\xi}_i^\dagger(t)\hat{\xi}_j(t') \right\rangle = 0 \tag{9}$$

$$\left\langle \hat{\xi}_i(t)\hat{\xi}_j^\dagger(t') \right\rangle = \delta_{i,j}\delta(t-t') \tag{10}$$

$$\left\langle \hat{\eta}(t)\hat{\eta}(t') \right\rangle = 0 \tag{11}$$

$$\left\langle \hat{\eta}^\dagger(t)\hat{\eta}(t') \right\rangle = n_{\mathrm{th}}\delta(t-t') \tag{12}$$

$$\left\langle \hat{\eta}(t)\hat{\eta}^\dagger(t') \right\rangle = (n_{\mathrm{th}} + 1)\delta(t-t'), \tag{13}$$

The subscripts "i" and "j" stand for either "int" or "ext", and $n_{\mathrm{th}} = (e^{\hbar\omega_{\mathrm{ac}}/k_{\mathrm{B}}T} - 1)^{-1}$ is the thermal occupation of the acoustic mode bath (we assume that $\gamma_{\mathrm{ac}} \ll \omega_{\mathrm{ac}}$, so that the frequency dependence of n_{th} can be disregarded).

To simplify equation (6), we can switch to a rotating frame for the optical mode to cancel the bare resonance frequency: $\hat{a} \to \hat{a}e^{-i\omega_{\mathrm{opt}}t}$, with the corresponding transformations for $\hat{\xi}_{\mathrm{int}}$, $\hat{\xi}_{\mathrm{ext}}$ and a_{ext}. This doesn't affect correlation relations for the noise operators, since they are δ-correlated. The equation of motion for the acoustic mode stays the same, while the optical one becomes

$$\dot{\hat{a}} = -\frac{\kappa}{2}\hat{a} - ig^{(0)}(\hat{c}^\dagger + \hat{c})\hat{a} + \sqrt{\kappa_{\mathrm{int}}}\hat{\xi}_{\mathrm{int}} + \sqrt{\kappa_{\mathrm{ext}}}(a_{\mathrm{ext}} + \hat{\xi}_{\mathrm{ext}}) \tag{14}$$

Next, we specify the optical drive. We assume that it is comprised of two tones which we will call "lower" and "upper", with the corresponding detunings Δ_ℓ and Δ_{u}; the later discussion will assume that $\Delta_\ell \approx -\omega_{\mathrm{ac}}$ and $\Delta_{\mathrm{u}} \approx +\omega_{\mathrm{ac}}$. Denoting the tones' amplitudes by $a_{\mathrm{ext},\ell}$ and $a_{\mathrm{ext,u}}$, we can express the drive as $a_{\mathrm{ext}} = a_{\mathrm{ext},\ell}e^{-i\Delta_\ell t} + a_{\mathrm{ext,u}}e^{-i\Delta_{\mathrm{u}}t}$.

After that, we apply the usual expansion of $\hat{a}$ in powers of $g^{(0)}$. The zeroth order only includes the coherent drive and not the vacuum noise, and results in the equations of motion

$$\dot{a}_0 = -\frac{\kappa}{2}a_0 - ig^{(0)}(c_0 + c_0^*)a_0 + \sqrt{\kappa_{\text{ext}}}a_{\text{ext}} \tag{15}$$

$$\dot{c}_0 = -\left(\frac{\gamma_{\text{ac}}}{2} + i\omega_{\text{ac}}\right)c_0 - ig^{(0)}a_0^*a_0 \tag{16}$$

The radiation pressure force in the second equation $-ig^{(0)}a_0^*a_0$ has two components: one static and one at frequency $|\Delta_{\text{u}} - \Delta_\ell| \approx 2\omega_{\text{ac}}$. Since both of these are far away from the acoustic mode resonance, and the radiation pressure force is relatively small, we can ignore them in our case and simply assume $c_0 = 0$. To put it more quantitatively, these forces result in a dimensionless acoustic mode displacement on the order of $z_0 \approx \frac{g^{(0)}}{\omega_{\text{ac}}}n_{\text{c}}$, where $n_{\text{c}} = \overline{|a_0|^2}$ is the average intracavity photon number. We can ignore this displacement when considering the optical mode if its contribution to the cavity detuning is less than a cavity linewidth: $z_0 g^{(0)} \ll \kappa$, which results in $n_{\text{c}} \ll \frac{\kappa\omega_{\text{ac}}}{(g^{(0)})^2}$. For our system this bound is about $4 \cdot 10^8$, which is much higher than the maximum circulating photon number used in the experiment $n_{\text{c}} \lesssim 10^4$. Thus, ignoring the static acoustic mode displacement is justified, and the zeroth order solution for the optical mode becomes

$$a_0 = a_{0,\ell}e^{-i\Delta_\ell t} + a_{0,\text{u}}e^{-i\Delta_{\text{u}}t} \tag{17}$$

$$a_{0,\ell} = \frac{\sqrt{\kappa_{\text{ext}}}a_{\text{ext},\ell}}{\kappa/2 - i\Delta_\ell} \tag{18}$$

$$a_{0,\text{u}} = \frac{\sqrt{\kappa_{\text{ext}}}a_{\text{ext},\text{u}}}{\kappa/2 - i\Delta_{\text{u}}} \tag{19}$$

Next, the linearized equations of motion are

$$\dot{\hat{d}} = -\frac{\kappa}{2}\hat{d} - ig^{(0)}(\hat{c}^\dagger + \hat{c})a_0 + \sqrt{\kappa_{\text{int}}}\hat{\xi}_{\text{int}} + \sqrt{\kappa_{\text{ext}}}\hat{\xi}_{\text{ext}} \tag{20}$$

$$\dot{\hat{c}} = -\left(\frac{\gamma_{\text{ac}}}{2} + i\omega_{\text{ac}}\right)\hat{c} - ig^{(0)}(a_0^*\hat{d} + \hat{d}^\dagger a_0) + \sqrt{\gamma_{\text{ac}}}\hat{\eta}, \tag{21}$$

where $\hat{d}$ and $\hat{c}$ are the first order expansion terms for the optical and acoustic modes respectively.

It is convenient to introduce a combined vacuum noise operator

$$\hat{\xi} = (\sqrt{\kappa_{\text{ext}}}\hat{\xi}_{\text{ext}} + \sqrt{\kappa_{\text{int}}}\hat{\xi}_{\text{int}})/\sqrt{\kappa} \tag{22}$$

Because $\kappa_{\text{int}} + \kappa_{\text{ext}} = \kappa$, this operator has the same correlation properties (8-10) as $\hat{\xi}_{\text{int,ext}}$. Equation (20) for the optical mode can be rewritten as

$$\dot{\hat{d}} = -\frac{\kappa}{2}\hat{d} - ig^{(0)}(\hat{c}^\dagger + \hat{c})a_0 + \sqrt{\kappa}\hat{\xi} \tag{23}$$

The first order equations are linear in $\hat{c}$ and $\hat{d}$, so we can solve them via Fourier transform, which is defined as

$$\hat{x}[\omega] = \lim_{T \to \infty} \frac{1}{\sqrt{T}} \int_{-T/2}^{T/2} \hat{x}(t)e^{i\omega t}dt, \tag{24}$$

so that the noise correlators become

$$\left\langle \hat{\xi}[\omega]\hat{\xi}[-\omega] \right\rangle = \left\langle \hat{\xi}^\dagger[\omega]\hat{\xi}[-\omega] \right\rangle = 0 \tag{25}$$

$$\left\langle \hat{\xi}[\omega]\hat{\xi}^\dagger[-\omega] \right\rangle = 1 \tag{26}$$

$$\langle \hat{\eta}[\omega]\hat{\eta}[-\omega] \rangle = 0 \tag{27}$$

$$\left\langle \hat{\eta}^\dagger[\omega]\hat{\eta}[-\omega] \right\rangle = n_{\text{th}} \tag{28}$$

$$\left\langle \hat{\eta}[\omega]\hat{\eta}^\dagger[-\omega] \right\rangle = n_{\text{th}} + 1 \tag{29}$$

13

Note that in this notation the Hermitian conjugate is applied before the Fourier transform: $\hat{x}^\dagger[\omega] = (\hat{x}[-\omega])^\dagger$.

In the Fourier domain the equations of motion become

$$
\left(\frac{\kappa}{2} - i\omega\right)\hat{d}[\omega] = -ig^{(0)}\left(a_{0,\ell}\left(\hat{c}[\omega - \Delta_\ell] + \hat{c}^\dagger[\omega - \Delta_\ell]\right) + a_{0,\mathrm{u}}\left(\hat{c}[\omega - \Delta_\mathrm{u}] + \hat{c}^\dagger[\omega - \Delta_\mathrm{u}]\right)\right)
$$
$$
+\sqrt{\kappa}\hat{\xi}[\omega] \tag{30}
$$
$$
\left(\frac{\gamma_{\mathrm{ac}}}{2} - i(\omega - \omega_{\mathrm{ac}})\right)\hat{c}[\omega] = -ig^{(0)}\left(a_{0,\ell}^*\hat{d}[\omega + \Delta_\ell] + a_{0,\mathrm{u}}^*\hat{d}[\omega + \Delta_\mathrm{u}] + a_{0,\ell}\hat{d}^\dagger[\omega - \Delta_\ell] + a_{0,\mathrm{u}}\hat{d}^\dagger[\omega - \Delta_\mathrm{u}]\right)
$$
$$
+\sqrt{\gamma_{\mathrm{ac}}}\hat{\eta}[\omega] \tag{31}
$$

To solve equations (30), (31), we substitute the expression for $\hat{d}$ (i.e., equation (30)) into the equation for $\hat{c}$ (i.e., equation (31)). This produces 16 terms containing acoustic motion ($\hat{c}$ or $\hat{c}^\dagger$), which we can divide into several categories. First, there are 8 terms involving $\hat{c}^\dagger$. If the acoustic sidebands are far from each other ($|\Delta_\mathrm{u} - \Delta_\ell - 2\omega_{\mathrm{ac}}| \gg \gamma_{\mathrm{ac}}$), these terms are off-resonant for the acoustic mode, and can be ignored. Of the remaining 8 terms, 4 include beating of the sideband of one control beam against the other beam, which would result in expressions like $\hat{c}[\omega \pm (\Delta_\mathrm{u} - \Delta_\ell)]$; since $\Delta_\mathrm{u} - \Delta_\ell \approx 2\omega_{\mathrm{ac}} \gg \gamma_{\mathrm{ac}}$, these terms are also very far off resonance and can be neglected. The last 4 terms produce a combination of the standard dynamic backaction effects of the beams (two terms per beam), and thus should be preserved. With the addition of the vacuum noise term, we obtain the following equation for the acoustic mode:

$$
\left(\frac{\gamma_{\mathrm{ac}}}{2} - i(\omega - \omega_{\mathrm{ac}})\right)\hat{c}[\omega] = (g^{(0)})^2\left(|a_{0,\ell}|^2(\chi_\mathrm{c}[\omega - \Delta_\ell] - \chi_\mathrm{c}[\omega + \Delta_\ell])\right.
$$
$$
\left. +|a_{0,\mathrm{u}}|^2(\chi_\mathrm{c}[\omega - \Delta_\mathrm{u}] - \chi_\mathrm{c}[\omega + \Delta_\mathrm{u}])\right)\hat{c}[\omega]
$$
$$
-ig^{(0)}\left(a_{0,\ell}^*\hat{d}_\xi[\omega + \Delta_\ell] + a_{0,\ell}\hat{d}_\xi^\dagger[\omega - \Delta_\ell]\right.
$$
$$
\left. +a_{0,\mathrm{u}}^*\hat{d}_\xi[\omega + \Delta_\mathrm{u}] + a_{0,\mathrm{u}}\hat{d}_\xi^\dagger[\omega - \Delta_\mathrm{u}]\right)
$$
$$
+\sqrt{\gamma_{\mathrm{ac}}}\hat{\eta}[\omega] \tag{32}
$$

Here $\chi_\mathrm{c}[\omega] = (\kappa/2 - i\omega)^{-1}$ is the cavity susceptibility, and $\hat{d}_\xi[\omega] = \chi_\mathrm{c}[\omega]\sqrt{\kappa}\hat{\xi}[\omega]$ are the vacuum fluctuations of the intracavity field. Now we can rewrite the acoustic equation of motion as

$$
\hat{c}[\omega] = \chi_{\mathrm{ac,eff}}[\omega]\left(-i\hat{F}_{\mathrm{RPSN}}[\omega] + \sqrt{\gamma_{\mathrm{ac}}}\hat{\eta}[\omega]\right), \tag{33}
$$

where the modified acoustic mode susceptibility is

$$
\chi_{\mathrm{ac,eff}}[\omega] = (\gamma_{\mathrm{ac}}/2 - i(\omega - \omega_{\mathrm{ac}}) + i\Sigma[\omega])^{-1} \approx (\gamma_{\mathrm{ac,eff}}/2 - i(\omega - \omega_{\mathrm{ac,eff}}))^{-1}, \tag{34}
$$

with the acoustic linewidth and the acoustic frequency modified by the dynamic backaction:

$$
\gamma_{\mathrm{ac,eff}} = \gamma_{\mathrm{ac}} - 2\mathrm{Im}\Sigma[\omega_{\mathrm{ac,eff}}] = \gamma_{\mathrm{ac}} + \gamma_{\mathrm{ac,opt}} \tag{35}
$$
$$
\omega_{\mathrm{ac,eff}} = \omega_{\mathrm{ac}} + \mathrm{Re}\Sigma[\omega_{\mathrm{ac,eff}}] = \omega_{\mathrm{ac}} + \omega_{\mathrm{ac,opt}} \tag{36}
$$

The self-energy $\Sigma[\omega]$ for the acoustic system is defined as

$$
\Sigma[\omega] = i(g^{(0)})^2\left(|a_{0,\ell}|^2(\chi_\mathrm{c}[\omega - \Delta_\ell] - \chi_\mathrm{c}[\omega + \Delta_\ell]) + |a_{0,\mathrm{u}}|^2(\chi_\mathrm{c}[\omega - \Delta_\mathrm{u}] - \chi_\mathrm{c}[\omega + \Delta_\mathrm{u}])\right), \tag{37}
$$

and the radiation pressure force is defined as

$$
\hat{F}_{\mathrm{RPSN}}[\omega] = g^{(0)}\left(a_{0,\ell}^*\hat{d}_\xi[\omega + \Delta_\ell] + a_{0,\ell}\hat{d}_\xi^\dagger[\omega - \Delta_\ell] + a_{0,\mathrm{u}}^*\hat{d}_\xi[\omega + \Delta_\mathrm{u}] + a_{0,\mathrm{u}}\hat{d}_\xi^\dagger[\omega - \Delta_\mathrm{u}]\right) \tag{38}
$$

Note that this force is Hermitian: $\hat{F}_{\mathrm{RPSN}}^\dagger[\omega] = \hat{F}_{\mathrm{RPSN}}[\omega]$.

Now we are ready to find an expression for the intracavity field. Because we focus on the part of the spectrum close to the optical resonance $\omega \approx 0$, we can neglect the other two sidebands: the red sideband of the lower control beam,

14

which corresponds to $\hat{c}^\dagger[\omega - \Delta_\ell] \approx \hat{c}^\dagger[+\omega_{\mathrm{ac}}] \approx 0$, and the blue sideband of the upper control beam, corresponding to $\hat{c}[\omega - \Delta_{\mathrm{u}}] \approx \hat{c}[-\omega_{\mathrm{ac}}] \approx 0$. The optical field thus becomes

$$\hat{d}[\omega] \approx \chi_{\mathrm{c}}[\omega]\left(-ig^{(0)}\left(a_{0,\ell}\hat{c}[\omega - \Delta_\ell] + a_{0,\mathrm{u}}\hat{c}^\dagger[\omega - \Delta_{\mathrm{u}}]\right) + \sqrt{\kappa}\hat{\xi}\right) \tag{39}$$

Finally, the outgoing field can be calculated using the input-output relations:

$$
\begin{aligned}
\hat{d}_{\mathrm{out}} &= \hat{\xi}_{\mathrm{ext}} - \sqrt{\kappa_{\mathrm{ext}}}\hat{d} \\
&= \hat{\xi}_{\mathrm{ext}} - \sqrt{\kappa_{\mathrm{ext}}}\chi_{\mathrm{c}}[\omega]\left(-ig^{(0)}\left(a_{0,\ell}\hat{c}[\omega - \Delta_\ell] + a_{0,\mathrm{u}}\hat{c}^\dagger[\omega - \Delta_{\mathrm{u}}]\right) + \sqrt{\kappa}\hat{\xi}\right)
\end{aligned} \tag{40}
$$

The acoustic mode annihilation operator spectrum has peaks at $+\omega_{\mathrm{ac,eff}}$, while the creation operator (being its Hermitian conjugate) is peaked at $-\omega_{\mathrm{ac,eff}}$. This means that the red sideband in the expression above (which comes from the $\hat{c}^\dagger$ term) is located around $\omega_{\mathrm{r}} = \Delta_{\mathrm{u}} - \omega_{\mathrm{ac,eff}}$, and the blue sideband (coming from the $\hat{c}$ term) is located around $\omega_{\mathrm{b}} = \Delta_\ell + \omega_{\mathrm{ac,eff}}$. Because of the earlier choice $\Delta_\ell \approx -\omega_{\mathrm{ac}}$, $\Delta_{\mathrm{u}} \approx +\omega_{\mathrm{ac}}$, both of these frequencies are close to zero.

3.2 Detection modes

It this section we describe how the acoustic sidebands are manifest in the photocurrent, and in the next section we use these results to calculate their power spectral densities and cross-correlations between them.

We consider heterodyne detection with a local oscillator (LO) at frequency $-\omega_{\mathrm{LO}}$ with $\omega_{\mathrm{LO}} > 0$ (the case where the local oscillator's frequency is higher than the sidebands frequency is less convenient, since it leads to the photocurrent spectrum being flipped compared to the optical one). Ignoring the reflected control beams, the field incident on the photodiode after combining with the LO is $\hat{a}_{\mathrm{det}} = a_{\mathrm{LO}}e^{+i\omega_{\mathrm{LO}}t} + \hat{d}_{\mathrm{out}}$. Standard photodetection theory [43] states that the (time-dependent) autocorrelation of the photocurrent $i(t)$ can be described as

$$
\begin{aligned}
C_{ii}(t, \tau) &\equiv \langle i(t + \tau/2)i(t - \tau/2)\rangle \\
&= G^2\left\langle : \hat{a}_{\mathrm{det}}^\dagger(t + \tau/2)\hat{a}_{\mathrm{det}}(t + \tau/2)\hat{a}_{\mathrm{det}}^\dagger(t - \tau/2)\hat{a}_{\mathrm{det}}(t - \tau/2) : \right\rangle \\
&\quad + G^2\left\langle \hat{a}_{\mathrm{det}}^\dagger(t)\hat{a}_{\mathrm{det}}(t) \right\rangle \delta(\tau),
\end{aligned} \tag{41}
$$

where G is the photodetector gain and $::$ denotes normal and time ordering. Note that since $i(t)$ is a photocurrent, we take it to be classical and real, so $C_{ii}(\tau)$ is real and symmetric in τ.

If we substitute the expression for $\hat{a}_{\mathrm{det}}$ above and expand up to second order in $\hat{d}$ (keeping in mind that the first order terms average to zero), we get

$$
\begin{aligned}
C_{ii}(t, \tau) \approx\ & G^2|a_{\mathrm{LO}}|^4 + G^2|a_{\mathrm{LO}}|^2\left(\left\langle \hat{d}_{\mathrm{out}}^\dagger(t + \tau/2)\hat{d}_{\mathrm{out}}(t + \tau/2)\right\rangle + \left\langle \hat{d}_{\mathrm{out}}^\dagger(t - \tau/2)\hat{d}_{\mathrm{out}}(t - \tau/2)\right\rangle\right) \\
&+ G^2|a_{\mathrm{LO}}|^2\left(e^{i\omega_{\mathrm{LO}}\tau}\left\langle \hat{d}_{\mathrm{out}}^\dagger(t + \tau/2)\hat{d}_{\mathrm{out}}(t - \tau/2)\right\rangle + e^{-i\omega_{\mathrm{LO}}\tau}\left\langle \hat{d}_{\mathrm{out}}^\dagger(t - \tau/2)\hat{d}_{\mathrm{out}}(t + \tau/2)\right\rangle\right) \\
&+ G^2(a_{\mathrm{LO}})^2 e^{2i\omega_{\mathrm{LO}}t}\left\langle : \hat{d}_{\mathrm{out}}^\dagger(t + \tau/2)\hat{d}_{\mathrm{out}}^\dagger(t - \tau/2) : \right\rangle \\
&+ G^2(a_{\mathrm{LO}}^*)^2 e^{-2i\omega_{\mathrm{LO}}t}\left\langle : \hat{d}_{\mathrm{out}}(t + \tau/2)\hat{d}_{\mathrm{out}}(t - \tau/2) : \right\rangle \\
&+ G^2|a_{\mathrm{LO}}|^2\delta(\tau)
\end{aligned} \tag{42}
$$

The first line in equation (42) is the DC component of the correlator, which is not relevant to the acoustic sideband spectrum and can be ignored. The next three lines reflect beating of the outgoing cavity field with the LO. Finally, the last line represents the unavoidable detector shot noise.

First, let us consider the power spectral density (PSD) of the photocurrent, which is the Fourier transform of the correlation function:

$$S_{ii}[\omega] = \int_{-\infty}^{+\infty} \overline{C_{ii}(t,\tau)} e^{i\omega\tau} d\tau, \tag{43}$$

where $\overline{C_{ii}(t,\tau)}$ denotes that the correlator is averaged over the central time t. We assume that the correlators of the input field are stationary (or at least don't have components at $2\omega_{\mathrm{LO}}$), and that the integration time is long enough that we can set $\overline{e^{2i\omega_{\mathrm{LO}}t}} = 0$. In this case, only the second and the last line in the correlator contribute to the PSD above, which can be re-expressed as

$$S_{ii}[\omega] = G^2|a_{\mathrm{LO}}|^2 \left(S_{\hat{d}^\dagger\hat{d}}[\omega_{\mathrm{LO}} + \omega] + S_{\hat{d}^\dagger\hat{d}}[\omega_{\mathrm{LO}} - \omega] + 1 \right) \tag{44}$$

With the Fourier transform definition (24), the spectrum of the outgoing field can be calculated in a straightforward way using the Wiener-Khinchin theorem:

$$S_{\hat{d}^\dagger\hat{d}}[\omega] = \int_{-\infty}^{+\infty} \overline{\left\langle \hat{d}_{\mathrm{out}}^\dagger(t+\tau/2)\hat{d}_{\mathrm{out}}(t-\tau/2) \right\rangle} e^{i\omega\tau} d\tau = \left\langle \hat{d}_{\mathrm{out}}^\dagger[\omega]\hat{d}_{\mathrm{out}}[-\omega] \right\rangle \tag{45}$$

Now, let us consider what would be the photocurrent $i(t)$ and its corresponding Fourier transform (in the sense of equation (24)) $i[\omega]$. After mixing with the optical local oscillator, the two acoustic sidebands of interest will be located around $\omega_{\mathrm{LO}} + \omega_{\mathrm{r,b}}$. We can define the shifted "local" Fourier transforms

$$i_{\mathrm{r,b}}[\delta\omega] \equiv i[\omega_{\mathrm{LO}} + \omega_{\mathrm{r,b}} + \delta\omega] \tag{46}$$

(note that unlike $i[\omega]$ these don't correspond to any real function of time, so in general $i_{\mathrm{r}}[\omega] \neq (i_{\mathrm{r}}[-\omega])^*$). The PSDs of the sidebands are then described by

$$\begin{aligned}
S_{ii}^{(\mathrm{rr})}[\delta\omega] &\equiv \langle i_{\mathrm{r}}[\delta\omega](i_{\mathrm{r}}[\delta\omega])^* \rangle = S_{ii}[\omega_{\mathrm{LO}} + \omega_{\mathrm{r}} + \delta\omega] \\
&= G^2|a_{\mathrm{LO}}|^2(S_{\hat{d}^\dagger\hat{d}}[2\omega_{\mathrm{LO}} + \omega_{\mathrm{r}} + \delta\omega] + S_{\hat{d}^\dagger\hat{d}}[-\omega_{\mathrm{r}} - \delta\omega] + 1)
\end{aligned} \tag{47}$$

$$\begin{aligned}
S_{ii}^{(\mathrm{bb})}[\delta\omega] &\equiv \langle i_{\mathrm{b}}[\delta\omega](i_{\mathrm{b}}[\delta\omega])^* \rangle = S_{ii}[\omega_{\mathrm{LO}} + \omega_{\mathrm{b}} + \delta\omega] \\
&= G^2|a_{\mathrm{LO}}|^2(S_{\hat{d}^\dagger\hat{d}}[2\omega_{\mathrm{LO}} + \omega_{\mathrm{b}} + \delta\omega] + S_{\hat{d}^\dagger\hat{d}}[-\omega_{\mathrm{b}} - \delta\omega] + 1)
\end{aligned} \tag{48}$$

Here $S_{ii}^{(\mathrm{rr})}[\delta\omega]$ and $S_{ii}^{(\mathrm{bb})}[\delta\omega]$ are the PSDs of the red and the blue sideband respectively, and $\delta\omega$ is the frequency shift in the PSD from the sideband maximum.

While the second terms in the parentheses $S_{\hat{d}^\dagger\hat{d}}[-\omega_{\mathrm{r,b}} - \delta\omega]$ correspond to the optical spectrum close to the cavity resonance, the first terms probe the spectrum roughly $2\omega_{\mathrm{LO}}$ away from the cavity resonance, and therefore are insensitive to the cavity dynamics (more rigorously, the cavity susceptibility in the expression (40) is very small). Moreover, because of the normal ordering of the operators in $S_{\hat{d}^\dagger\hat{d}}$ the vacuum noise terms $\hat{\xi}$ don't contribute. Thus, it is clear that $S_{\hat{d}^\dagger\hat{d}}[2\omega_{\mathrm{LO}}] \approx 0$, and the PSDs simplify to

$$S_{ii}^{(\mathrm{rr})}[\delta\omega] \approx G^2|a_{\mathrm{LO}}|^2(S_{\hat{d}^\dagger\hat{d}}[-\omega_{\mathrm{r}} - \delta\omega] + 1) \tag{49}$$

$$S_{ii}^{(\mathrm{bb})}[\delta\omega] \approx G^2|a_{\mathrm{LO}}|^2(S_{\hat{d}^\dagger\hat{d}}[-\omega_{\mathrm{b}} - \delta\omega] + 1) \tag{50}$$

Next, we turn to the correlations between the two sidebands. It is natural to define them as

$$S_{ii}^{(\mathrm{rb})}[\delta\omega] \equiv \langle i_{\mathrm{b}}[\delta\omega]i_{\mathrm{r}}[-\delta\omega] \rangle = \langle i[\omega_{\mathrm{LO}} + \omega_{\mathrm{b}} + \delta\omega]i[\omega_{\mathrm{LO}} + \omega_{\mathrm{r}} - \delta\omega] \rangle \tag{51}$$

Note that i_{r} isn't complex conjugated, because it comes from $\hat{c}^\dagger$ rather than $\hat{c}$. Similar to (43), we can use the definition of the Fourier transform $i[\delta\omega]$ to express the result above through the time correlator $C_{ii}(t,\tau)$:

$$\begin{aligned}
S_{ii}^{(\mathrm{rb})}[\delta\omega] &= \int_{-\infty}^{+\infty} \overline{C_{ii}(t,\tau)e^{i(2\omega_{\mathrm{LO}}+\omega_{\mathrm{r}}+\omega_{\mathrm{b}})t}} e^{i(\omega_{\mathrm{b}}/2 - \omega_{\mathrm{r}}/2 + \delta\omega)\tau} d\tau \\
&= G^2(a_{\mathrm{LO}}^*)^2 \int_{-\infty}^{+\infty} \overline{\left\langle : \left(e^{i\omega_{\mathrm{b}}(t+\tau/2)}\hat{d}_{\mathrm{out}}(t+\tau/2)\right)\left(e^{i\omega_{\mathrm{r}}(t-\tau/2)}\hat{d}_{\mathrm{out}}(t-\tau/2)\right) : \right\rangle} e^{i\delta\omega\tau} d\tau
\end{aligned} \tag{52}$$

16

This expression can be greatly simplified if we recall from input-output theory that the commutation relations of the outgoing fields are the same as the incoming ones. This implies that $\hat{d}_{\text{out}}$ (just like $\hat{\xi}_{\text{ext}}$) commutes at different times, so the time ordering inside the ensemble averaging is irrelevant. Therefore, we can apply the Wiener-Khinchin theorem again and arrive at

$$S_{ii}^{(\text{rb})}[\delta\omega] = G^2(a_{\text{LO}}^*)^2 \left\langle \hat{d}_{\text{out}}[\omega_{\text{b}} + \delta\omega]\hat{d}_{\text{out}}[\omega_{\text{r}} - \delta\omega]\right\rangle \tag{53}$$

3.3 Correlators values and the interpretation

In this section we calculate the sideband PSDs (49), (50) and the cross-correlator (53) for the optical field (40) obtained earlier.

We start with the sideband PSDs $S_{ii}^{(\text{rr})}$ and $S_{ii}^{(\text{bb})}$, which are proportional to $S_{\hat{d}^\dagger\hat{d}}[\omega]$. As noted before, due to the normal ordering the terms containing the vacuum noise $\hat{\xi}$ won't contribute. Thus, we're left with

$$\begin{aligned}
S_{\hat{d}^\dagger\hat{d}}[\omega] &= \left\langle \hat{d}_{\text{out}}^\dagger[\omega]\hat{d}_{\text{out}}[-\omega]\right\rangle \\
&= \kappa_{\text{ext}}|\chi_{\text{c}}[-\omega]|^2(g^{(0)})^2 \left(|a_{0,\ell}|^2 S_{\hat{c}^\dagger\hat{c}}[\omega + \Delta_\ell] + |a_{0,\text{u}}|^2 S_{\hat{c}\hat{c}^\dagger}[\omega + \Delta_\text{u}]\right)
\end{aligned} \tag{54}$$

We've also omitted two other terms involving the acoustic mode motion: $a_{0,\text{u}}^* a_{0,\ell} \left\langle \hat{c}[\omega + \Delta_\text{u}]\hat{c}[-\omega - \Delta_\ell]\right\rangle$ and its complex conjugate $a_{0,\ell}^* a_{0,\text{u}} \left\langle \hat{c}^\dagger[\omega + \Delta_\ell]\hat{c}^\dagger[-\omega - \Delta_\text{u}]\right\rangle$. While not strictly zero, these terms are nevertheless small because the acoustic susceptibilities of the two terms in the product don't overlap. For example, in the first expression the two acoustic terms are centered around $\omega = \omega_{\text{ac}} - \Delta_\text{u} = -\omega_\text{r}$ and $\omega = -\omega_{\text{ac}} - \Delta_\ell = -\omega_\text{b}$; as we're working in the assumption $|\omega_\text{r} - \omega_\text{b}| \gg \gamma_{\text{ac,eff}}$ (non-overlapping sidebands), the product of these two terms is always small.

Now we need to calculate the acoustic motion correlators:

$$S_{\hat{c}^\dagger\hat{c}}[\omega] = |\chi_{\text{ac,eff}}[-\omega]|^2 (S_{\hat{F}\hat{F}}^{\text{RPSN}}[\omega] + S_{\hat{F}^\dagger\hat{F}}^{\text{th}}[\omega]) \tag{55}$$

$$S_{\hat{c}\hat{c}^\dagger}[\omega] = |\chi_{\text{ac,eff}}[+\omega]|^2 (S_{\hat{F}\hat{F}}^{\text{RPSN}}[\omega] + S_{\hat{F}\hat{F}^\dagger}^{\text{th}}[\omega]) \tag{56}$$

The PSD of the thermal force is:

$$S_{\hat{F}^\dagger\hat{F}}^{\text{th}}[\omega] \equiv \left\langle (\sqrt{\gamma_{\text{ac}}}\hat{\eta}^\dagger[\omega])(\sqrt{\gamma_{\text{ac}}}\hat{\eta}[-\omega])\right\rangle = \gamma_{\text{ac}}n_{\text{th}} \tag{57}$$

$$S_{\hat{F}\hat{F}^\dagger}^{\text{th}}[\omega] \equiv \left\langle (\sqrt{\gamma_{\text{ac}}}\hat{\eta}[\omega])(\sqrt{\gamma_{\text{ac}}}\hat{\eta}^\dagger[-\omega])\right\rangle = \gamma_{\text{ac}}(n_{\text{th}} + 1), \tag{58}$$

and the PSD of the radiation pressure is

$$\begin{aligned}
S_{\hat{F}\hat{F}}^{\text{RPSN}}[\omega] &\equiv \left\langle \hat{F}_{\text{RPSN}}[\omega]\hat{F}_{\text{RPSN}}[-\omega]\right\rangle \\
&= (g^{(0)})^2\kappa \left(|a_{0,\ell}|^2|\chi_{\text{c}}[\omega + \Delta_\ell]|^2 + |a_{0,\text{u}}|^2|\chi_{\text{c}}[\omega + \Delta_\text{u}]|^2\right)
\end{aligned} \tag{59}$$

(since $\hat{F}_{\text{RPSN}}$ is Hermitian, this is the only correlator that we need).

For the following discussion we note that

$$\begin{aligned}
S_{\hat{F}\hat{F}^\dagger}^{\text{th}}[\omega] - S_{\hat{F}^\dagger\hat{F}}^{\text{th}}[-\omega] &= \gamma_{\text{ac}} \tag{60} \\
S_{\hat{F}\hat{F}}^{\text{RPSN}}[\omega] - S_{\hat{F}\hat{F}}^{\text{RPSN}}[-\omega] &= (g^{(0)})^2\kappa \left(|a_{0,\ell}|^2(|\chi_{\text{c}}[\omega + \Delta_\ell]|^2 - |\chi_{\text{c}}[-\omega + \Delta_\ell]|^2)\right. \\
&\qquad \left. + |a_{0,\text{u}}|^2(|\chi_{\text{c}}[\omega + \Delta_\text{u}]|^2 - |\chi_{\text{c}}[-\omega + \Delta_\text{u}]|^2)\right) \\
&= -2\text{Im}\Sigma[\omega] \equiv \gamma_{\text{ac,opt}} \tag{61}
\end{aligned}$$

This shows that the antisymmetric part of the force noise spectrum (with appropriate ordering for a non-Hermitian noise operator) is equal to the dissipation rate associated with this force: either the intrinsic loss γ_{ac} for the environment acoustic

mode noise $\hat{\eta}$, or the optomechanically induced damping $\gamma_{\text{ac,opt}}$ for the radiation pressure shot noise. This is well-known from quantum noise theory [44], where the positive and the negative parts of the force spectrum are associated with the tendency to (respectively) extract energy from or give energy to the system, so the difference between the two provides the net damping.

When substituting force spectra into the equations for $S_{\hat{c}^\dagger \hat{c}}$ and $S_{\hat{c}\hat{c}^\dagger}$, we can simplify them by assuming that $\gamma_{\text{ac,eff}} \ll \kappa$, so the radiation pressure noise spectrum is approximately flat over the acoustic resonance. This lets us write

$$
\begin{aligned}
S_{\hat{c}^\dagger \hat{c}}[\omega] &\approx |\chi_{\text{ac,eff}}[-\omega]|^2 (S_{\hat{F}\hat{F}}^{\text{RPSN}}[-\omega_{\text{ac,eff}}] + S_{\hat{F}^\dagger \hat{F}}^{\text{th}}[-\omega_{\text{ac,eff}}]) \\
&= |\chi_{\text{ac,eff}}[-\omega]|^2 (n_{\text{RPSN}}\gamma_{\text{ac,opt}} + n_{\text{th}}\gamma_{\text{ac}}) \\
S_{\hat{c}\hat{c}^\dagger}[\omega] &\approx |\chi_{\text{ac,eff}}[\omega]|^2 (S_{\hat{F}\hat{F}}^{\text{RPSN}}[\omega_{\text{ac,eff}}] + S_{\hat{F}\hat{F}^\dagger}^{\text{th}}[\omega_{\text{ac,eff}}]) \\
&= |\chi_{\text{ac,eff}}[\omega]|^2 ((n_{\text{RPSN}} + 1)\gamma_{\text{ac,opt}} + (n_{\text{th}} + 1)\gamma_{\text{ac}}),
\end{aligned}
$$

(62)

(63)

where we've defined the effective phonon occupation of the RPSN bath $n_{\text{RPSN}} = S_{\hat{F}\hat{F}}^{\text{RPSN}}[-\omega_{\text{ac,eff}}]/\gamma_{\text{ac,opt}}$ analogously to the thermal bath occupation n_{th}. To determine the final mean energy of the acoustic mode, we can find the expectation value of the phonon number operator by integrating its PSD:

$$
\begin{aligned}
n_{\text{ac}} &= \left\langle \hat{c}^\dagger(t)\hat{c}(t) \right\rangle = \frac{1}{2\pi} \int_{-\infty}^{+\infty} S_{\hat{c}^\dagger \hat{c}}[\omega] d\omega \\
&= \frac{1}{2\pi} \int_{-\infty}^{+\infty} \frac{n_{\text{RPSN}}\gamma_{\text{ac,opt}} + n_{\text{th}}\gamma_{\text{ac}}}{\gamma_{\text{ac,eff}}^2/4 + (\omega + \omega_{\text{ac,eff}})^2} d\omega = \frac{n_{\text{RPSN}}\gamma_{\text{ac,opt}} + n_{\text{th}}\gamma_{\text{ac}}}{\gamma_{\text{ac,eff}}}
\end{aligned}
$$

(64)

This expression can be understood intuitively if we consider that the acoustic oscillator is coupled to two different baths (environment and radiation pressure force) with two different rates (γ_{ac} and $\gamma_{\text{ac,opt}}$ respectively). This way, the final occupation of the oscillator is a weighted average of the occupations of the two baths, with the weights being proportional to the coupling rates.

With this expression for n_{ac} the PSDs simplify to

$$
S_{\hat{c}^\dagger \hat{c}}[\omega] = \frac{n_{\text{ac}}\gamma_{\text{ac,eff}}}{\gamma_{\text{ac,eff}}^2/4 + (\omega + \omega_{\text{ac,eff}})^2}
$$

(65)

$$
S_{\hat{c}\hat{c}^\dagger}[\omega] = \frac{(n_{\text{ac}} + 1)\gamma_{\text{ac,eff}}}{\gamma_{\text{ac,eff}}^2/4 + (\omega - \omega_{\text{ac,eff}})^2}
$$

(66)

Note that the difference in the magnitude between the two PSDs (which comes from the asymmetry of the force noise spectra) is directly related to the equal-time commutator of the acoustic mode creation and annihilation operators:

$$
[\hat{c}(t), \hat{c}^\dagger(t)] = \left\langle [\hat{c}(t), \hat{c}^\dagger(t)] \right\rangle = \left\langle \hat{c}(t)\hat{c}^\dagger(t) \right\rangle - \left\langle \hat{c}^\dagger(t)\hat{c}(t) \right\rangle = (n_{\text{ac}} + 1) - n_{\text{ac}} = 1
$$

(67)

With these spectra the PSD of the outgoing field is

$$
\begin{aligned}
S_{\hat{d}^\dagger \hat{d}}[\omega] &= \left\langle \hat{d}_{\text{out}}^\dagger[\omega]\hat{d}_{\text{out}}[-\omega] \right\rangle \\
&= \kappa_{\text{ext}} |\chi_c[-\omega]|^2 (g^{(0)})^2 \left(|a_{0,\ell}|^2 \frac{n_{\text{ac}}\gamma_{\text{ac,eff}}}{\gamma_{\text{ac,eff}}^2/4 + (\omega + \Delta_\ell + \omega_{\text{ac,eff}})^2} \right. \\
&\quad \left. + |a_{0,\text{u}}|^2 \frac{(n_{\text{ac}} + 1)\gamma_{\text{ac,eff}}}{\gamma_{\text{ac,eff}}^2/4 + (\omega + \Delta_\text{u} - \omega_{\text{ac,eff}})^2} \right) \\
&= \kappa_{\text{ext}} |\chi_c[-\omega]|^2 (g^{(0)})^2 \left(|a_{0,\ell}|^2 \frac{n_{\text{ac}}\gamma_{\text{ac,eff}}}{\gamma_{\text{ac,eff}}^2/4 + (\omega + \omega_\text{b})^2} + |a_{0,\text{u}}|^2 \frac{(n_{\text{ac}} + 1)\gamma_{\text{ac,eff}}}{\gamma_{\text{ac,eff}}^2/4 + (\omega + \omega_\text{r})^2} \right)
\end{aligned}
$$

(68)

(69)

18

As expected, it is comprised of two Lorentzians centered at $\omega = -\omega_{\rm r}$ and $\omega = -\omega_{\rm b}$. From (49), (50) the photocurrent PSDs of the individual sidebands are

$$S_{ii}^{(\rm rr)}[\delta\omega] \approx G^2|a_{\rm LO}|^2 \left(\kappa_{\rm ext}|\chi_{\rm c}[\omega_{\rm r}]|^2 (g^{(0)})^2|a_{0,{\rm u}}|^2 \frac{(n_{\rm ac}+1)\gamma_{\rm ac,eff}}{\gamma_{\rm ac,eff}^2/4 + \delta\omega^2} + 1 \right) \tag{70}$$

$$S_{ii}^{(\rm bb)}[\delta\omega] \approx G^2|a_{\rm LO}|^2 \left(\kappa_{\rm ext}|\chi_{\rm c}[\omega_{\rm b}]|^2 (g^{(0)})^2|a_{0,\ell}|^2 \frac{n_{\rm ac}\gamma_{\rm ac,eff}}{\gamma_{\rm ac,eff}^2/4 + \delta\omega^2} + 1 \right) \tag{71}$$

Both are Lorentzians with shot noise background, and with area under the Lorentzian proportional to $n_{\rm ac}$ or $n_{\rm ac}+1$ for the blue and the red sideband respectively.

Now we switch to the cross-correlator (53), which is proportional to $\left\langle \hat{d}_{\rm out}[\omega_{\rm b}+\delta\omega]\hat{d}_{\rm out}[\omega_{\rm r}-\delta\omega] \right\rangle$. Because the normal ordering is not enforced, there are terms involving the vacuum noise:

$$
\begin{aligned}
\left\langle \hat{d}_{\rm out}[\omega_{\rm b}+\delta\omega]\hat{d}_{\rm out}[\omega_{\rm r}-\delta\omega] \right\rangle &\approx -\kappa_{\rm ext}(\chi_{\rm c}[\omega_{\rm r}]\chi_{\rm c}[\omega_{\rm b}])(g^{(0)})^2 a_{0,\ell}a_{0,{\rm u}}S_{\hat{c}\hat{c}^\dagger}[\omega_{\rm ac,eff}+\delta\omega] \\
&\quad + i\left\langle \left(\hat{\xi}_{\rm ext}[\omega_{\rm b}+\delta\omega] - \sqrt{\kappa_{\rm ext}\kappa}\chi_{\rm c}[\omega_{\rm b}]\hat{\xi}[\omega_{\rm b}+\delta\omega] \right) \right. \\
&\quad \left. \times \left(\sqrt{\kappa_{\rm ext}}\chi_{\rm c}[\omega_{\rm r}]g^{(0)} \left(a_{0,{\rm u}}\hat{c}^\dagger[-\omega_{\rm ac,eff}-\delta\omega] \right) \right) \right\rangle
\end{aligned}
\tag{72}
$$

The first term is just the acoustic motion PSD, similar to the sidebands' PSDs (as before, we've assumed $\delta\omega \sim \gamma_{\rm ac,eff} \ll |\omega_{\rm r}-\omega_{\rm b}|$ and neglected all off-resonant acoustic terms). The second term involves the correlations of the optical vacuum fluctuations with the acoustic mode motion, which are non-zero because the acoustic oscillator is driven by the radiation pressure shot noise arising from these vacuum fluctuations. Thus, this term directly represents the action of the radiation pressure shot noise on the acoustic oscillator.

Using expression (22) for $\hat{\xi}$ and (38) for $\hat{F}_{\rm RPSN}$, we get

$$
\begin{aligned}
\left\langle \hat{\xi}[\omega_{\rm b}+\delta\omega]\hat{F}_{\rm RPSN}[-\omega_{\rm ac,eff}-\delta\omega] \right\rangle &= g^{(0)}a_{0,\ell}\left\langle \hat{\xi}[\omega_{\rm b}+\delta\omega]\hat{d}_{\hat{\xi}}^\dagger[-\omega_{\rm b}-\delta\omega] \right\rangle \\
&= g^{(0)}a_{0,\ell}\chi_{\rm c}[-\omega_{\rm b}]\sqrt{\kappa} \tag{73} \\
\left\langle \hat{\xi}_{\rm ext}[\omega_{\rm b}+\delta\omega]\hat{F}_{\rm RPSN}[-\omega_{\rm ac,eff}-\delta\omega] \right\rangle &= \sqrt{\kappa_{\rm ext}/\kappa}\left\langle \hat{\xi}[\omega_{\rm b}+\delta\omega]\hat{F}_{\rm RPSN}[-\omega_{\rm ac,eff}-\delta\omega] \right\rangle \\
&= g^{(0)}a_{0,\ell}\chi_{\rm c}[-\omega_{\rm b}]\sqrt{\kappa_{\rm ext}}, \tag{74}
\end{aligned}
$$

so that

$$
\begin{aligned}
&\left\langle \left(\hat{\xi}_{\rm ext}[\omega_{\rm b}+\delta\omega] - \sqrt{\kappa_{\rm ext}\kappa}\chi_{\rm c}[\omega_{\rm b}]\hat{\xi}[\omega_{\rm b}+\delta\omega] \right) \hat{c}^\dagger[-\omega_{\rm ac,eff}-\delta\omega] \right\rangle \\
&= i(\chi_{\rm ac,eff}[\omega_{\rm ac,eff}+\delta\omega])^* \left\langle \left(\hat{\xi}_{\rm ext}[\omega_{\rm b}+\delta\omega] - \sqrt{\kappa_{\rm ext}\kappa}\chi_{\rm c}[\omega_{\rm b}]\hat{\xi}[\omega_{\rm b}+\delta\omega] \right) \hat{F}_{\rm RPSN}[-\omega_{\rm ac,eff}-\delta\omega] \right\rangle \\
&= i(\chi_{\rm ac,eff}[\omega_{\rm ac,eff}+\delta\omega])^* \sqrt{\kappa_{\rm ext}}(1-\kappa\chi_{\rm c}[\omega_{\rm b}])g^{(0)}a_{0,\ell}\chi_{\rm c}[-\omega_{\rm b}] \\
&= -i(\chi_{\rm ac,eff}[\omega_{\rm ac,eff}+\delta\omega])^* \sqrt{\kappa_{\rm ext}}g^{(0)}a_{0,\ell}\chi_{\rm c}[\omega_{\rm b}] \tag{75}
\end{aligned}
$$

Note that this expression depends on the full complex acoustic susceptibility $\chi_{\rm ac,eff}[\omega]$, unlike, for example, the acoustic PSD, where only $|\chi_{\rm ac,eff}|^2$ is present. This implies that it is sensitive to the phase response of the acoustic oscillator, meaning that this term really is a correlator between the force and the displacement (simple force-force or displacement-displacement correlators wouldn't depend on the force-displacement phase shift).

The complete noise correlator becomes

$$\left\langle \hat{d}_{\rm out}[\omega_{\rm b}+\delta\omega]\hat{d}_{\rm out}[\omega_{\rm r}-\delta\omega] \right\rangle \approx G_{cc}\left(S_{\hat{c}\hat{c}^\dagger}[\omega_{\rm ac,eff}+\delta\omega] - (\chi_{\rm ac,eff}[\omega_{\rm ac,eff}+\delta\omega])^* \right) \tag{76}$$

$$G_{cc} = -\kappa_{\rm ext}(\chi_{\rm c}[\omega_{\rm r}]\chi_{\rm c}[\omega_{\rm b}])(g^{(0)})^2 a_{0,\ell}a_{0,{\rm u}} \tag{77}$$

19

where G_{cc} simply is a conversion factor between the displacement and the outgoing field.

Finally, the photocurrent cross-correlator is

$$
\begin{aligned}
S_{ii}^{(\mathrm{rb})}[\delta\omega] &= G^2(a_{\mathrm{LO}}^*)^2 G_{cc}\left(S_{\hat{c}\hat{c}^\dagger}[\omega_{\mathrm{ac,eff}}+\delta\omega]-(\chi_{\mathrm{ac,eff}}[\omega_{\mathrm{ac,eff}}+\delta\omega])^*\right) \\
&= G^2(a_{\mathrm{LO}}^*)^2 G_{cc}\left(\frac{(n_{\mathrm{ac}}+1)\gamma_{\mathrm{ac,eff}}}{\gamma_{\mathrm{ac,eff}}^2/4+\delta\omega^2}-\frac{\gamma_{\mathrm{ac,eff}}/2-i\delta\omega}{\gamma_{\mathrm{ac,eff}}^2/4+\delta\omega^2}\right) \\
&= G^2(a_{\mathrm{LO}}^*)^2 G_{cc}\frac{(n_{\mathrm{ac}}+1/2)\gamma_{\mathrm{ac,eff}}-i\delta\omega}{\gamma_{\mathrm{ac,eff}}^2/4+\delta\omega^2}
\end{aligned}
\tag{78}
$$

This expression is different from (70) and (71) in several important ways. First, there's no shot noise background present, as this noise is uncorrelated between the two sidebands (it's important to note that the measurement SNR is still affected by the shot noise; it just averages to zero instead of to some finite value). Second, the cross-correlator is complex, with an imaginary part that is antisymmetric in $\delta\omega$. Finally, the real Lorentzian part of the cross-correlator is proportional not to n_{ac} (like in $S_{ii}^{(\mathrm{bb})}$) or $n_{\mathrm{ac}}+1$ (as in $S_{ii}^{(\mathrm{rr})}$), but to $n_{\mathrm{ac}}+1/2$. As was shown above in equation (76), this additional half phonon in the real part together with the anti-Lorentzian imaginary part can be combined to produce a complex acoustic susceptibility. This susceptibility shows up because of the correlation between the random radiation pressure force noise and the acoustic mode displacement driven by this force, and thus is an unambiguous signature of the RPSN acting on the acoustic oscillator.

3.4 Photothermal coupling

In this section we consider the effect of the photothermal optomechanical coupling.

The quantum treatment of the photothermal coupling is similar to [45]. We model it as an additional optical loss and an extra acoustic force whose magnitude is proportional to the optical power lost to that channel. To describe this quantitatively, we first introduce an optical loss channel with a rate κ_{pt} and a corresponding vacuum noise $\hat{\xi}_{\mathrm{pt}}$. This modifies the original equation of motion for the optical mode (6) to

$$
\dot{\hat{a}} = -\frac{\kappa}{2}\hat{a}-ig^{(0)}(\hat{c}^\dagger+\hat{c})\hat{a}+\sqrt{\kappa_{\mathrm{int}}}\hat{\xi}_{\mathrm{int}}+\sqrt{\kappa_{\mathrm{pt}}}\hat{\xi}_{\mathrm{pt}}+\sqrt{\kappa_{\mathrm{ext}}}(a_{\mathrm{ext}}+\hat{\xi}_{\mathrm{ext}})
\tag{79}
$$

The total damping is now a combination of all three loss rates: $\kappa = \kappa_{\mathrm{int}}+\kappa_{\mathrm{pt}}+\kappa_{\mathrm{ext}}$. The vacuum noise $\hat{\xi}_{\mathrm{pt}}$ is uncorrelated with any other noise and is described by the same correlation relations (8-10). The amplitude of the field lost to that channel can be found from the input-output relations, just like (40) for the external coupling:

$$
\hat{a}_{\mathrm{out,pt}} = \hat{\xi}_{\mathrm{pt}}-\sqrt{\kappa_{\mathrm{pt}}}\hat{a}
\tag{80}
$$

The corresponding power is simply

$$
\hat{I}_{\mathrm{out,pt}} = \hat{a}_{\mathrm{out,pt}}^\dagger \hat{a}_{\mathrm{out,pt}}
\tag{81}
$$

The photothermal force is proportional to this intensity. However, the thermal reaction rate may be slow compared to the characteristic frequencies of interest (i.e., $\omega_{\mathrm{ac,eff}}$), so the force may be subject to a low-pass filtering. We can model this by writing

$$
\tau_{\mathrm{pt}}\dot{\hat{F}}_{\mathrm{pt}} = -\hat{F}_{\mathrm{pt}}+A_{\mathrm{pt}}\hat{I}_{\mathrm{out,pt}},
\tag{82}
$$

where A_{pt} is the DC proportionality coefficient between the intensity and the photothermal force, and τ_{pt} is the time constant of the low-pass filter. The solution of this equation (in the Fourier domain) is

$$
\hat{F}_{\mathrm{pt}}[\omega] = \frac{A_{\mathrm{pt}}\hat{I}_{\mathrm{out,pt}}[\omega]}{1-i\omega\tau_{\mathrm{pt}}}
\tag{83}
$$

20

Since we're only interested in the forces in a small frequency band around $\omega_{ac,eff}$, we can substitute $\omega \approx \omega_{ac,eff}$ in the denominator of the expression above and transform back to the time domain, getting

$$\hat{F}_{pt}(t) = \frac{A_{pt}}{1 - i\omega_{ac,eff}\tau_{pt}} \hat{I}_{out,pt}(t) = A_{pt,eff}\hat{I}_{out,pt}(t) \tag{84}$$

Note that this equation only holds for spectral components of the photothermal force near $\omega_{ac,eff}$.

With that result, we can modify the acoustic equation of motion (7) and turn it into

$$\dot{\hat{c}} = -\left(\frac{\gamma_{ac}}{2} + i\omega_{ac}\right)\hat{c} - ig^{(0)}\hat{a}^\dagger\hat{a} - i\hat{F}_{pt} + \sqrt{\gamma_{ac}}\hat{\eta} \tag{85}$$

Next, we once again perform the first order expansion of the optical mode $\hat{a} = a_0 + \hat{d}$. This leads to the photothermal force

$$
\begin{aligned}
\hat{F}_{pt}(t) &= A_{pt,eff}\hat{a}^\dagger_{out,pt}\hat{a}_{out,pt} \\
&= A_{pt,eff}\left(\hat{\xi}^\dagger_{pt} - \sqrt{\kappa_{pt}}(a_0^* + \hat{d}^\dagger)\right)\left(\hat{\xi}_{pt} - \sqrt{\kappa_{pt}}(a_0 + \hat{d})\right) \\
&\approx A_{pt,eff}\kappa_{pt}|a_0|^2 + A_{pt,eff}\kappa_{pt}(a_0^*\hat{d} + \hat{d}^\dagger a_0) - A_{pt,eff}\sqrt{\kappa_{pt}}(a_0^*\hat{\xi}_{pt} + \hat{\xi}^\dagger_{pt}a_0) \\
&= g^{(0)}_{pt}|a_0|^2 + g^{(0)}_{pt}(a_0^*\hat{d} + \hat{d}^\dagger a_0) - \frac{g^{(0)}_{pt}}{\sqrt{\kappa_{pt}}}(a_0^*\hat{\xi}_{pt} + \hat{\xi}^\dagger_{pt}a_0),
\end{aligned}
\tag{86}
$$

where $g^{(0)}_{pt} = A_{pt,eff}\kappa_{pt}$ is a single-photon photothermal coupling rate. It is analogous to $g^{(0)}$, but it is in general complex (owing to the low-pass filtering) and appears only in the acoustic equation of motion, since its origin is non-unitary. In the following we ignore the static force term $g^{(0)}_{pt}|a_0|^2$ (this term is incorrect anyway, since we've used the low-passed proportionality coefficient $A_{pt,eff}$ instead of the static A_{pt}), just as for the radiation pressure. The acoustic equation of motion then becomes

$$\dot{\hat{c}} = -\left(\frac{\gamma_{ac}}{2} + i\omega_{ac}\right)\hat{c} - i(g^{(0)} + g^{(0)}_{pt})(a_0^*\hat{d} + \hat{d}^\dagger a_0) + i\frac{g^{(0)}_{pt}}{\sqrt{\kappa_{pt}}}(a_0^*\hat{\xi}_{pt} + \hat{\xi}^\dagger_{pt}a_0) + \sqrt{\gamma_{ac}}\hat{\eta} \tag{87}$$

The rest follows fairly closely the derivation for case of pure radiation pressure. After transitioning to the Fourier domain and solving for $\hat{c}[\omega]$, we find, similarly to (33)

$$\hat{c}[\omega] = \chi_{ac,eff}[\omega]\left(-i\hat{F}_{opt}[\omega] + \sqrt{\gamma_{ac}}\hat{\eta}[\omega]\right) \tag{88}$$

There are two modifications here. First, the expression for the acoustic susceptibility is still the same $\chi_{ac,eff}[\omega] = (\gamma_{ac}/2 - i(\omega - \omega_{ac}) + i\Sigma[\omega])^{-1}$, but the self-energy is slightly different:

$$\Sigma[\omega] = ig^{(0)}(g^{(0)} + g^{(0)}_{pt})\left(|a_{0,\ell}|^2(\chi_c[\omega - \Delta_\ell] - \chi_c[\omega + \Delta_\ell]) + |a_{0,u}|^2(\chi_c[\omega - \Delta_u] - \chi_c[\omega + \Delta_u])\right) \tag{89}$$

(this expression is proportional to $g^{(0)}(g^{(0)} + g^{(0)}_{pt})$, in contrast with $\left(g^{(0)}\right)^2$ in the radiation pressure case (37)). Second, the radiation pressure force is replaced by a more general optical force:

$$
\begin{aligned}
\hat{F}_{opt}[\omega] &= g^{(0)}\left(a_{0,\ell}^*\hat{d}_\xi[\omega + \Delta_\ell] + a_{0,\ell}\hat{d}^\dagger_\xi[\omega - \Delta_\ell] + a_{0,u}^*\hat{d}_\xi[\omega + \Delta_u] + a_{0,u}\hat{d}^\dagger_\xi[\omega - \Delta_u]\right) \\
&+ g^{(0)}_{pt}\left(a_{0,\ell}^*\hat{d}_{pt}[\omega + \Delta_\ell] + a_{0,\ell}\hat{d}^\dagger_{pt}[\omega - \Delta_\ell] + a_{0,u}^*\hat{d}_{pt}[\omega + \Delta_u] + a_{0,u}\hat{d}^\dagger_{pt}[\omega - \Delta_u]\right),
\end{aligned}
\tag{90}
$$

where the RPSN is associated with the same vacuum noise as before $\hat{d}_\xi[\omega] = \chi_c[\omega]\sqrt{\kappa}\hat{\xi}[\omega]$, while for the photothermal noise it's modified:

$$\hat{d}_{pt}[\omega] = \chi_c[\omega]\sqrt{\kappa}\hat{\xi}[\omega] - \frac{\hat{\xi}_{pt}}{\sqrt{\kappa_{pt}}} \tag{91}$$

21

Since $g_{\mathrm{pt}}^{(0)}$ is in general complex, the optical force is no longer Hermitian: $\hat{F}_{\mathrm{opt}}^{\dagger} \neq \hat{F}_{\mathrm{opt}}$. Therefore, we need to calculate two different force noise spectra:

$$
\begin{aligned}
S_{\hat{F}\hat{F}^{\dagger}}^{\mathrm{opt}}[\omega] &\equiv \left\langle \hat{F}_{\mathrm{opt}}[\omega]\hat{F}_{\mathrm{opt}}^{\dagger}[-\omega]\right\rangle \\
&= |g^{(0)} + g_{\mathrm{pt}}^{(0)}|^2 \kappa \left(|a_{0,\ell}|^2 |\chi_{\mathrm{c}}[\omega+\Delta_\ell]|^2 + |a_{0,\mathrm{u}}|^2 |\chi_{\mathrm{c}}[\omega+\Delta_{\mathrm{u}}]|^2\right) \\
&\quad -2\mathrm{Re}\left[(g^{(0)}+g_{\mathrm{pt}}^{(0)})^* g_{\mathrm{pt}}^{(0)}\left(|a_{0,\ell}|^2 \chi_{\mathrm{c}}[-\omega-\Delta_\ell]) + |a_{0,\mathrm{u}}|^2 \chi_{\mathrm{c}}[-\omega-\Delta_{\mathrm{u}}])\right] \\
&\quad +\frac{|g_{\mathrm{pt}}^{(0)}|^2}{\kappa_{\mathrm{pt}}}\left(|a_{0,\ell}|^2 + |a_{0,\mathrm{u}}|^2\right) \\
&= (g^{(0)})^2 \kappa \left(|a_{0,\ell}|^2 |\chi_{\mathrm{c}}[\omega+\Delta_\ell]|^2 + |a_{0,\mathrm{u}}|^2 |\chi_{\mathrm{c}}[\omega+\Delta_{\mathrm{u}}]|^2\right) \\
&\quad +2\mathrm{Re}\left[g^{(0)} g_{\mathrm{pt}}^{(0)}\left(|a_{0,\ell}|^2 \chi_{\mathrm{c}}[\omega+\Delta_\ell] + |a_{0,\mathrm{u}}|^2 \chi_{\mathrm{c}}[\omega+\Delta_{\mathrm{u}}]\right)\right] \\
&\quad +\frac{|g_{\mathrm{pt}}^{(0)}|^2}{\kappa_{\mathrm{pt}}}\left(|a_{0,\ell}|^2 + |a_{0,\mathrm{u}}|^2\right) \tag{92}
\end{aligned}
$$

$$
\begin{aligned}
S_{\hat{F}^{\dagger}\hat{F}}^{\mathrm{opt}}[\omega] &\equiv \left\langle \hat{F}_{\mathrm{opt}}^{\dagger}[\omega]\hat{F}_{\mathrm{opt}}[-\omega]\right\rangle \\
&= (g^{(0)})^2 \kappa \left(|a_{0,\ell}|^2 |\chi_{\mathrm{c}}[\omega+\Delta_\ell]|^2 + |a_{0,\mathrm{u}}|^2 |\chi_{\mathrm{c}}[\omega+\Delta_{\mathrm{u}}]|^2\right) \\
&\quad +2\mathrm{Re}\left[g^{(0)} g_{\mathrm{pt}}^{(0)}\left(|a_{0,\ell}|^2 \chi_{\mathrm{c}}[-\omega-\Delta_\ell] + |a_{0,\mathrm{u}}|^2 \chi_{\mathrm{c}}[-\omega-\Delta_{\mathrm{u}}]\right)\right] \\
&\quad +\frac{|g_{\mathrm{pt}}^{(0)}|^2}{\kappa_{\mathrm{pt}}}\left(|a_{0,\ell}|^2 + |a_{0,\mathrm{u}}|^2\right) \tag{93}
\end{aligned}
$$

Nevertheless, the general property of the antisymmetric component of the noise spectrum still holds:

$$
\begin{aligned}
S_{\hat{F}\hat{F}^{\dagger}}^{\mathrm{opt}}[\omega] - S_{\hat{F}^{\dagger}\hat{F}}^{\mathrm{opt}}[-\omega] &= (g^{(0)})^2 \kappa \left(|a_{0,\ell}|^2(|\chi_{\mathrm{c}}[\omega+\Delta_\ell]|^2 - |\chi_{\mathrm{c}}[-\omega+\Delta_\ell]|^2)\right. \\
&\quad \left.+|a_{0,\mathrm{u}}|^2(|\chi_{\mathrm{c}}[\omega+\Delta_{\mathrm{u}}]|^2 - |\chi_{\mathrm{c}}[-\omega+\Delta_{\mathrm{u}}]|^2)\right) \\
&\quad +2\mathrm{Re}\left[g^{(0)} g_{\mathrm{pt}}^{(0)}\left(|a_{0,\ell}|^2(\chi_{\mathrm{c}}[\omega_{\mathrm{ac}}+\Delta_\ell] - \chi_{\mathrm{c}}[\omega_{\mathrm{ac}}-\Delta_\ell])\right.\right. \\
&\quad \left.\left.+|a_{0,\mathrm{u}}|^2(\chi_{\mathrm{c}}[\omega_{\mathrm{ac}}+\Delta_{\mathrm{u}}] - \chi_{\mathrm{c}}[\omega_{\mathrm{ac}}-\Delta_{\mathrm{u}}])\right)\right] \\
&= 2\mathrm{Re}\left[g^{(0)}(g^{(0)}+g_{\mathrm{pt}}^{(0)})\left(|a_{0,\ell}|^2(\chi_{\mathrm{c}}[\omega_{\mathrm{ac}}+\Delta_\ell] - \chi_{\mathrm{c}}[\omega_{\mathrm{ac}}-\Delta_\ell])\right.\right. \\
&\quad \left.\left.+|a_{0,\mathrm{u}}|^2(\chi_{\mathrm{c}}[\omega_{\mathrm{ac}}+\Delta_{\mathrm{u}}] - \chi_{\mathrm{c}}[\omega_{\mathrm{ac}}-\Delta_{\mathrm{u}}])\right)\right] \\
&= -2\mathrm{Im}\Sigma[\omega_{\mathrm{ac}}] = \gamma_{\mathrm{ac,opt}} \tag{94}
\end{aligned}
$$

This result relies crucially on the presence of the $\hat{\xi}_{\mathrm{pt}}/\sqrt{\kappa_{\mathrm{pt}}}$ term in the photothermal force noise, and on the fact that this noise is partially correlated with the intracavity field. Ignoring it and simply replacing the $g^{(0)}$ by $g^{(0)} + g_{\mathrm{pt}}^{(0)}$ in the equation of motion for $\hat{c}$ (which is sufficient for a classical treatment) would ultimately result in $[\hat{c},\hat{c}^{\dagger}] \neq 1$.

The relation above allows us to follow the same route as for a purely radiation pressure coupled system. We can still define the effective occupation of the bath associated with the optical force shot noise

$$
n_{\mathrm{OFSN}} = \frac{S_{\hat{F}^{\dagger}\hat{F}}^{\mathrm{opt}}[-\omega_{\mathrm{ac,eff}}]}{\gamma_{\mathrm{ac,opt}}} \tag{95}
$$

and obtain the equilibrium occupation of the acoustic mode in the same way as in the expression (64) before:

$$
n_{\mathrm{ac}} = \frac{n_{\mathrm{OFSN}}\gamma_{\mathrm{ac,opt}} + n_{\mathrm{th}}\gamma_{\mathrm{ac}}}{\gamma_{\mathrm{ac,eff}}} \tag{96}
$$

22

With that, the expressions for the acoustic spectrum look the same as (65) and (66):

$$S_{\hat{c}^\dagger \hat{c}}[\omega] = \frac{n_{\mathrm{ac}}\gamma_{\mathrm{ac,eff}}}{\gamma_{\mathrm{ac,eff}}^2/4 + (\omega + \omega_{\mathrm{ac,eff}})^2} \qquad (97)$$

$$S_{\hat{c}\hat{c}^\dagger}[\omega] = \frac{(n_{\mathrm{ac}} + 1)\gamma_{\mathrm{ac,eff}}}{\gamma_{\mathrm{ac,eff}}^2/4 + (\omega - \omega_{\mathrm{ac,eff}})^2} \qquad (98)$$

The difference is concealed in the definitions of the optomechanical self-energy $\Sigma = \omega_{\mathrm{ac,opt}} - i\gamma_{\mathrm{ac,opt}}/2$ and the equilibrium acoustic occupation n_{ac}.

One caveat about this difference is the additional optical force noise arising from the photothermal force:

$$\begin{aligned}
\delta(n_{\mathrm{OFSN}}\gamma_{\mathrm{ac,opt}}) &= S_{\hat{F}^\dagger \hat{F}}^{\mathrm{opt}}[-\omega_{\mathrm{ac,eff}}] - S_{\hat{F}\hat{F}}^{\mathrm{RPSN}}[-\omega_{\mathrm{ac,eff}}] \\
&= 2\mathrm{Re}\left[g^{(0)} g_{\mathrm{pt}}^{(0)} \left(|a_{0,\ell}|^2 \chi_{\mathrm{c}}[-\omega_{\mathrm{ac,eff}} + \Delta_\ell] + |a_{0,\mathrm{u}}|^2 \chi_{\mathrm{c}}[-\omega_{\mathrm{ac,eff}} + \Delta_{\mathrm{u}}] \right) \right] \\
&\quad + \frac{|g_{\mathrm{pt}}^{(0)}|^2}{\kappa_{\mathrm{pt}}} \left(|a_{0,\ell}|^2 + |a_{0,\mathrm{u}}|^2 \right)
\end{aligned} \qquad (99)$$

While the first term only depends on the measurable system parameters (and in our case it is much smaller than the RPSN owing to the fact that $g^{(0)}$ is purely imaginary), the second term involves the photothermal channel loss rate κ_{pt}, which we can not access experimentally. To estimate the effect of this term, we can assume that κ_{pt} is associated with the absorptive loss discussed in section 5.2.1. This means that its value can be calculated as $\kappa_{\mathrm{pt}} = \alpha(\kappa - \kappa_{\mathrm{ext}})$, where α is defined in equation (111) and is estimated to be $\alpha = 0.2$ (from room temperature measurements of mirrors' absorption, Section 5.2.1) or $\alpha = 0.7 \pm 0.1$ (from fitting the cryogenic data using the thermal model, Section 5.4). Using these numbers and a total intracavity photon number $\bar{n} = |a_{0,\ell}|^2 + |a_{0,\mathrm{u}}|^2 = 2500$ (which is the maximum photon number for the data shown in the main text) yields an extra phonon occupation of between 0.05 (for $\alpha = 0.7$) and 0.2 (for $\alpha = 0.2$) phonons; these values are between 3 and 10 times smaller than the RPSN effects. Because of this, and because this extra noise becomes even smaller for lower photon numbers (the majority of the data was taken at $\bar{n} < 1000$), we ignore it in the data analysis and assume $n_{\mathrm{OFSN}} = n_{\mathrm{RPSN}}$.

Since the equation of motion (equation (20)) for the optical mode doesn't change (except for an additional loss channel), the general expression (54) for the PSD of the outgoing light still holds. Following that, the results for the PSDs of the red and blue sidebands are also the same as before (equations (70) and (71)).

To find $S_{ii}^{(\mathrm{rb})}$ we can still apply equation (72). In order to do so, we once again need to calculate the correlations between the vacuum noise and the acoustic motion, which follow from the generalized optical force noise:

$$\begin{aligned}
\left\langle \hat{\xi}[\omega_{\mathrm{b}} + \delta\omega]\hat{F}_{\mathrm{opt}}^\dagger[-\omega_{\mathrm{ac,eff}} - \delta\omega] \right\rangle &= (g^{(0)} + g_{\mathrm{pt}}^{(0)})^* a_{0,\ell} \left\langle \hat{\xi}[\omega_{\mathrm{b}} + \delta\omega]\hat{d}_\xi^\dagger[-\omega_{\mathrm{b}} - \delta\omega] \right\rangle \\
&\quad - (g_{\mathrm{pt}}^{(0)})^* \frac{a_{0,\ell}}{\sqrt{\kappa_{\mathrm{pt}}}} \left\langle \hat{\xi}[\omega_{\mathrm{b}} + \delta\omega]\hat{\xi}_{\mathrm{pt}}[-\omega_{\mathrm{b}} - \delta\omega] \right\rangle \\
&= (g^{(0)} + g_{\mathrm{pt}}^{(0)})a_{0,\ell}\chi_{\mathrm{c}}[-\omega_{\mathrm{b}}]\sqrt{\kappa} - (g_{\mathrm{pt}}^{(0)})^* \frac{a_{0,\ell}}{\sqrt{\kappa}}
\end{aligned} \qquad (100)$$

$$\left\langle \hat{\xi}_{\mathrm{ext}}[\omega_{\mathrm{b}} + \delta\omega]\hat{F}_{\mathrm{opt}}^\dagger[-\omega_{\mathrm{ac,eff}} - \delta\omega] \right\rangle = (g^{(0)} + g_{\mathrm{pt}}^{(0)})^* a_{0,\ell}\chi_{\mathrm{c}}[-\omega_{\mathrm{b}}]\sqrt{\kappa_{\mathrm{ext}}} \qquad (101)$$

These lead to

$$\begin{aligned}
&\left\langle \left(\hat{\xi}_{\mathrm{ext}}[\omega_{\mathrm{b}} + \delta\omega] - \sqrt{\kappa_{\mathrm{ext}}\kappa}\chi_{\mathrm{c}}[\omega_{\mathrm{b}}]\hat{\xi}[\omega_{\mathrm{b}} + \delta\omega] \right) \hat{F}_{\mathrm{opt}}^\dagger[-\omega_{\mathrm{ac,eff}} - \delta\omega] \right\rangle \\
&= \sqrt{\kappa_{\mathrm{ext}}}(1 - \kappa\chi_{\mathrm{c}}[\omega_{\mathrm{b}}])(g^{(0)} + g_{\mathrm{pt}}^{(0)})^* a_{0,\ell}\chi_{\mathrm{c}}[-\omega_{\mathrm{b}}] - \sqrt{\kappa_{\mathrm{ext}}}[\omega_{\mathrm{b}}](g_{\mathrm{pt}}^{(0)})^* a_{0,\ell} \\
&= -\sqrt{\kappa_{\mathrm{ext}}}g^{(0)}a_{0,\ell}\chi_{\mathrm{c}}[\omega_{\mathrm{b}}],
\end{aligned} \qquad (102)$$

which is not dependent on the photothermal coupling. This means that the rest of the derivation follows the pure radiation pressure case, and we arrive at the same equation (78) as before.

23

4 Supplementary Note 4: Displacement measurement calibration

In this section we describe the procedure for calibrating the acoustic motional sidebands in units of zero point fluctuations.

Consider the expression for the power spectral density of the blue acoustic sideband (71)

$$
\begin{aligned}
S_{ii}^{(\mathrm{bb})}[\delta\omega] &= G^2|a_{\mathrm{LO}}|^2 \left(\kappa_{\mathrm{ext}}|\chi_{\mathrm{c}}[\omega_{\mathrm{b}}]|^2(g^{(0)})^2|a_{0,\ell}|^2 \frac{n_{\mathrm{ac}}\gamma_{\mathrm{ac,eff}}}{\gamma_{\mathrm{ac,eff}}^2/4 + \delta\omega^2} + 1 \right) \\
&= G^2|a_{\mathrm{LO}}|^2 \left(4\frac{\kappa_{\mathrm{ext}}}{\kappa} \frac{4(g^{(0)})^2|a_{0,\ell}|^2}{\kappa\gamma_{\mathrm{ac,eff}}} \frac{1}{1+(2\delta\omega/\gamma_{\mathrm{ac,eff}})^2} n_{\mathrm{ac}} \frac{1}{1+(2\omega_{\mathrm{b}}/\kappa)^2} + 1 \right) \\
&= G^2|a_{\mathrm{LO}}|^2 \left(4\eta_\kappa \frac{\Gamma_{\mathrm{meas},\ell}}{\gamma_{\mathrm{ac,eff}}} \frac{1}{1+(2\omega_{\mathrm{b}}/\kappa)^2} n_{\mathrm{ac}} \frac{1}{1+(2\delta\omega/\gamma_{\mathrm{ac,eff}})^2} + 1 \right)
\end{aligned}
\tag{103}
$$

Here $\Gamma_{\mathrm{meas},\ell} = \frac{4(g^{(0)})^2|a_{0,\ell}|^2}{\kappa}$ is the measurement strength of the lower control beam, and $\eta_\kappa = \frac{\kappa_{\mathrm{ext}}}{\kappa}$ is the contribution to the quantum efficiency due to imperfect external coupling to the cavity. This power spectral density represents a Lorentzian with width $\gamma_{\mathrm{ac,eff}}$ on top of an approximately frequency-independent background (more precisely, the background is a Lorentzian with width $\kappa \gg \gamma_{\mathrm{ac,eff}}$). The height of the Lorentzian with respect to the background is

$$
a_{\mathrm{rel}}^{(\mathrm{bb})} = 4\eta_\kappa \frac{\Gamma_{\mathrm{meas},\ell}}{\gamma_{\mathrm{ac,eff}}} \frac{1}{1+(2\omega_{\mathrm{b}}/\kappa)^2} n_{\mathrm{ac}}
\tag{104}
$$

This expression is derived under the assumption of no additional loss or noise sources between the cavity output and the detector. Now, assume that there is a finite transmission from the cavity output to the photodetector η_ℓ. It will affect the signal part of the PSD, but not the background, which will stay 1 in photon units. This is especially apparent in the normal-ordering description of the photodetection, where the background comes from the optical local oscillator, which is unaffected by the additional loss. Thus, the relative height is multiplied by η_ℓ

$$
a_{\mathrm{rel}}^{(\mathrm{bb})} = 4\eta_\kappa\eta_\ell \frac{\Gamma_{\mathrm{meas},\ell}}{\gamma_{\mathrm{ac,eff}}} \frac{1}{1+(2\omega_{\mathrm{b}}/\kappa)^2} n_{\mathrm{ac}}
\tag{105}
$$

Next, let us consider an additional source of noise on the way from the cavity to the photodetector (in our case this comes from erbium-doped fiber amplifier, which has a noise figure of ~ 4 dB). We denote its strength relative to the vacuum noise as $n_{\mathrm{add}} = \frac{1}{\eta_{\mathrm{n}}} - 1$, were $\eta_{\mathrm{n}} \leq 1$ represents a drop in quantum efficiency due to this additional noise. With that, the noise background becomes $1 + n_{\mathrm{add}} = \frac{1}{\eta_{\mathrm{n}}}$, and the relative height is further reduced to

$$
a_{\mathrm{rel}}^{(\mathrm{bb})} = 4\eta_\kappa\eta_\ell\eta_{\mathrm{n}} \frac{\Gamma_{\mathrm{meas},\ell}}{\gamma_{\mathrm{ac,eff}}} \frac{1}{1+(2\omega_{\mathrm{b}}/\kappa)^2} n_{\mathrm{ac}}
\tag{106}
$$

Finally, there may be additional mechanisms reducing the signal-to-noise ratio which can't be readily attributed to loss or additional noise. We can denote the quantum efficiency reduction of these residual mechanisms as η_{r} and get the final expression

$$
\begin{aligned}
a_{\mathrm{rel}}^{(\mathrm{bb})} &= 4\eta_\kappa\eta_\ell\eta_{\mathrm{n}}\eta_{\mathrm{r}} \frac{\Gamma_{\mathrm{meas},\ell}}{\gamma_{\mathrm{ac,eff}}} \frac{1}{1+(2\omega_{\mathrm{b}}/\kappa)^2} n_{\mathrm{ac}} \\
&= 4\eta_{\mathrm{t}} \frac{\Gamma_{\mathrm{meas},\ell}}{\gamma_{\mathrm{ac,eff}}} \frac{1}{1+(2\omega_{\mathrm{b}}/\kappa)^2} n_{\mathrm{ac}},
\end{aligned}
\tag{107}
$$

where $\eta_{\mathrm{t}} = \eta_\kappa\eta_\ell\eta_{\mathrm{n}}\eta_{\mathrm{r}}$ is the combined quantum efficiency of the measurement process. For a sideband close to the optical resonance $|\omega_{\mathrm{b}}| \ll \kappa$ the expression above simplifies to

$$
a_{\mathrm{rel}}^{(\mathrm{bb})} = 4\eta_{\mathrm{t}} \frac{\Gamma_{\mathrm{meas},\ell}}{\gamma_{\mathrm{ac,eff}}} n_{\mathrm{ac}}
\tag{108}
$$

To calibrate the measurement rate $\Gamma_{\mathrm{meas},\ell}$ we use the OMIT/A data. The expression for the normalized amplitude of the OMIT/A feature is derived in the Supplemental Information of Ref. [22], which in the notation used in this paper can be written as

$$a_{\mathrm{dr}}^{(\mathrm{bb})} = -\frac{g^{(0)}g_{\mathrm{tot}}^{(0)}|a_{0,\ell}|^2\chi_{\mathrm{c}}[\omega_{\mathrm{b}}]}{\gamma_{\mathrm{ac,eff}}/2} = -\frac{4g^{(0)}g_{\mathrm{tot}}^{(0)}|a_{0,\ell}|^2}{\kappa\gamma_{\mathrm{ac,eff}}}\frac{1}{1-2i\omega_{\mathrm{b}}/\kappa}$$

$$= -\frac{g_{\mathrm{tot}}^{(0)}}{g^{(0)}}\frac{\Gamma_{\mathrm{meas},\ell}}{\gamma_{\mathrm{ac,eff}}}\frac{1}{1-2i\omega_{\mathrm{b}}/\kappa} \tag{109}$$

The minus sign denotes that for a blue sideband (i.e., red-detuned control beam) the OMIT/A feature is a dip, so the Lorentzian is subtracted from the background. Similar to the motional sideband PSD, the expression can be further simplified for an on-resonance sideband:

$$a_{\mathrm{dr}}^{(\mathrm{bb})} = -\frac{g_{\mathrm{tot}}^{(0)}}{g^{(0)}}\frac{\Gamma_{\mathrm{meas},\ell}}{\gamma_{\mathrm{ac,eff}}} \tag{110}$$

If the photothermal coupling $g_{\mathrm{pt}}^{(0)} = g_{\mathrm{tot}}^{(0)} - g^{(0)}$ is known, then the measurement of $a_{\mathrm{dr}}^{(\mathrm{bb})}$ can be used to extract the ratio $\Gamma_{\mathrm{meas},\ell}/\gamma_{\mathrm{ac,eff}}$. Knowing this ratio and η_{t}, one can then use formula (108) to relate the measured relative height of the Brownian motion peak $a_{\mathrm{rel}}^{(\mathrm{bb})}$ to the acoustic mode occupation n_{ac}, and consequently rescale the vertical axis in the motional PSD data in units of phonons. A similar calibration (using the same value of η_{t}, but a different individually determined measurement rate $\Gamma_{\mathrm{meas,u}}$) is performed for the red acoustic sideband. Finally, to normalize the cross-correlator data $S_{ii}^{(\mathrm{rb})}$ we apply a scaling coefficient which is the geometric mean of the coefficients for the red and the blue sidebands.

The relevant contributions to the quantum efficiency in our setup are measured to be:

- Imperfect input cavity coupling $\eta_\kappa = \kappa_{\mathrm{ext}}/\kappa = 0.44 \pm 0.03$.

- Optical loss between the cavity output and the optical amplifier $\eta_\ell = 0.44$.

- Optical amplifier input noise $\eta_{\mathrm{n}} = 0.35 \div 0.40$ (depending on the total power incident on the amplifier).

- Imperfection of the heterodyne detection. The idealized description of the heterodyne detection usually assumes that the power in the optical local oscillator (OLO) is much larger than in the rest of the optical field. If this assumption is relaxed, then the added noise background, which is proportional to the total laser power, becomes larger in comparison with the signal component, which comes only from the mixing with the OLO. As a result, the SNR degrades by an additional factor of $\eta_{\mathrm{r}} = P_{\mathrm{OLO}}/P_{\mathrm{tot}}$, where P_{OLO} is the power in the OLO and P_{tot} is total power incident on the photodiode. In our measurements η_{r} varies between 0.8 and 0.95, depending on the strength of the microwave drives used to create control beams.

Combining these contributions, the total quantum efficiency η_{t} of the setup was between 0.05 and 0.08 depending on the measurement configuration. The relative error in its determination (which gives rise to the uncertainty in Figure 3 of the main text) is 7%, which almost entirely comes from the uncertainty in the relative input cavity coupling η_κ.

5 Supplementary Note 5: Thermal model

5.1 Introduction

The temperature dependence of the speed of sound and acoustic damping in liquid helium are well-studied. As a result, it is straightforward to calculate the temperature dependence of the acoustic mode's frequency ω_{ac}, damping γ_{ac}, and mean phonon number n_{ac} provided that the temperature is uniform throughout the cavity. However in the present device the temperature is not uniform. Here we calculate the expected temperature profile within the cavity using well-known

thermal properties of liquid helium (Section 5.2). We then use this result to calculate $\omega_{\rm ac}$, $\gamma_{\rm ac}$, and $n_{\rm ac}$ (Section 5.3). The results of these two sections are then used to fit the data (Section 5.4)

5.2 Temperature distribution in the cavity

In a superfluid-filled optical cavity, the helium's temperature is set by the balance between heating (caused by optical absorption in the cavity mirrors) and the transport of this heat through the helium to the mixing chamber (MC). In prior work, [22] this transport was limited by the thermal impedance of a narrow "sheath" of helium that connected the cavity to the MC. The sheath's large impedance ensured that the temperature drop between the cavity and the MC occurred primarily in the sheath, leaving the cavity itself at an approximately uniform temperature. As described in the main text, the present device uses a more open geometry without a sheath. This results in an improved thermal link to the MC and allows the cavity to reach lower temperatures; however, the absence of a bottleneck also means that the temperature within the cavity is less uniform than in the device described in Ref. [22].

We model the temperature distribution in the present device by assuming that the heating originates in sub-μm absorbers (located in the DBR coatings) that overlap with the cavity's optical mode, and that the resulting heat propagates outward through the helium. We find that in the overwhelming majority of the cavity the temperature and heat flux density are low enough that thermal transport is via ballistic phonons. However within ≈ 1 μm of each absorber the heat flux density is high enough to produce turbulence, with the result that thermal transport in this small region is described by the Gorter-Mellink model. Despite the smallness of the turbulent region, we find that it plays an important role in the device's performance.

5.2.1 Optical absorption

A schematic illustration of the device is shown in Supplementary Figure 7. The cavity is formed between the end faces of two optical fibers, each having a radius $r_{\rm out} = 100$ μm. The separation between the fibers (and hence the cavity length) is $d = 69.1$ μm. Laser light may be absorbed where the cavity's optical mode overlaps with the mirrors. This corresponds to a disk-shaped region on the fiber surfaces with radius $r_{\rm opt} \approx 7$ μm. The total heat flux from this absorption is:

$$\dot{Q} = \hbar\omega_{\rm l} n_{\rm circ} \kappa_{\rm int} \alpha \tag{111}$$

Here $\hbar$ is the reduced Planck's constant, $\omega_{\rm l}/2\pi = 196.0$ THz is the frequency of the optical mode, $n_{\rm circ}$ is the circulating photon number, $\kappa_{\rm int}/2\pi = 10$ MHz is the internal cavity loss rate, and α is the fraction of the internal loss that leads to heating of the mirrors (as distinguished from internal loss due to photons that are elastically scattered out of the cavity mode and absorbed in some distant part of the apparatus).

Some *a priori* information about α is provided by room-temperature calorimetry measurements, which give the mirror's absorption coefficient $a = 3$ ppm (15 ± 5 ppm) for $\lambda = 1{,}064$ nm (532 nm)[46]. To estimate α from this information, we note that the probability for an intracavity photon to be absorbed by a mirror is given by $P_{\rm mir} = a\frac{\mathcal{F}}{2\pi}\frac{\kappa}{\kappa_{\rm int}}$, where the cavity finesse is $\mathcal{F} \simeq 95{,}000$ and the cavity linewidth $\kappa/2\pi = 21$ MHz. Assuming $a = 3$ ppm for $\lambda = 1{,}529.7$ nm (the wavelength used in the present experiment) gives $P_{\rm mir} = 0.1$. Since the cavity is defined by two mirrors, these assumptions would give $\alpha = 2P_{\rm mir} = 0.2$. This estimate for α is necessarily rough, since the absorption coefficient was measured at room temperature and for a somewhat different wavelength. In Section 5.4, α will be used as a fit parameter.

We assume that photons are absorbed in small (sub-μm) absorbers distributed throughout the DBR layers (as illustrated by the small red circles in Supplementary Figure 7). Each absorber will produce an average heat flux

$$\dot{Q}_1 = \dot{Q}/N \tag{112}$$

where N is the number of absorbers within the optical mode. The heat from each absorber is assumed to spread isotropically into the helium, since the optical fibers' thermal conductivity is extremely low at the relevant temperatures.
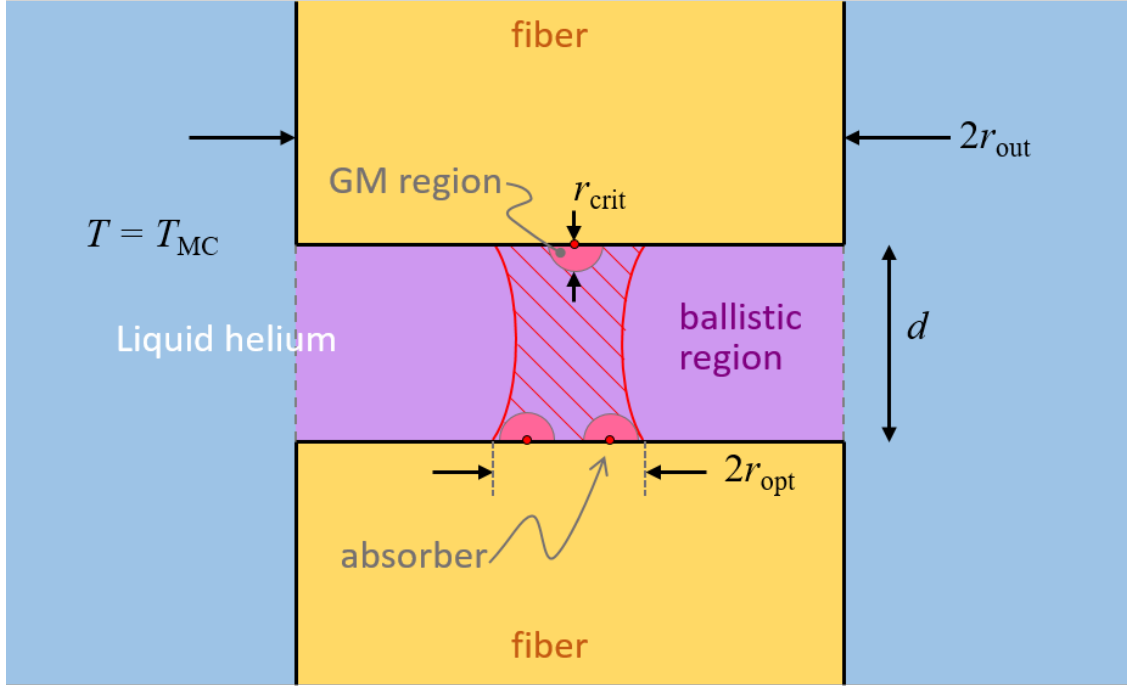
Supplementary Figure 7: Schematic illustration of the thermal model. The calculation assumes that heat is deposited in the device when photons from the cavity's optical mode (red hatched region) are absorbed in microscopic (sub-μm) regions on the cavity mirrors (small red discs). The resulting heat transport through the liquid He involves two distinct regimes: the Gorter-Mellink (GM) regime near the absorbers (pink semicircles), and the ballistic regime (purple region). The liquid He in the blue region is assumed to be in thermal equilibrium with the mixing chamber.

5.2.2 Relevant regimes of thermal transport in liquid helium

The character of thermal transport in helium II depends strongly on the size of the helium channel, its temperature, and the heat flux density [47, 48]. As described below, we find that thermal transport is in the ballistic regime throughout nearly all of the cavity. The only exception is a small region around each absorber, where thermal transport is in the Gorter-Mellink regime.

To calculate the temperature profile, we assume that helium in the region outside of the cavity (the blue region in Supplementary Figure 7) is at the temperature of the mixing chamber T_{MC}. For all T_{MC} used in this work the phonon mean free path λ_{mfp} [49] is much larger than any of the device's dimensions. Thus, at the boundary of the blue region in Supplementary Figure 7 and for some distance inwards (i.e., towards the absorbers) thermal transport is in the ballistic regime.

However the ballistic regime does not extend all the way to the absorbers. This is because the heat flux density $\dot{q} = \dot{Q}_1/2\pi r^2$ increases as the distance r from the absorber decreases. At some distance r_{crit} from the absorber, $\dot{q}$ exceeds the critical value $\dot{q}_{\mathrm{crit}}$ for generating turbulence. Within the turbulent region (i.e., for $r < r_{\mathrm{crit}}$), thermal transport is in the Gorter-Mellink (GM) regime.

We calculate the temperature profile $T(r)$ throughout the cavity by concatenating these two regimes. Specifically, we start with the boundary condition $T(r_{\mathrm{out}}) = T_{\mathrm{MC}}$, and integrate the expressions describing ballistic transport towards decreasing r, stopping when $\dot{q} = \dot{q}_{\mathrm{crit}}$ (or equivalently, when $r = r_{\mathrm{crit}}$). We then use the calculated $T(r_{\mathrm{crit}})$ as a new boundary condition for integrating the GM expressions for $r < r_{\mathrm{crit}}$. The following three subsections (5.2.3 - 5.2.5) provide a detailed description of these steps.

5.2.3 The critical heat flux density

In the GM regime heat is carried by the turbulent normal fluid. The onset of turbulence in helium II is typically estimated in two different ways: (1) by considering the fluid velocity required to produce vortices in the superfluid, or (2) by considering the Reynolds number of the normal fluid. Below, we estimate $\dot{q}_{\mathrm{crit}}$ using both (1) and (2) (the corresponding estimates are labeled $\dot{q}_{\mathrm{crit},1}$ and $\dot{q}_{\mathrm{crit},2}$).

We assume throughout that the net mass flow is zero:

$$\rho_s \mathbf{v}_s + \rho_n \mathbf{v}_n = 0 \tag{113}$$

where $\rho_{s,n}$ and $\mathbf{v}_{s,n}$ are the density and velocity of the superfluid and normal fluid. We also note that regardless of the mechanism by which turbulence sets in, the heat flux density $\dot{q}$ is given by

$$\dot{q} = s\rho T v_n \tag{114}$$

where s is the entropy and $\rho = 145$ kg/m^3 is the mass density of liquid He. The entropy can be evaluated using

$$s(T) = \int_0^T \frac{C(T')}{T'}dT' \tag{115}$$

and the following empirical expressions for the specific heat $C(T)$ [50]:

$$\begin{aligned}
C(T) &= \zeta_1 T^3 & \text{for} & \quad T < 0.6 \text{ K} \\
C(T) &= \zeta_2 T^{6.7} & \text{for} & \quad 0.6 < T < 1.1 \text{ K} \\
C(T) &= \zeta_3 T^{5.6} & \text{for} & \quad 1.1 < T < 2.17 \text{ K}
\end{aligned} \tag{116}$$

where $\zeta_1 = 20.4$ J/(kg $\cdot$ K^4) , $\zeta_2 = 108$ J/(kg $\cdot$ K$^{7.7}$) , and $\zeta_3 = 117$ J/(kg $\cdot$ K$^{6.6}$) .

1. If the onset of turbulence is attributed to the production of vortices, we use the result that vortex lines are produced for superfluid velocity exceeding [50]

$$v_{s,\mathrm{crit}} \simeq \frac{\beta}{d^{1/4}} \tag{117}$$

   where d is the channel diameter and the constant $\beta = 0.03$ m$^{5/4}$/s. We assume $d = 69.1$ μm (i.e., the spacing between the fibers). Equation 117 can be combined with Eq.113 to give

$$v_{n,\mathrm{crit}} \simeq \frac{\rho_s \beta}{\rho_n d^{1/4}} \tag{118}$$

   This may be rewritten (using Eq. 114) as a critical heat flux density:

$$\dot{q}_{\mathrm{crit},1} = s\rho T \frac{\rho_s \beta}{\rho_n d^{1/4}} \tag{119}$$

   In practice, we evaluate Eq. 119 using the following expressions for ρ_s & ρ_n (along with Eq. 115):

$$\rho_n(T) = \frac{s(T)}{s(T_\lambda)}\rho \tag{120}$$

$$\rho_s(T) = \rho - \rho_n(T) \tag{121}$$

2. If the onset of turbulence is attributed to the dynamics of the viscous normal fluid, this will occur when its Reynolds number

$$\mathrm{Re} = \frac{\rho v_n d}{\mu} \approx 1200 \tag{122}$$

where μ is the viscosity of the normal fluid. Combining Eq. 114 & 122 gives

$$\dot{q}_{\text{crit},2} = \frac{1200 s T \mu}{d} \tag{123}$$

In practice, we evaluate Eq. 123 using the empirical expression for the viscosity (valid for $T < 1.8$ K)[50]

$$\mu \approx \nu_5 T^{-5} + \nu_0 \tag{124}$$

where $\nu_5 = 1.4 \times 10^{-6}$ Pa $\cdot$ s/K^5 and $\nu_0 = 1.4 \times 10^{-6}$ Pa $\cdot$ s.

From equation 112, we find:

$$r_{\text{crit},(1,2)} = \sqrt{\frac{\dot{Q}_1}{2\pi \dot{q}_{\text{crit},(1,2)}}} = \eta_{(1,2)} \sqrt{n_{\text{eff}}} \tag{125}$$

Here we have defined $n_{\text{eff}} = n_{\text{circ}} \alpha / N$ (the number of photons absorbed by an individual absorber per cavity lifetime) and $\eta_{(1,2)}$ is the value of $r_{\text{crit},(1,2)}$ for $n_{\text{eff}} = 1$.

Supplementary Figure 8 shows $\eta_{(1,2)}(T)$. From this figure it is apparent that both models (1) and (2) predict a modest temperature dependence for η, and that the two models differ by less than a factor of 4 for the relevant temperature range. Given these qualitative features and the absence of a strong physical justification for choosing one model over the other, we will assume in the following analysis that η is a constant. As described in Section 5.4, η will serve as a fit parameter. For the rough estimates presented in section 5.2.6 (i.e., prior to the fitting), we will simply assume $\eta = 1.0 \times 10^{-8}$ m for concreteness.
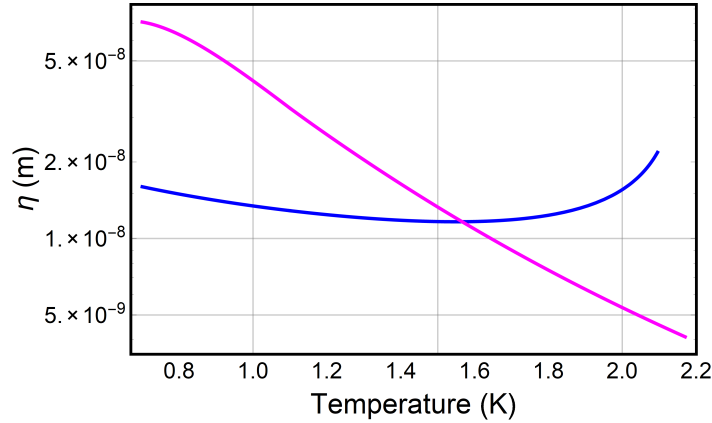
Supplementary Figure 8: The value of η as a function of temperature. Blue line: η_1 (set by superfluid turbulence). Magenta line: η_2 (set by normal fluid turbulence).

For the approach described in this section to be valid, one necessary condition is that the spacing between the absorbers must be larger than r_{crit}:

$$N < \frac{r_{\text{opt}}^2}{r_{\text{crit}}^2} \tag{126}$$

In the present device, this is equivalent to the condition

$$n_{\text{circ}} \alpha < 3 \times 10^5 \tag{127}$$

which is satisfied for all the measurements described here.

5.2.4 Heat propagation in the ballistic regime

As described above, heat propagation is in the ballistic regime for $r > r_{\text{crit}}$. In this regime, the thermal conductivity of liquid helium in a channel is described by the following equation [48]:

$$k = \frac{1}{3}Cvd\frac{2-f}{f} \tag{128}$$

Here C is the specific heat per unit volume, v is the sound velocity, d is the channel diameter (which we take to be 70 μm as above), and f is the probability for a phonon to be diffusively (as opposed to specularly) reflected from the fiber faces.

To estimate f, we note that the probability of diffusive scattering from a rough interface is given by [51]:

$$R_{\text{d}} = 1 - R_0 e^{-\frac{4\pi\sigma^2}{\lambda^2}} \tag{129}$$

The constant R_0 is the interface's reflectivity in the absence of roughness. We estimate $R_0 = 0.99$ based upon the acoustic impedances of helium and the DBR materials [22]. The rms surface roughness σ of similarly prepared fibers was measured to be 0.24 nm [32]. For a thermal distribution of phonons at $T = T_{\text{MC}}$, the most likely wavelength λ_{th} in these experiments ranges from 20 nm (for $T_{\text{MC}} = 500$ mK) to 500 nm (for $T_{\text{MC}} = 20$ mK). As a result, $\lambda_{\text{th}} \gg \sigma$ for all of the measurements described here, so $R_{\text{d}} \approx 1 - R_0 \approx 0.01$. Therefore we set $f = 0.01$.

We can then rewrite expression 128 as:

$$k(T) = \xi T^3 \tag{130}$$

where the constant $\xi = 3200 \text{ W} \cdot \text{m}^{-1} \cdot \text{K}^{-4}$. The expression relating heat flow to temperature gradient is [52]:

$$\frac{1}{2}\frac{\dot{Q}}{A} = -k(T)\frac{dT}{dr} \tag{131}$$

Here $A = 2\pi r^2$ is the area over which the heat is distributed. The factor of 1/2 accounts for the presence of two mirrors. Eq. 131 can be rewritten as

$$\frac{\dot{Q}}{4\pi r^2}dr = -\xi T^3 dT \tag{132}$$

Assuming that $T(r_{\text{out}}) = T_{\text{MC}}$, the temperature at r can be found by integrating Eq. 132 :

$$\frac{\dot{Q}}{4\pi}\int_{r_{\text{out}}}^{r}\frac{1}{r^2}dr = -\xi\int_{T_{\text{mc}}}^{T}T'^3 dT' \tag{133}$$

$$\frac{\dot{Q}}{4\pi}\left(\frac{1}{r_{\text{out}}} - \frac{1}{r}\right) = -\frac{\xi}{4}(T^4 - T_{\text{mc}}^4) \tag{134}$$

$$T(r) = \left(T_{\text{mc}}^4 + \frac{\dot{Q}}{\pi\xi}\left(\frac{1}{r} - \frac{1}{r_{\text{out}}}\right)\right)^{1/4} \tag{135}$$

Supplementary Figure 9 shows the temperature profile between r_{crit} and r_{out} for three different circulating photon numbers and for $T_{\text{MC}} = 50$ mK. The red curve shows the most extreme case used in this work ($T_{\text{MC}} = 50$ mK and $n_{\text{circ}} = 100,000$). Higher T_{MC} or lower n_{circ} leads to more uniform temperature throughout the cavity, as evidenced by Supplementary Figure 10. The color scale in Supplementary Figure 10 shows the ratio $T(r_{\text{crit}})/T_{\text{MC}}$ for different values of T_{MC} and the circulating photon number. The white dots in the figure show the conditions under which the data in in the main paper were taken.
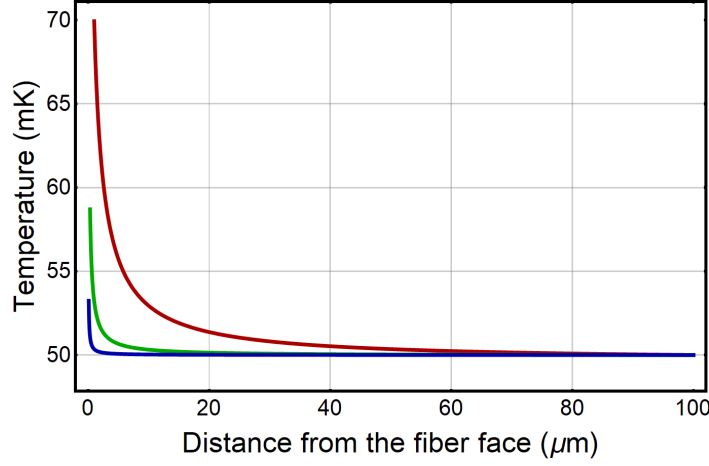
Supplementary Figure 9: The temperature profile in the ballistic region (i.e., for $r_{\text{crit}} < r < r_{\text{out}}$). Blue: $n_{\text{circ}} = 1,000$. Green: $n_{\text{circ}} = 10,000$. Red: $n_{\text{circ}} = 100,000$. In all three cases $T_{\text{MC}} = 50$ mK, $\alpha = 0.2$ and each fiber mirror absorbs the same amount of light.
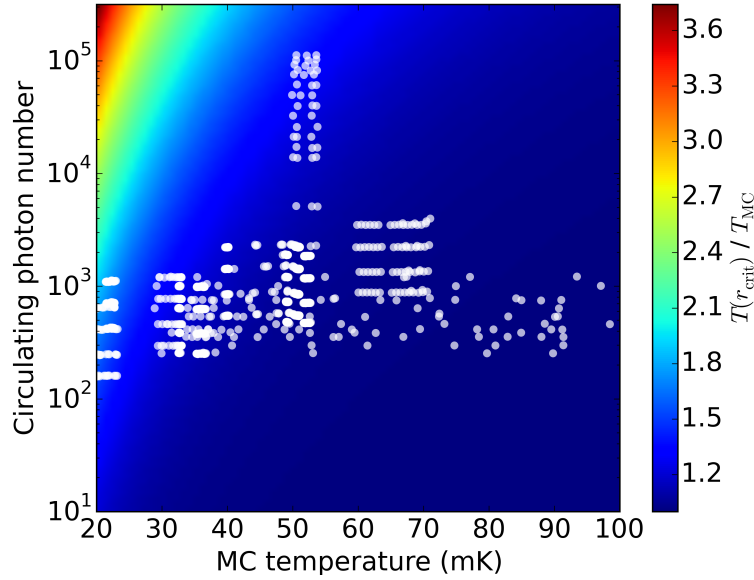
Supplementary Figure 10: Color scale: the ratio $T_{r_{\text{crit}}}/T_{\text{MC}}$ for different values of mixing chamber temperature and circulating photon number, assuming $\alpha = 0.2$. White points: the conditions under which the data shown in the main text were taken.

5.2.5 Heat propagation in the Gorter-Mellink regime

For heat flux above the critical value (i.e., for $r < r_{\text{crit}}$), the thermal conductance is described by the Gorter-Mellink model. This regime is characterized by the following equation [53]:

$$\left(\frac{\dot{Q}_1}{A}\right)^3 = -g(T)\frac{dT}{dr} \tag{136}$$

Note that the heat flux from a single absorber $\dot{Q}_1$ is used. The function $g(T)$ is given by:

$$g(T) = \frac{s^4\rho_s^3 T^3}{A_{\text{GM}}\rho_n} \tag{137}$$

31

Experiments have given a range of values for A_{GM} [53]; however there is general agreement that $A_{\text{GM}} \propto T^3$. Using the approximate average of the data in [53] we take $A_{\text{GM}} = \alpha_{\text{GM}} T^3$ with $\alpha_{\text{GM}} \approx 200$ m·s/(kg·K^3).

To find the temperature profile inside the critical radius, we integrate the temperature from the critical radius inward:
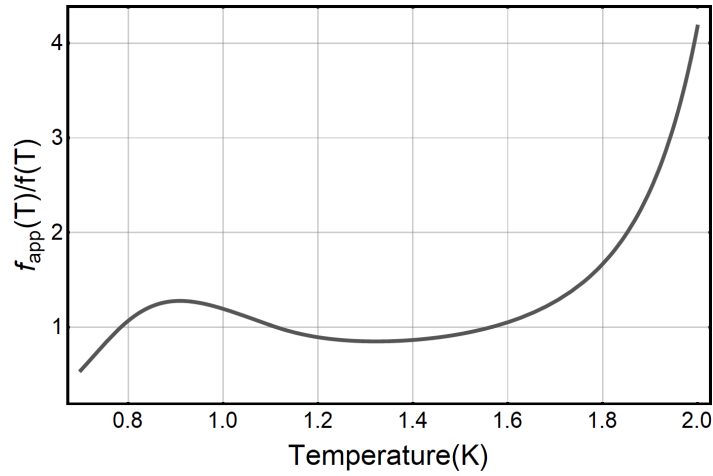
$$\left(\frac{\dot{Q}_1}{2\pi}\right)^3 \int_{r_{\text{crit}}}^{r} \frac{1}{r'^6} dr' = -\int_{T_{\text{crit}}}^{T} g(T') dT' \tag{138}$$

$$\left(\frac{\dot{Q}_1}{2\pi}\right)^3 \frac{1}{5} \left(\frac{1}{r^5} - \frac{1}{r_{\text{crit}}^5}\right) = f(T) - f(T_{\text{crit}}) \tag{139}$$

The function $f(T)$ is defined as the indefinite integral of $g(T)$. It can be written analytically, but the expression is cumbersome so instead we make use of the fact that it can be approximated (to within a factor of 4) by:

$$f_{\text{app}}(T) = \beta T^{18} \tag{140}$$

Where $\beta = 0.5 \times 10^8$ W^3/(m^5· K^{18}) for 0.7 K $< T < 2$ K (Supplementary Figure 11).

Supplementary Figure 11: The ratio $f_{\text{app}}(T)/f(T)$

Combining the preceding two equations gives:

$$T^{18} = T_{\text{crit}}^{18} + \left(\frac{\dot{Q}_1}{2\pi}\right)^3 \frac{1}{5\beta} \left(\frac{1}{r^5} - \frac{1}{r_{\text{crit}}^5}\right) \tag{141}$$

Equation 141 can be further simplified by noting that T_{crit} is close to T_{MC} (as shown above), which is always smaller than 300 mK. For $T_{\text{crit}} = 300$ mK and photon number $n = 100$ photons (the lowest measurable), the second term on the right-hand-side of equation 141 dominates in the the region $0 < r < 0.99r_{\text{crit}}$), so to a good approximation the temperature inside the critical radius depends only on n_{circ} and not on T_{MC}:

$$T(r) = \left(\left(\frac{\dot{Q}_1}{2\pi}\right)^3 \frac{1}{5\beta} \left(\frac{1}{r^5} - \frac{1}{r_{\text{crit}}^5}\right)\right)^{1/18} \tag{142}$$

5.2.6 Temperature profile summary

To summarize, the temperature profile within the cavity is calculated via the following steps:

- Outside of the cylinder defined by the fibers, the temperature is at the mixing chamber temperature $T(r \geq r_{\text{out}}) = T_{\text{MC}}$.

- The total heat radiating into the helium is $\dot{Q} = \hbar \omega_l n_{\text{circ}} \kappa_{\text{int}} \alpha$.

- The heat radiates isotropically into the helium from point-like absorbers. The amount of heat radiated from each absorber is $\dot{Q}_1 = \dot{Q}/N$.

- The heat flux density drops off with distance from the absorber as $\dot{q} = \frac{\dot{Q}_1}{2\pi r^2}$. For $r < r_{\text{crit}}$ thermal transport is in the Gorter-Mellink regime. For $r > r_{\text{crit}}$ the propagation is in the ballistic regime.

- For $r > r_{\text{crit}}$ the temperature is very close to the mixing chamber temperature.

- For $r < r_{\text{crit}}$ the temperature is roughly independent of mixing chamber temperature

Using equations 135 and 142, the temperature profile $T(r)$ can be calculated. Supplementary Figure 12 shows $T(r)$ for $n_{\text{circ}} = 10^5$, $T_{\text{MC}} = 50$ mK, $\alpha = 0.2$, $f = 0.01$, and $N = 2$.
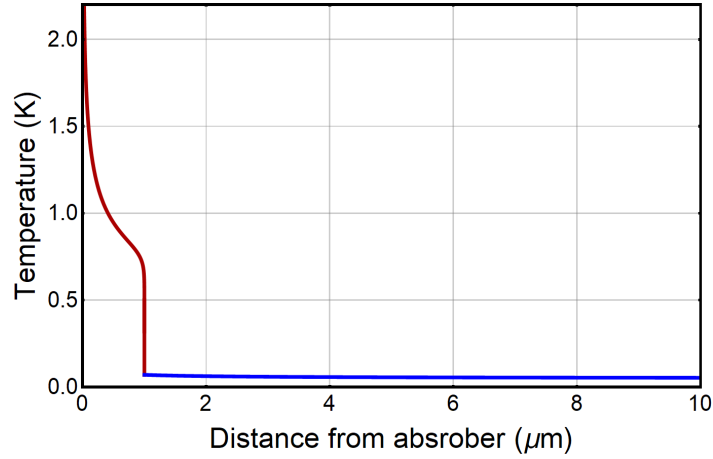
Supplementary Figure 12: The temperature profile inside the critical radius (red), and outside the critical radius (blue) for $n_{\text{circ}} = 10^5$, $T_{\text{MC}} = 50$ mK, $\alpha = 0.2$, $f = 0.01$, and $N = 2$.

5.3 Properties of the acoustic mode

The speed of sound c, density ρ, and acoustic damping rate γ in liquid helium are all functions of temperature. As a result, the spatial variation of the temperature (calculated in section 5.2) leads to spatial variation of c, ρ, and γ. In this section we calculate how this influences the frequency ω_{ac}, linewidth γ_{ac}, and phonon number n_{ac} of the paraxial acoustic mode that is the focus of the main text. In this section we start with the wave equation describing the propagation of sound in an inhomogeneous fluid (subsection 5.3.1), find approximate solutions relevant to the experiments described in the main text (subsection 5.3.2), and finally use these solutions to provide expressions for ω_{ac}, γ_{ac}, and n_{ac} in terms of the experimentally controlled parameters n_{circ} and T_{MC} (subsections 5.3.3 - 5.3.5).

5.3.1 Wave equation for a non-uniform medium

As described in ref. [54], linearizing the hydrodynamic equations gives the following expression for a small-amplitude pressure fluctuation $p(\mathbf{x}, t)$ propagating through a fluid with spatially varying (but static) density $\rho(\mathbf{x})$ and local speed of

sound $c(\mathbf{x})$:

$$\rho(\mathbf{x})\nabla \cdot \left(\frac{1}{\rho(\mathbf{x})} \nabla p(\mathbf{x}, t) \right) - \frac{1}{c(\mathbf{x})^2} \frac{\partial^2 p(\mathbf{x}, t)}{\partial t^2} + \frac{2\delta_{\mathrm{cl}}(\mathbf{x})}{c(\mathbf{x})^4} \frac{\partial^3 p(\mathbf{x}, t)}{\partial t^3} = 0 \tag{143}$$

where $\delta_{\mathrm{cl}}(\mathbf{x})$ is proportional to the fluid's viscosity $\mu(\mathbf{x})$ [54]. Assuming a solution of the form $p(\mathbf{x}, t) = \pi(\mathbf{x})e^{-i\tilde{\omega}t}$ gives the following equation for the eigenmode $\pi(\mathbf{x})$ and the (complex) eigenvalue $\tilde{\omega}$:

$$\rho(\mathbf{x})\nabla \cdot \left(\frac{1}{\rho(\mathbf{x})} \nabla \pi(\mathbf{x}) \right) + \frac{1}{c(\mathbf{x})^2} \tilde{\omega}^2 \pi(\mathbf{x}) + i\frac{\gamma(\mathbf{x})}{c(\mathbf{x})^2} \tilde{\omega}\pi(\mathbf{x}) = 0 \tag{144}$$

where $\mu(\mathbf{x})$ has been rewritten in terms of the local acoustic damping rate $\gamma(\mathbf{x})$.

In the following subsections, we assume that the eigenmode is normalized:

$$\int \pi^2(\mathbf{x})d^3\mathbf{x} = 1 \tag{145}$$

We also make use of the fact that for our system the mode is confined by the optical fibers. This imposes the boundary condition $\frac{\partial \pi(\mathbf{x})}{\partial z} = 0$ at the fiber surface, where z is the direction along the cavity axis (and normal to the fiber surfaces).

5.3.2 Perturbative solutions of the wave equation

Exact solutions to equation 144 are not available unless $c(\mathbf{x})$, $\rho(\mathbf{x})$, and $\gamma(\mathbf{x})$ have very simple forms. To find approximate solutions for arbitrary $c(\mathbf{x})$, $\rho(\mathbf{x})$, and $\gamma(\mathbf{x})$, we write:

$$c(\mathbf{x}) = c_0 + c_1(\mathbf{x}) \tag{146}$$

$$\rho(\mathbf{x}) = \rho_0 + \rho_1(\mathbf{x}) \tag{147}$$

$$\gamma(\mathbf{x}) = \gamma_1(\mathbf{x}) \tag{148}$$

$$\pi(\mathbf{x}) = \pi_0(\mathbf{x}) + \pi_1(\mathbf{x}) \tag{149}$$

$$\tilde{\omega} = \omega_0 + \tilde{\omega}_1 \tag{150}$$

The spatial variations $c_1(\mathbf{x})$, $\rho_1(\mathbf{x})$, and $\gamma_1(\mathbf{x})$ are assumed to be small perturbations. Specifically, we assume $c_1(\mathbf{x}) \ll c_0$, $\rho_1(\mathbf{x}) \ll \rho_0$, and $\gamma_1(\mathbf{x}) \ll \omega_0$, and we assume that these perturbations lead to a small change to the eigenmode ($\pi_1(\mathbf{x})$) and eigenvalue ($\tilde{\omega}_1$). The unperturbed eigenmode $\pi_0(\mathbf{x})$ and the unperturbed eigenvalue ω_0 are assumed to solve the wave equation for the uniform lossless fluid (i.e., equation 144 with $c_1(\mathbf{x}) = \rho_1(\mathbf{x}) = \gamma_1(\mathbf{x}) = 0$).

By combining equation 144 with equations 146 - 150, and keeping only terms that are first-order in the perturbations, it is straightforward to find the shifts in the mode's frequency of oscillation and damping rate that are due to $c_1(\mathbf{x})$, $\rho_1(\mathbf{x})$, and $\gamma_1(\mathbf{x})$. These expressions are discussed in the following two subsections.

5.3.3 Mode frequency

The perturbation theory described in subsection 5.3.2 gives the first-order change in ω_{ac} as:

$$\delta\omega_{\mathrm{ac}} = \mathrm{Re}[\tilde{\omega}_1] = \frac{\omega_0}{c_0} \int c_1(\mathbf{x})\pi_0^2(\mathbf{x})d^3\mathbf{x} + \frac{c_0^2}{2\rho_0\omega_0} \int \pi_0(\mathbf{x})(\nabla \rho_1(\mathbf{x})) \cdot (\nabla \pi_0(\mathbf{x}))d^3\mathbf{x} \tag{151}$$

The spatial variation in the speed of sound and density arise from the spatial variation of the temperature: i.e., $c(\mathbf{x}) = c(T(\mathbf{x}))$ and $\rho(\mathbf{x}) = \rho(T(\mathbf{x}))$. As a result, we can use two of the main results from section 5.2 (which are summarized in subsection 5.2.6) to write equation 151 in a more intuitive form.

First, we assume that in the ballistic region (i.e., whenever the distance from an absorber is greater than r_{crit}) the temperature is simply equal to T_{MC} (and hence independent of $\mathbf{x}$ and n_{circ}). Second, we assume that inside any GM region the temperature is given by equation 142 (and so depends upon $\mathbf{x}$ and n_{circ} but not T_{MC}). The justification for these assumptions is given in section 5.2.

With these assumptions, the mode's frequency of oscillation is conveniently written as

$$\omega_{\text{ac}}(n_{\text{circ}}, T_{\text{MC}}) = \omega_{\text{ac},0} + \delta\omega_{\text{ac}} = \omega_{\text{ac},0} + \delta\omega_{\text{ac,ball}}(T_{\text{MC}}) + \delta\omega_{\text{ac,GM}}(n_{\text{circ}}) \tag{152}$$

In the final expression the first term ($\omega_{\text{ac},0}$) is the mode frequency for a uniform lossless fluid with the constants c and ρ set to their $T = 0$ values. It is used as a fit parameter.

The second term ($\delta\omega_{\text{ac,ball}}$) is given by equation 151 but with the integration carried out only over the ballistic region. In this region $c(\mathbf{x}) = c(T_{\text{MC}})$ and $\rho(\mathbf{x}) = \rho(T_{\text{MC}})$ are both constants. Combined with the fact that the ballistic region's volume is much greater than the GM regions' means that $\delta\omega_{\text{ac,ball}}/\omega_{\text{ac},0} = c(T_{\text{MC}})/c(T = 0)$. For the range of T_{MC} used here ($T_{\text{MC}} < 300$ mK) theory predicts $c(T) - c(T = 0) \propto T^4$, or equivalently:

$$\delta\omega_{\text{ac,ball}} = b_\omega T_{\text{MC}}^4 \tag{153}$$

The constant b_ω is used as a fit parameter.

The third term ($\delta\omega_{\text{ac,GM}}$) is given by equation 151 but with the integration carried out only over the GM regions:

$$\delta\omega_{\text{ac,GM}} = N\frac{\omega_0}{c_0}\int_{V_{\text{GM}}} c_1(T(r(\mathbf{x})))\pi_0^2(\mathbf{x})d^3\mathbf{x} \tag{154}$$

$$+ N\frac{c_0^2}{2\rho_0\omega_0}\int_{V_{\text{GM}}} \pi_0(\mathbf{x})(\nabla\rho_1(T(r(\mathbf{x})))) \cdot (\nabla\pi_0(\mathbf{x}))d^3\mathbf{x} \tag{155}$$

where r is the distance from the absorber, and the factor of N accounts for the total number of absorbers. In practice, we evaluate equation 154 by: (1) combining equation 142 (which gives $T(r)$) with interpolations of the data for $c(T)$ and $\rho(T)$ given in [55] and [56]; (2) using the approximate one-dimensional form for the unperturbed eigenmode $\pi_0(\mathbf{x}) = \sqrt{\frac{2}{d}}\cos(z\omega_0/c_0)$; and (3) performing the integration numerically over a hemisphere of radius r_{crit}.

This approach introduces the following fit parameters: $\omega_{\text{ac},0}$ (the mode's "bare" frequency) and b_ω (which appears in $\delta\omega_{\text{ac,ball}}$). The parameters N, α, and η (introduced in section 5.2) appear in $\delta\omega_{\text{ac,GM}}$.

5.3.4 Mode linewidth

The perturbation theory described in subsection 5.3.2 gives the first-order change in γ_{ac} as:

$$\delta\gamma_{\text{ac}} = \text{Im}[\tilde{\omega}_1] = \int \gamma_1(\mathbf{x})\pi_0^2(\mathbf{x})d^3\mathbf{x} \tag{156}$$

As in the previous subsection, we write the mode's damping rate as the sum of three contributions:

$$\gamma_{\text{ac}}(n_{\text{circ}}, T_{\text{MC}}) = \gamma_{\text{ac},0} + \delta\gamma_{\text{ac}} = \gamma_{\text{ac},0} + \delta\gamma_{\text{ac,ball}}(T_{\text{MC}}) + \delta\gamma_{\text{ac,GM}}(n_{\text{circ}}) \tag{157}$$

The first term, $\gamma_{\text{ac},0}$, is the mode's $T = 0$ damping rate, which is due to acoustic radiation from the liquid helium into the optical fibers (as discussed in Ref. [22]).

The second term, $\delta\gamma_{\text{ac,ball}}$, is given by equation 156 but with the integration carried out only over the ballistic region. For liquid helium at a uniform temperature the acoustic damping rate is $\propto T^4$, so we have

$$\delta\gamma_{\text{ac,ball}} = b_\gamma T_{\text{MC}}^4 \tag{158}$$

The constant b_γ is used as a fit parameter.

The third term, $\delta\gamma_{\mathrm{ac,GM}}$, is given by equation 156 but with the integration carried out only over the GM region. The procedure for evaluating this term is the same as for evaluating $\delta\omega_{\mathrm{ac,GM}}$: the temperature profile $T(r)$ is given by equation 142, while $\gamma(T)$ is given by the theoretical expressions in Ref. [55] for $T < 1.7$ K (where theory and experiment show close agreement) and by interpolating the measurements in Ref. [57] for $T > 1.7$ K.

This approach introduces two fit parameters: $\gamma_{\mathrm{ac,0}}$ (the mode's "bare" damping) and b_γ (which appears in $\delta\gamma_{\mathrm{ac,ball}}$). The parameters N, α, and η (which were introduced in section 5.2) appear in $\delta\gamma_{\mathrm{ac,GM}}$.

5.3.5 The mode phonon number

In the main paper the acoustic mode's mean phonon number n_{ac} is determined from the optical heterodyne signal as $n_{\mathrm{ac}} = (h_{\mathrm{rr}} + h_{\mathrm{bb}} - 1)/2$. In order to facilitate comparison with the thermal model described in this section, we removed the optical damping ("laser cooling") and RPSN contributions from n_{ac} by plotting $n_{\mathrm{th}} = n_{\mathrm{ac}}(\gamma_{\mathrm{ac,eff}}/\gamma_{\mathrm{ac}}) - n_{\mathrm{O}}\gamma_{\mathrm{ac}}/\gamma_{\mathrm{ac}}$ on the vertical axes of Fig. 3, A and B. The quantity n_{th} represents the mean number of phonons in the acoustic mode's mechanical bath, as inferred from the optical heterodyne signal.

In this subsection, we extract an estimate of $n_{\mathrm{th}}(T_{\mathrm{MC}}, n_{\mathrm{circ}})$ from the thermal model described above. In Fig. 3, B and C of the main paper, this estimate is converted to an effective temperature of the acoustic mode $T_{\mathrm{eff}} = \frac{\hbar\omega_{\mathrm{ac}}}{k_{\mathrm{B}} \ln(1+n_{\mathrm{th}}^{-1})}$ and used as the horizontal axis.

To begin, we note that if the temperature throughout the helium in the cavity were uniform, the acoustic mode's mean phonon number would be

$$n_{\mathrm{th}} = \frac{n_{\mathrm{fib}}\gamma_{\mathrm{ac,0}} + n_0\gamma_0}{\gamma_{\mathrm{ac,0}} + \gamma_0} \tag{159}$$

where $n_0 = 1/(e^{\hbar\omega_{\mathrm{ac}}/(k_{\mathrm{B}}T_0)} - 1)$, $n_{\mathrm{fib}} = 1/(e^{\hbar\omega_{\mathrm{ac}}/(k_{\mathrm{B}}T_{\mathrm{fib}})} - 1)$, T_0 is the uniform temperature of the helium in this hypothetical case, T_{fib} is the temperature of the optical fiber, and $\gamma_0 = \gamma(T_0)$. Since the helium's temperature and damping rate are both non-uniform, we rewrite equation 159 as

$$n_{\mathrm{th}} = \frac{n_{\mathrm{fib}}\gamma_{\mathrm{ac,0}} + \int n_{\mathbf{x}}(T(\mathbf{x}))\gamma(T(\mathbf{x}))\pi_0^2(\mathbf{x})d^3\mathbf{x}}{\gamma_{\mathrm{ac,0}} + \int \gamma(T(\mathbf{x}))\pi_0^2(\mathbf{x})d^3\mathbf{x}} \tag{160}$$

where

$$n_{\mathbf{x}}(T(\mathbf{x})) = 1/(e^{\hbar\omega_{\mathrm{ac}}/(k_{\mathrm{B}}T(\mathbf{x}))} - 1) \tag{161}$$

As in subsections 5.3.3 and 5.3.4, we separate the integrals in equation 160 into one integral over the ballistic region and another over the GM region. This gives

$$n_{\mathrm{th}} = \frac{n_{\mathrm{fib}}(T_{\mathrm{MC}}, n_{\mathrm{circ}})\gamma_{\mathrm{ac,0}} + n_{\mathrm{ball}}(T_{\mathrm{MC}})\delta\gamma_{\mathrm{ac,ball}}(T_{\mathrm{MC}}) + f_{\mathrm{GM}}(n_{\mathrm{circ}})}{\gamma_{\mathrm{ac,0}} + \delta\gamma_{\mathrm{ac,ball}}(T_{\mathrm{MC}}) + \delta\gamma_{\mathrm{ac,GM}}(n_{\mathrm{circ}})} \tag{162}$$

where the dependences upon T_{MC} and n_{circ} are noted explicitly, and $n_{\mathrm{ball}} = 1/(e^{\hbar\omega_{\mathrm{ac}}/(k_{\mathrm{B}}T_{\mathrm{MC}})} - 1)$. The function

$$f_{\mathrm{GM}} = N \int_{V_{\mathrm{GM}}} n_{\mathbf{x}}(T(r(\mathbf{x})))\gamma(T(r(\mathbf{x})))\pi_0^2(\mathbf{x})d^3\mathbf{x} \tag{163}$$

We estimate T_{fib} by assuming that the fiber's thermal conductivity $\propto T^k$, which gives

$$T_{\mathrm{fib}} = (T_{\mathrm{mc}}^{k+1} + \sigma^{k+1}n_{\mathrm{circ}})^{1/(k+1)} \tag{164}$$

The constant σ parameterizes how much each circulating photon contributes to heating of the fiber. Measurements of the thermal conductivity of amorphous silica at low temperatures [52] give $k = 1.91$. Both σ and k are used as fitting parameters.

5.4 Fitting data

In the work described here, three properties of the acoustic mode were measured (i.e. by fitting heterodyne noise spectra and OMIT/A spectra): ω_{ac}, γ_{ac}, and n_{th}. They were measured as a function of two externally controlled parameters: n_{circ} and T_{MC}. Expressions for $\omega_{ac}(n_{circ}, T_{MC})$, $\gamma_{ac}(n_{circ}, T_{MC})$, and $n_{th}(n_{circ}, T_{MC})$ were derived in Sections 5.2 and 5.3, and in Eq. (1) of the main text. The complete set of measurements of $\omega_{ac}(n_{circ}, T_{MC})$, $\gamma_{ac}(n_{circ}, T_{MC})$, and $n_{th}(n_{circ}, T_{MC})$ was fit to these expressions in two steps.

For the first step, we considered measurements of $\omega_{ac}(n_{circ}, T_{MC})$ and $\gamma_{ac}(n_{circ}, T_{MC})$ for which $n_{circ} < 500$. As shown in Supplementary Figure 13, these measurements are approximately independent of n_{circ}. From this observation we conclude that for $n_{circ} < 500$ no appreciable heating occurs from optical absorption, so we fit this data to the expressions derived above with n_{circ} set to zero:

$$\omega_{ac}(0, T_{MC}) = \omega_{ac,0} + b_\omega T_{MC}^4 \tag{165}$$

$$\gamma_{ac}(0, T_{MC}) = \gamma_{ac,0} + b_\gamma T_{MC}^4 \tag{166}$$

The advantage of this approach is that it employs only four fitting parameters: $\omega_{ac,0}$, $\gamma_{ac,0}$, b_ω, and b_γ. The resulting fits are shown in Supplementary Figure 13. The best-fit values of $\omega_{ac,0}$, $\gamma_{ac,0}$, b_ω, and b_γ are listed in Table 1, along with their *a priori* expected values.
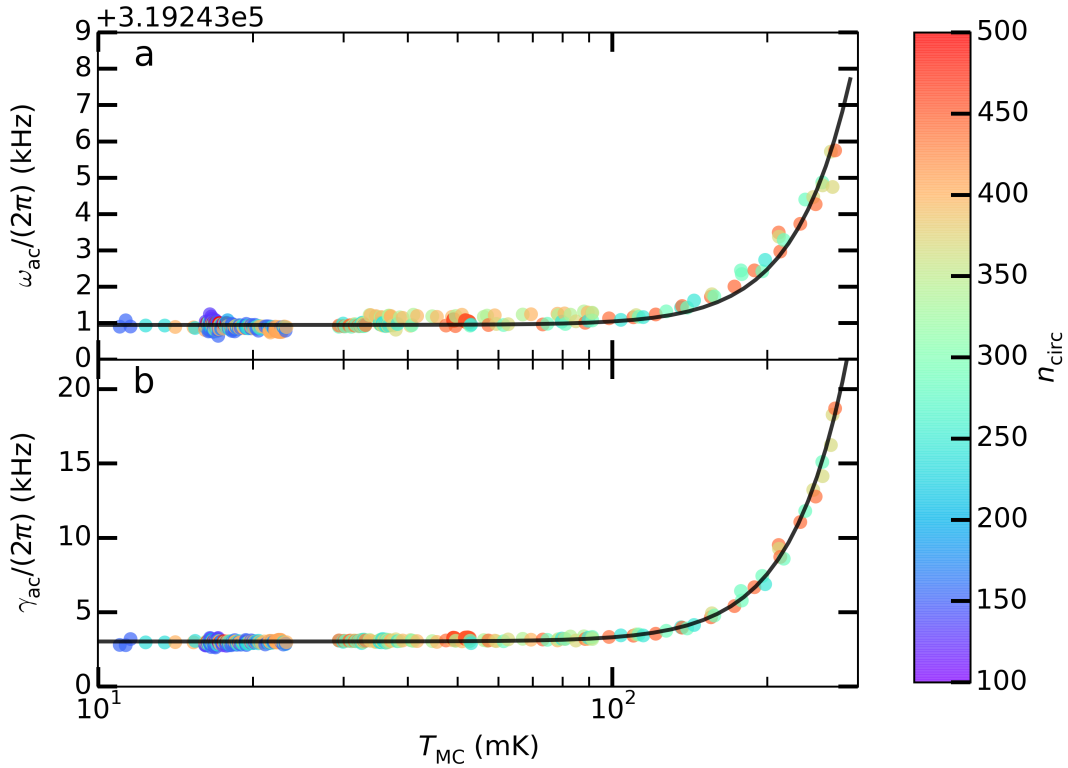
Supplementary Figure 13: Temperature dependence of the acoustic frequency and linewidth. (a) Frequency and (b) linewidth vs. T_{MC} for $n_{circ} < 500$ mK. The dots represent data, with the color corresponding to the circulating photon number n_{circ}. The solid lines show the fit. The best-fit values of the four fit parameters ($\omega_{ac,0}$, $\gamma_{ac}, 0$, b_ω, b_γ) are listed in Table 1

For the second step, the complete set of measurements of $\omega_{ac}(n_{circ}, T_{MC})$, $\gamma_{ac}(n_{circ}, T_{MC})$, and $n_{th}(n_{circ}, T_{MC})$ was fit to the expressions derived in Sections 5.2 and 5.3:

$$\omega_{ac}(n_{circ}, T_{MC}) = \omega_{ac,0} + \delta\omega_{ac,GM}(n_{circ}) + b_\omega T_{MC}^4 \tag{167}$$

37

Parameter [units]	Best fit value	Expected value
$\omega_{\mathrm{ac},0}/2\pi$ [MHz]	$319.24 \pm 5 \times 10^{-6}$	319.24
$\gamma_{\mathrm{ac},0}/2\pi$ [Hz]	3026 ± 6	4000 ± 2400
$b_\omega/2\pi$ [Hz/K^3]	$(0.93 \pm 0.01) \times 10^6$	1×10^6
$b_\gamma/2\pi$ [Hz/K^4]	$(2.79 \pm 0.01) \times 10^6$	2.70×10^6
σ [K]	$(2.2 \pm 0.2) \times 10^{-2}$	-
k	3.0 ± 0.1	1.91
α	0.69 ± 0.02	0.2
$N \in \mathbb{Z}^+$	1	≥ 1
η [m]	$(1.01 \pm 0.01) \times 10^{-8}$	$5 \times 10^{-9} < \eta < 7 \times 10^{-8}$

Table 1: Fit parameters and the expected values.

$$\gamma_{\mathrm{ac}}(n_{\mathrm{circ}}, T_{\mathrm{MC}}) = \gamma_{\mathrm{ac},0} + \delta\gamma_{\mathrm{ac,GM}}(n_{\mathrm{circ}}) + b_\gamma T_{\mathrm{MC}}^4 \tag{168}$$

$$n_{\mathrm{th}}(n_{\mathrm{circ}}, T_{\mathrm{MC}}) = \frac{n_{\mathrm{fib}}\gamma_{\mathrm{ac},0} + n_{\mathrm{ball}}b_\gamma T_{\mathrm{MC}}^4 + f_{\mathrm{GM}}(n_{\mathrm{circ}})}{\gamma_{\mathrm{ac},0} + b_\gamma T_{\mathrm{MC}}^4 + \gamma_{\mathrm{ac,GM}}(n_{\mathrm{circ}})} \tag{169}$$

For these fits, the parameters $\omega_{\mathrm{ac},0}$, $\gamma_{\mathrm{ac},0}$, b_ω, and b_γ are fixed to the best-fit values determined in the first step. This leaves five fitting parameters: N, α, η, k, and σ. The data were fit using these five parameters, with N constrained to be a positive integer and α constrained ≤ 1. The best fit values are listed in Table 1, along with the expected values. Although the best fit was achieved with $N = 1$, qualitatively similar fits were achieved with $N = 2$ and $N = 3$. For $N \geq 4$ the fits do not reproduce the qualitative trends in the data. The resulting fits are shown in Supplementary Figure 14.
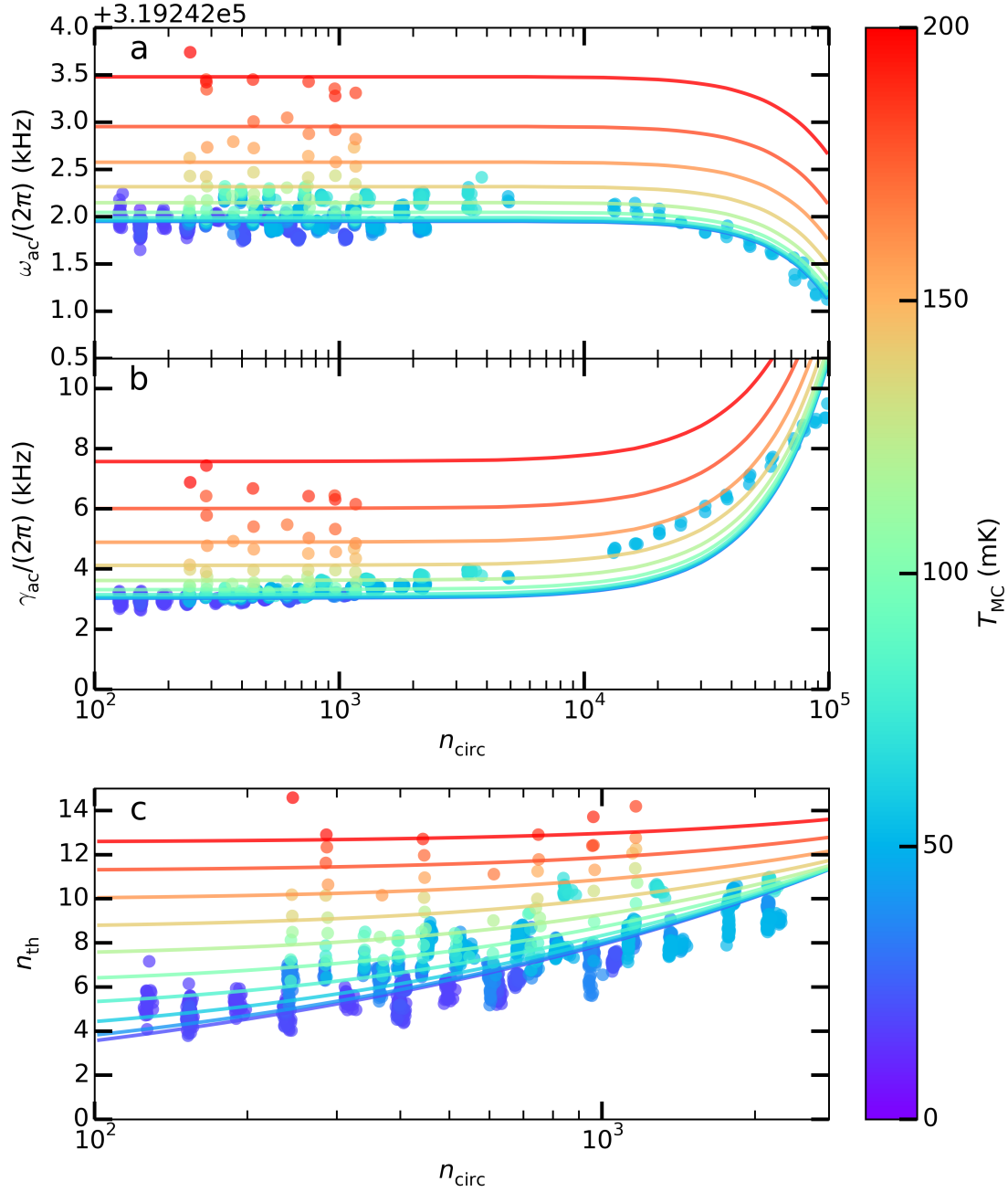
Supplementary Figure 14: Optical spring, optical damping, and mean phonon number. (a) Acoustic mode frequency. (b) Acoustic mode linewidth. (c) Acoustic mode thermal phonon number nth (defined in the main text). All three are plotted as a function of the cavity photon number n_{circ} for $T_{MC} < 200$ mK. The dots represent data, and the solid lines show the fit. For both the data points and the fit lines, the color corresponds to T_{MC}. The best-fit values of the five fit parameters ($N, \alpha, \eta, k, \sigma$) are listed in Table 1.

References

[37] Jayich, A. M., et al. Cryogenic optomechanics with a Si_3N_3 membrane and classical laser noise. *New Journal of Physics*, 14(11):115018, nov 2012.

[38] Børkje, K. Heterodyne photodetection measurements on cavity optomechanical systems: Interpretation of sideband asymmetry and limits to a classical explanation. *Phys. Rev. A*, 94(4):043816, oct 2016.

[39] Kashkanova, A. D., et al. Optomechanics in superfluid helium coupled to a fiber-based cavity. *J. Opt.*, 19(3):034001, 2017.

[40] Hunger, D., Deutsch, C., Barbour, R. J., Warburton, R. J., and Reichel J. Laser micro-fabrication of concave, low-roughness features in silica. *AIP Adv.*, 2:012119, 2012.

[41] Flowers-Jacobs, N. E., et al. Fiber-cavity-based optomechanical device. *Appl. Phys. Lett.*, 101(2):221109, 2012.

[42] Kashkanova, A. D. Optomechanics with superfluid helium. Ph.D. Thesis, Yale University (2017).

[43] H. J. Carmichael. Spectrum of squeezing and photocurrent shot noise: a normally ordered treatment. *Journal of the Optical Society of America B*, 4(10):1588, oct 1987.

[44] A. A. Clerk, S. M. Girvin, F. Marquardt, R. J. Schoelkopf, and M. H. Devoret. Introduction to quantum noise, measurement, and amplification. *Reviews of Modern Physics*, 82(2):1155–1208, apr 2010.

[45] J. Restrepo, J. Gabelli, C. Ciuti, and I. Favero. Classical and quantum theory of photothermal cavity cooling of a mechanical oscillator. *Comptes Rendus Physique*, 12(9-10):860–870, 2011.

[46] Correspondence with LaserOptik mirror coating company, 2014.

[47] M. Sciacca, A. Sellitto, and D. Jou. Transition to ballistic regime for heat transport in helium II. *Phys. Lett. A*, 378(34):2471–2477, 2014.

[48] B. Bertman and T. A. Kitchens. Heat transport in superfluid filled capillaries. *Cryogenics (Guildf).*, 8(1):36–41, 1968.

[49] R. W. Whitworth. Experiments on the Flow of Heat in Liquid Helium below 0.7 degrees K. *Proc. R. Soc. A Math. Phys. Eng. Sci.*, 246(1246):390–405, 1958.

[50] S. W. Van Sciver. *Helium Cryogenics*. Springer New York, New York, NY, 2012.

[51] H. E. Bennett and J. O. Porteus. Relation between surface roughness and spectral reflectance at normal incidence. *J. Opt. Soc. Am.*, 51(2):123–129, 1961.

[52] F. Pobell. *Matter and methods at low temperatures*. Springer-Verlag Berlin Heidelberg, 2007.

[53] V. Arp. Heat Transport Through Helium II. *Cryogenics (Guildf).*, 10:96–105, 1970.

[54] A. D. Pierce. *Acoustics*. McGraw-Hill Book Company, New York, NY, USA, 1982.

[55] B. M. Abraham, Y. Eckstein, J. B. Ketterson, M. Kuchnir, and J. Vignos. Sound propagation in liquid He4. *Phys. Rev.*, 181(1):347–373, 1969.

[56] R. J. Donnelly and C. F. Barenghi. The observed properties of liquid helium at the saturated vapour pressure. *J. Phys. Chem. Ref. Data*, 27(6), 1998.

[57] R. L. St. Peters, T. J. Greytak, and G. B. Benedek. Brillouin scattering measurements of the velocity and attenuation of high frequency sound waves in superfluid helium. *Opt. Commun.*, 1:412–416, 1970.